FINAL REPORT

Distorted Turbulent Flow in a Shear Layer

Contract Number : N00014-10-1-0910

Principal Investigator: Stewart A.L. Glegg

Dept. of Ocean and Mechanical Engineering
Florida Atlantic University
Boca Raton
FL 33431

Email: sglegg@fau.edu

March 2014

Report Documentation Page		*Form Approved* *OMB No. 0704-0188*

Public reporting burden for the collection of information is estimated to average 1 hour per response, including the time for reviewing instructions, searching existing data sources, gathering and maintaining the data needed, and completing and reviewing the collection of information. Send comments regarding this burden estimate or any other aspect of this collection of information, including suggestions for reducing this burden, to Washington Headquarters Services, Directorate for Information Operations and Reports, 1215 Jefferson Davis Highway, Suite 1204, Arlington VA 22202-4302. Respondents should be aware that notwithstanding any other provision of law, no person shall be subject to a penalty for failing to comply with a collection of information if it does not display a currently valid OMB control number.

1. REPORT DATE **MAR 2014**	2. REPORT TYPE **N/A**	3. DATES COVERED **28 June 201 - 31 Jan 201**

4. TITLE AND SUBTITLE	5a. CONTRACT NUMBER
Distorted Turbulent Flow in a Shear Layer	5b. GRANT NUMBER
	5c. PROGRAM ELEMENT NUMBER

6. AUTHOR(S)	5d. PROJECT NUMBER
	5e. TASK NUMBER
	5f. WORK UNIT NUMBER

7. PERFORMING ORGANIZATION NAME(S) AND ADDRESS(ES) **Florida Atlantic University, 777 Glades Road, Boca Raton, FL 33431**	8. PERFORMING ORGANIZATION REPORT NUMBER

9. SPONSORING/MONITORING AGENCY NAME(S) AND ADDRESS(ES) **Office of Naval Research 875 Randolph Street Arlington, VA 22203-1995**	10. SPONSOR/MONITOR'S ACRONYM(S)
	11. SPONSOR/MONITOR'S REPORT NUMBER(S)

12. DISTRIBUTION/AVAILABILITY STATEMENT
Approved for public release, distribution unlimited

13. SUPPLEMENTARY NOTES

14. ABSTRACT

This report describes the work carried out under grant number N00014-10-1-0910 Distorted Turbulent Flow in a Shear Layer at Florida Atlantic University. The project was in collaboration with Dr. William Devenport of Virginia Tech, who has carried out wind tunnel measurements on the rotor system described in this report as part of a companion project. The overall objective of this study is to measure and predict the sound radiation from a rotor operating near a wall in a wind tunnel. Results are given showing the methods used to calculate the far field noise levels and how this is related to the distortion of the inflow turbulence as it enters the rotor.

15. SUBJECT TERMS

16. SECURITY CLASSIFICATION OF:			17. LIMITATION OF ABSTRACT	18. NUMBER OF PAGES	19a. NAME OF RESPONSIBLE PERSON
a. REPORT **unclassified**	b. ABSTRACT **unclassified**	c. THIS PAGE **unclassified**	**SAR**	**120**	

Standard Form 298 (Rev. 8-98)
Prescribed by ANSI Std Z39-18

Summary

This report describes the work carried out under grant number N00014-10-1-0910 "Distorted Turbulent Flow in a Shear Layer" at Florida Atlantic University. The project was in collaboration with Dr. William Devenport of Virginia Tech, who has carried out wind tunnel measurements on the rotor system described in this report as part of a companion project. The overall objective of this study is to measure and predict the sound radiation from a rotor operating near a wall in a wind tunnel. Results are given showing the methods used to calculate the far field noise levels and how this is related to the distortion of the inflow turbulence as it enters the rotor.

This first part of the report describes how broadband rotor noise can be predicted directly from measurements of turbulent velocity correlation functions upstream of a rotor without the need for turbulence modeling. The method is based on a time domain formulation and uses the turbulence velocity correlation function in the plane of the rotor to describe the inflow velocity statistics. The application of this theory to a rotor mounted near a hard wall is described. It is shown that rotor noise measurements for a non thrusting rotor (taken at Virginia Tech in a companion project) are well predicted using this approach. It is also shown that to calculate the blade response correctly the time step of the numerical computation must be less than the time it takes for an acoustic wave to travel from the leading edge to the trailing edge of the blade section.

For a thrusting rotor the inflow turbulence is stretched and distorted as it enters the rotor and this effect can have a significant impact on the noise source levels. Part II of the report focuses on the distortion of turbulent inflows that occur when a rotor is embedded in a turbulent boundary layer. More specifically, it considers how this inflow can be analyzed using Rapid Distortion Theory (RDT) based on Batchelor and Proudman's approach(in which the mean shear remains undistorted). It is concluded that the an upper bound can be obtained for the velocity correlation function after a rapid distortion and that this can be calculated from the mean flow, including shear, providing the mean shear is undistorted by the turbulence.

Part III of the report shows how the time domain approach to rotor noise prediction can be combined with rapid distortion theory to predict the far field noise from a thrusting rotor. The method used for the noise prediction was the same as used in Part I of the report and the measured velocity correlation function was corrected for mean flow distortion using the method outlined in Part II. The implementation of RDT requires the calculation of the mean flow and this has been carried out using three different inflow models, a RANS model with a multiple reference frame model for the rotor, a RANS model with an actuator disc model for the rotor, and a potential flow model with an actuator disc representing the rotor. The RANS model with the actuator disc was found to be most satisfactory and was been found to be consistent with flow visualizations in the wind tunnel experiment. One of the most important conclusions from this study was that the flow in the boundary layer near the rotor showed the effect of separation at the lower advances ratios. This will cause the boundary layer turbulence to be significantly modified and the RDT approach is not suitable for these conditions. There was also an issue in defining where the RDT calculation should be started to properly reflect the effect of the

distortion on the turbulence. It was concluded that it should be one Lagranian lengthscale upstream of the rotor disc plane.

The predicted noise levels for a thrusting rotor were compared to measurements at three different angles to the rotor axis and at two different advance ratios. The agreement between the measurement and predictions was good at high frequencies. However, around the blade passing frequency where haystacking effects were dominant, the measured levels were under predicted, and the RDT correction was shown to reduce rather than increase the predicted levels. It was concluded that for a thrusting rotor the effect of separation in the boundary layer near the disc plane and its effect on the turbulence needed to be modeled more accurately.

Table of Contents

Part 1: Broadband rotor noise predictions using a time domain approach

I. Introduction

Broadband noise from fans and rotors ingesting a turbulent flow has been studied extensively [1-20]. In the majority of these studies the far field sound has been analyzed using a frequency domain approach which is based on the concepts introduced by Ffowcs-Williams and Hawkings[21] for the sound radiation from rotating machinery. The frequency domain approach recognizes that the propagation distance from a rotating source to a fixed observer varies periodically in time and any function of the propagation distance can be expanded as a Fourier series. This leads to a formulation with an infinite series of terms that is slow to converge and so computation times can be large as more detail about the source is added to the calculation. An alternative approach for slowly rotating systems such as helicopter rotors was introduced by Amiet[5] and used by Glegg *et al* [12] for wind turbines. This approach only applies when the blade passing frequency is very much less than the bandwidth of the broadband noise and is not applicable to rotors where the blade passing tones and the broadband noise are in the same frequency range. In contrast Casper and Farassat[22] introduced a time domain approach to calculate broadband trailing edge noise, relating the surface pressure correlation function to the far field sound for a stationary airfoil. In this paper we will extend this concept to inflow turbulence noise from rotating blades. This approach has two advantages over frequency domain methods. The first is that the time domain method does not require the summation of an infinite series of terms that depend on Bessel functions, and so is numerically faster to evaluate than a frequency domain method. The second is that the unsteady loading on the blade surface can be directly related to the velocity correlation function of the incoming turbulence, which can be measured directly. In a frequency domain method the turbulence is characterized by its wavenumber spectrum and this cannot usually be obtained over the entire wavenumber range of interest without some intermediate turbulence modeling. Furthermore for the inhomogeneous inflows that are found in real applications the wavenumber spectrum is not readily modeled. In contrast four dimensional inhomogeneous velocity correlation functions can be measured [19] and used as the input for the time domain method described in this paper.

In sections 2 and 3 we will outline the approach for predicting broadband rotor noise in the time domain. We will then apply the method to predict the sound radiation from a rotor that is partially immersed in a boundary layer as shown in Figure 1. Experimental measurements for this configuration are given by Alexander *et al*.[23] and the four dimensional velocity correlation function of the flow entering the rotor was measured by Morton *et al*[19], so all the data needed for the prediction method is available, and no assumptions regarding the characteristics of the turbulent flow are required. We will only consider a rotor operating at zero thrust so that the mean flow distortion of the inflow turbulence will not be important and the measured turbulence characteristics in the absence of the rotor can be used as an input to the predictions.

2. Broadband Rotor Noise: Time Domain Theory

This section will describe the theory for the broadband noise generation from an open rotor caused by the unsteady loading on the blades. We start with the solution to Lighthill's wave equation given by Ffowcs Williams and Hawkings[24] which gives the acoustic field from a thin blade in arbitrary motion with a net blade surface loading per unit area of $f_i(\mathbf{y},\tau)$ as

$$(1)$$

$$p(\mathbf{x},t) = -\frac{\partial}{\partial x_i}\sum_{n=1}^{B}\int_{\Sigma_n}\left[\frac{f_i(\mathbf{y},\tau)}{4\pi r\,|1-M_r\,|}\right]_{\tau=\tau*}d\Sigma_n(\mathbf{y})$$

In this equation Σ_n represents the planform of each blade and r is the distance from the source point to the observer. The terms in [] are evaluated at the correct retarded time $\tau=\tau*=t-r(\tau)/c_o$, c_o is the speed of sound and M_r is the Mach number of the source velocity in the direction of the observer. The coordinate system for the analysis is shown in Figure 2.

For broadband noise we are interested in calculating the power spectrum of the acoustic field. However since rotor noise is non-stationary we must specifically take the time of observation into account and average measurements over multiple revolutions. We will define the power spectrum as

$$(2)$$

$$S_{pp}(\mathbf{x},\omega) = \frac{1}{2T}\int_{-T}^{T}\frac{1}{2\pi}\int_{-T}^{T}Ex\left[p(\mathbf{x},t)p(\mathbf{x},t')\right]e^{i\omega(t-t')}dtdt'$$

where the averaging time $2T$ is large compared to the time taken for one revolution of the rotor so that $\Omega T>>1$. This will ensure that the blade passage tones are fully resolved and that the analysis allows for multiple blade passages through the same turbulent structures.

The analysis is simplified if we make the compact chord assumption. In this case the surface loading on the blade can be replaced by a force per unit span $F^{(n)}(R,\tau)$ on the nth blade, which acts in the direction of the normal to the blade surface, defined as $n_i^{(n)}(R,\tau)$ and is a function of radius $R=(y_2^2+y_3^2)^{1/2}$. In general the superscript n refers to the blade number. We then obtain from equation (1)

$$(3)$$

$$p(\mathbf{x},t) = \sum_{n=1}^{B}\int_{R_{min}}^{R_{max}}\left[\frac{\partial}{\partial x_i}\frac{n_i^{(n)}(R,\tau)F^{(n)}(R,\tau)}{4\pi r^{(n)}(\tau)\,|1-M_r\,|}\right]_{t=\tau+r^{(n)}(\tau)/c_o}dR$$

where R_{min} and R_{max} are the radius of the blade hub and tip respectively. The integrand in equation (2) is then defined as

$$(4)$$

$$Ex[p(\mathbf{x},t)p(\mathbf{x},t')] = \sum_{n=1}^{B}\sum_{m=1}^{B}\int_{R_{min}}^{R_{max}}\int_{R_{min}}^{R_{max}}$$

$$\left[\left\{\frac{\partial}{\partial x_i}\frac{n_i^{(n)}(R,\tau)}{4\pi r^{(n)}|1-M_r|}\right\}\left\{\frac{\partial}{\partial x_i}\frac{n_j^{(m)}(R,\tau')}{4\pi r^{(m)}|1-M_r|}\right\}R_{FF}^{(n,m)}(R,R',\tau,\tau')\right]_{\substack{t=\tau+r^{(n)}/c_o\\t'=\tau+r^{(m)}/c_o}} dRdR'$$

where

(5)

$$R_{FF}^{(n,m)}(R,R',\tau,\tau') = Ex[F^{(n)}(R,\tau)F^{(m)}(R',\tau')]$$

is the cross correlation coefficient of the force per unit span on the blades.

The integrals over observer time in (2) can be changed to an integral over emission time because the time differentials are related by $dt=|1-M_r|d\tau$. Since $t=\tau+r(\tau)/c_o$ it follows that

(6)

$$S_{pp}(\mathbf{x},\omega) = \frac{1}{4\pi T}\sum_{n=1}^{B}\sum_{m=1}^{B}\int_{R_{min}}^{R_{max}}\int_{R_{min}}^{R_{max}}\int_{-T}^{T}\int_{-T}^{T}$$

$$\left\{\frac{\partial}{\partial x_i}\frac{n_i^{(n)}(R,\tau)e^{i\omega r^{(n)}(\tau)/c_o}}{4\pi r^{(n)}(\tau)}\right\}\left\{\frac{\partial}{\partial x_i}\frac{n_j^{(m)}(R,\tau')e^{-i\omega r^{(m)}(\tau')/c_o}}{4\pi r^{(m)}(\tau')}\right\}R_{FF}^{(n,m)}(R,R',\tau,\tau')e^{i\omega(\tau-\tau')}dRdR'd\tau d\tau'$$

The force is directed at an angle normal to the inflow angle β (see Figure 2) and so the direction of the force can be specified for a right handed rotor as

(7)

$$n_i^{(n)} = (\cos\beta,\sin\beta\sin(\Omega\tau+\phi_n),-\sin\beta\cos(\Omega\tau+\phi_n))$$

where $\phi_n=2\pi n/B$, as shown in Figure 2 for a rotor that has a angular velocity Ω and an axial speed of V in the x_1 direction. For a left handed rotor the angular velocity is $-\Omega$ and the blade angle is $-\beta$.

The location of the leading edge of each blade in the fixed frame of reference for a right handed rotor is given by

(8)

$$\mathbf{y}^{(n)}(R,\tau) = (V\tau,R\cos(\Omega\tau+\phi_n),R\sin(\Omega\tau+\phi_n))$$

The source position is not periodic because the rotor moves relative to the observer. However in near field or wind tunnel applications we are interested in an observer that moves at the same speed as the rotor hub. For the moving observer, that is at an angle θ_o to the axial direction in hub based coordinates,

(9)

$$\mathbf{x} = (r_o \cos\theta_o + Vt, r_o \sin\theta_o \cos\phi_o, r_o \sin\theta_o \sin\phi_o)$$

The propagation distance r is then given by the solution to the equation

(10)

$$r(\tau) = ((r_o \cos\theta_o + Vr(\tau)/c_o)^2 + (r_o \sin\theta_o \cos\phi_o - R\cos(\Omega\tau + \phi_n))^2$$
$$+ (r_o \sin\theta_o \sin\phi_o - R\sin(\Omega\tau + \phi_n))^2)^{1/2}$$

It follows that $r(\tau)$ is a periodic function of the source time τ and repeats every blade revolution.

In a frequency domain method the integrals over time in equation (6) would be evaluated analytically by expanding the terms in {} as a Fourier series and defining the loading correlation function in terms of it's cross spectrum. The resulting equations include the summation of a slowly converging infinite series of terms that is time consuming to compute. In the time domain method the integrals over time in equation (6) are evaluated numerically and since the integrand consists of relatively simple functions the numerical integrations have been found to reduce the computation time by a factor of approximately 20. This numerical advantage is one of the most important reasons for using this approach.

3. The unsteady blade loadings

3.1 The blade response function

If we make a strip theory approximation the unsteady loading per unit area can be approximated by two dimensional unsteady loading at each radius. For an incompressible flow this gives

(11)

$$F^{(n)}(\omega_o, R) = \left\{\pi\rho c U(R)S(\sigma)\right\} w^{(n)}(R, \omega_o) \qquad S(\sigma) = \frac{2e^{i\sigma}}{\pi\sigma(H_o^{(1)}(\sigma) + iH_1^{(1)}(\sigma))}$$

where c is the blade chord, ρ is the fluid density, U is the blade speed, $S(\sigma)$ is Sears function (referenced to a gust at the leading edge of the blade) which depends on the non dimensional frequency $\sigma = \omega_o c/2U(R)$ and $w^{(n)}(R, \omega)$ is the Fourier transform with respect to time of the upwash encountered by the leading edge of the blade. The functions $H_o^{(1)}$ and $H_1^{(1)}$ are Hankel functions of the first kind.

The fluctuating force in the time domain is given by the convolution integral

(12)

$$F^{(n)}(R, \tau) = \int_{-\infty}^{\tau} s(R, \tau - \tau_o) w^{(n)}(R, \tau_o) d\tau_o$$

where

(13)

$$s(R, \tau) = \frac{1}{2\pi} \int_{-\infty}^{\infty} \left\{\pi\rho c U(R)S(\sigma)\right\} e^{-i\omega\tau} d\omega$$

8

and the branch cut associated with the Sears function is chosen so $S(-\sigma)=S^*(\sigma).$ Using the approximation to the Sears function given by $S(\sigma)\sim(i/(1+2\pi\sigma))^{1/2}$ and the non-dimensional time $\tilde{\tau} = 2U\tau / c$ we obtain the asymptotic solutions to this integral as

(14)

$$s(R,\tau) = 2\rho U^2(R)\operatorname{Re}\left\{\int_0^\infty \left(\frac{i}{1+2\pi\sigma}\right)^{1/2} e^{-i\sigma\tilde{\tau}}d\sigma\right\} \approx \begin{cases} \dfrac{\sqrt{2}\rho U^2(R)}{\sqrt{\tilde{\tau}}} & \tilde{\tau}<<1 \\[4mm] \dfrac{\sqrt{2}\rho U^2(R)}{\tilde{\tau}} & \tilde{\tau}>>1 \end{cases}$$

Based on these two approximate solutions we can define an asymptotic form for the Sears function in the time domain as

(15)

$$s(R,\tau) \approx \frac{\sqrt{2}\rho U^2(R)}{\sqrt{\tilde{\tau}+\tilde{\tau}^2}}$$

Alternatively we can use the time domain response function given by Amiet[25] for a compressible gust. For a delta function gust defined as $(w_o c/2)\delta(\gamma-tU)= (w_o c/2U)\delta(\gamma/U-t),$ where γ is the distance along the chord parallel to the flow (see Figure 2), Amiet[25] gives

(16)

$$F(\tau) = \rho(c/2)w_o U A(\tilde{\tau}) \qquad \tau_a = 2M/(1+M)$$

$$A(\tilde{\tau}) = \begin{cases} 2/M^{1/2} & \tilde{\tau}<\tau_a \\[3mm] \dfrac{4\sin^{-1}(\sqrt{\tau_a/\tilde{\tau}})}{\pi M^{1/2}} & \tilde{\tau}>\tau_a \end{cases}$$

where $M=U/c_o$ is the section Mach number. For a more general gust we can define the convolution integral

(17)

$$w(\tau-\gamma/U) = \int_{-\infty}^\infty w(\tau-\tau_1)\delta(\tau_1-\gamma/U)d\tau_1$$

We can use Amiet's solution in (17) to give

(18)

$$F(\tau) = \rho U^2 \int_{-\infty}^\infty w(\tau-\tau_1)A(2U\tau_1/c)d\tau_1$$

and it follows that $s(R,\tau)=\rho U^2 A(2U\tau/c)$.

We can also define the blade response function in the time domain using the Kussner function for the response of a flat plate to a step gust. The time derivative of the Kussner function then gives the response to a Dirac gust which can be used to define $s(R,\tau)$. From Leishman[26] we obtain an approximation to the Kussner function that gives

(19)

$$s(R,\tau) = \rho U^2 \frac{\partial}{\partial \tilde{\tau}} \left(\frac{2\pi(\tilde{\tau}^2 + \tilde{\tau})}{\tilde{\tau}^2 + 2.82\tilde{\tau} + 0.8} \right)$$

Each of these functions are shown in Figure 3 and we note that the incompressible Sears response function differs significantly from the compressible solution given by Amiet[25]. Amiet's solution will be more accurate when the time lag is less than the propagation time for the acoustic wave to travel from the leading edge to the trailing edge, but will be less accurate for large time scales because, in the form given above, it does not allow for all the acoustic waves reflected at the blade leading and trailing edges. In contrast the incompressible solution includes acoustic waves with infinite propagation speed and so is most accurate when the time lag is large enough to include multiple reflections of the acoustic waves at the leading and trailing edges. Integrating $s(R,\tau)$ over $0 < \tilde{\tau} < \tau_a$ for Sears' and Amiet's solutions gives an identical result, and so it can be argued that for gusts with non dimensional time scales $\tau_s >> \tau_a$ the incompressible solution is more accurate. For a subsonic rotor $\tau_a < 1$ and in most applications the lengthscales are not as large as the blade chord so $\tau_s < 2$. This implies that Amiet's response is a more accurate model than the incompressible solution.

3.2 The blade loading correlation function

We can define the loading correlation function using equation (12) as

(20)

$$R_{FF}^{(n,m)}(R,R',\tau,\tau') = \int\limits_{-\infty}^{\tau} \int\limits_{-\infty}^{\tau} s(R,\tau - \tau_o)s(R',\tau' - \tau_o)R_{ww}^{(n,m)}(R,R',\tau_o,\tau_o')d\tau_o d\tau_o'$$

where R_{ww} is the correlation function of the upwash velocity. Providing that R_{ww} is known these integrals can be evaluated numerically in the time domain.

In the rotor noise problem the blade moves through a frozen turbulence field defined by $\mathbf{v}(\mathbf{y},\tau)$ and encounters an upwash gust

(21)

$$w^{(n)}(R_o,\tau_o) = n_i^{(n)}(R_o,\tau_o)v_i(\mathbf{y}^{(n)}(\tau_o,R_o),\tau_o)$$

where $n_i^{(n)}$ is the blade surface normal to the nth blade as defined in equation (7). We then obtain the upwash correlation function required by equation (20) as

$$R_{ww}^{(n,m)}(R,R',\tau_o,\tau_o') = n_i^{(n)}(R,\tau_o)n_j^{(m)}(R',\tau_o')R_{ij}(\mathbf{y}^{(n)}(\tau_o,R),\mathbf{y}^{(m)}(\tau_o',R'),\tau_o-\tau_o') \tag{22}$$

where $R_{ij}(\mathbf{x},\mathbf{y},\tau)$ is the cross correlation function of the turbulent velocity in the plane of the rotor.

This can be simplified since we can define

$$n_i^{(n)}(R,\tau) = n_i^{(0)}(R,\tau+\phi_n/\Omega) \qquad y_i^{(n)}(R,\tau) = y_i^{(0)}(R,\tau+\phi_n/\Omega) \tag{23}$$

so that

$$R_{ww}^{(n,m)}(R,R',\tau_o,\tau_o') = n_i^{(0)}(R,\tau_m)n_j^{(0)}(R',\tau_m'-s\Delta\tau)R_{ij}(\mathbf{y}^{(0)}(\tau_m,R),\mathbf{y}^{(0)}(\tau_m'-s\Delta\tau,R'),\tau_m-\tau_m') \tag{24}$$

$$\tau_m = \tau_o + m\Delta\tau \qquad \Delta\tau = 2\pi/B\Omega \qquad s = m-n$$

Using these results the correlation function is defined as only a function of *s=m-n*, and this significantly reduces the computation time.

Combining the results of this section with the acoustic theory given in section 3 gives a complete procedure for calculating broadband rotor noise from measurements of the velocity correlation function of the inflow turbulence. It includes blade to blade correlation effects as well as the spanwise integration of the unsteady loading. Furthermore by adding the mean flow perturbation to the correlation function, the tone noise for the rotor can be included in the calculation. The method assumes that the correlation function in the rotor disc plane is known and the effect of mean flow distortion on the turbulence as it enters the rotor must be calculated separately.

4. Numerical Evaluations and Comparisons with Experimental Measurements

4.1 The Experimental Arrangement

In order to evaluate the approach described above we will predict the noise from the rotor used in a recent study by Alexander *et al*[23]. The rotor is a 2.25 scale version of the rotor used in Sevik's [8] study. It has 10-blades with 57.2mm chord and a tip diameter of 457.2mm. The hub diameter was extended slightly beyond the 2.25 scale to a 127mm diameter by removing the inner 6.35mm of each blade root. The blades have square tips and no skew. The geometric angle of attack varies from 55.6° at the root to 21.2° at the tip. The airfoil sections have a maximum thickness of 9.7% at the root and 8.4% at the tip occurring approximately at mid-chord. Sevik[8] indicates that the design advance ratio for this rotor is 1.17. The nose of the rotor was extended to house instrumentation although no on-board devices were used in this study. A straight, constant-diameter 247.1mm long instrumentation tube extended in front of the rotor blade sections which was capped by a 135.6mm long aerodynamic nose cone. Since we are concerned with the acoustic prediction of rotor noise we will only consider the zero thrust case that does not cause mean flow distortion. This corresponds to a free steam tunnel velocity of U_∞ =30m/s, and a rotor speed of 2734 rpm.

Measurements were taken in the Virginia Tech Stability Wind Tunnel which has low turbulence levels (0.01% to 0.03%) and interchangeable aerodynamic and anechoic test sections each 1.83m square and 7.3m long. The anechoic section, detailed in Devenport *et al*.[27], has tensioned Kevlar walls that are acoustically transparent but contain the flow so a jet catcher is not needed. Acoustic data can be taken from anechoic chambers that run alongside the test section on the port and starboard side

A single 9.5mm boundary layer trip was placed 4.76m upstream of the rotor in the wind tunnel contraction section resulting in the growth of a two-dimensional boundary layer on the wall to which the rotor was mounted (Figure 1). The boundary layer was approximately 100mm thick at the location of the rotor plane with a Re_θ up to 16,600. Two four-sensor hotwire probes were used to measure boundary layer profiles and two-point space time correlations at the rotor blade station with the rotor removed. The hotwire probes were traversed from 4mm to 124mm from the wall (encompassing approximately 1.2 times the boundary layer thickness) at some 1781 relative positions providing the complete 4 dimensional velocity correlation function for the rotor inflow at zero thrust. More details regarding the measurements can be found in Alexander *et al*[23] and Morton *et al* [19].

4.2 Numerical Considerations

Hard Wall Correction

The experimental set up of the rotor shown in Figure 1 includes a hard reflecting surface in close proximity to the rotor. To accurately predict the rotor noise the reflections from this surface will be important and will typically cause an increase of level at low frequencies of up to 6 dB, ground reflection interference dips and an increase of high frequency broadband levels of 3dB

[12]. To correct for the reflections from the surface an image rotor can be added to the calculation. This will account for the reflected field exactly, including the correct directionality and retarded time effects. To include an image rotor in the calculation the Greens function defining the propagation of sound from each blade element, defined by the terms in {} in equation (6) is modified to

$$(24)$$

$$\left\{ \frac{\partial}{\partial x_i} \left(\frac{n_i^{(n)} e^{i\omega r(\tau)/c_o}}{4\pi r(\tau)} \right) + \frac{\partial}{\partial x_i^{\#}} \left(\frac{n_i^{(n)} e^{i\omega r^{\#}(\tau)/c_o}}{4\pi r^{\#}(\tau)} \right) \right\}$$

where $r^{\#}=|\mathbf{x}^{\#}|$ and $\mathbf{x}^{\#}=(x_1,-x_2-2h,x_3)$ represents the distance from the image source to the fixed observer. This is a relatively simple correction that has a minimal effect on the computational effort.

Radial and Time Integrations

The predictions are based on the combination of equations (6) and (20) which involve a double radial integration and two double time integrals, which are carried out numerically for each combination of the blade number. This approach will include all possible correlation effects between both radial stations and different blades. The acoustic radiation is dominated by the loading near the blade tips where the blade speed is fastest and so a logarithmic distribution of radial blade segments is used to approximate the radial integral with the more closely spaced segments near the blade tips. The calculations shown below are based on fifteen blade segments but only small differences are found if ten segments are used.

The critical numerical parameters for the integrals over time are the time step $\Delta\tau$ and the integration time T. The latter determines the frequency resolution of the predicted spectra and needs to be large enough to include blade to blade correlations over multiple revolutions. For the rotor experiment described here Morton *et al*[19] showed that the blade to blade correlation would be zero for time delays that exceed two revolutions. Numerical evaluation of the spectra using the same velocity correlation data showed that this was the case and calculations based on integration over two or three rotor revolutions are almost identical (Figure 4).

The time step for the integrals in equation (6) are specified by the standard Nyquist criteria based on the highest frequency of interest. However the time step requirement for the convolution integrals given by equation (20) depend on the characteristics of the blade response functions shown in Figure 3. First we note that for the incompressible models based on the Sears and Kussner functions the blade response varies rapidly for small time delays. To integrate this curve numerically the time step must be chosen to correctly capture this variation, which implies that we need at least ten steps in the range $0<2U\tau/c<1$. Based on this criteria the time step should be $\Delta\tau<0.05c/U$. In contrast the compressible flow blade response function given by Amiet[25] has a uniform amplitude for small time delays and can be integrated accurately with larger time steps. For the compressible case a single time step can be used over the range $0<2U\tau/c<2M/(1+M)$ which leads to the requirement that $\Delta\tau=c/(c_o+U)$ or less. This time step is determined by the time it takes for an acoustic wave to travel from the leading edge to the trailing edge of the blade. It is interesting to note that the time step requirement is les restrictive for the compressible model

13

than for the incompressible model for blade Mach numbers greater than 0.05. It is also important to note that the compressible model includes more of the physics of the blade response than the incompressible approximation. For Sears model the blade response is instantaneous and the whole flow adjusts to the blade gust interaction as soon as the gust reaches the leading edge of the blade. The compressible flow model is more is more satisfactory because it allows for the finite time it takes for the flow in the vicinity of the blade to adjust to the blade gust interaction. On this basis the most accurate results are expected to be obtained using the compressible flow solution with the time step chosen as $\Delta\tau < c/(c_o + U)$. This result applies at all Mach numbers because for very slow blade speeds the blade response in the time domain will still be dominated by the characteristics of the blade response function at very small time delays, which can only be correctly modeled using a compressible solution.

To illustrate the impact the time step has on the predicted spectra Figure 5 shows spectra calculated with different time steps using a compressible flow blade response function and the Sears response function. The blade tip Mach number in this example is $M=0.2$ and the non dimensional time steps based on this flow speed are specified as $\Omega\Delta\tau = 2\pi/128, 2\pi/154$ and $2\pi/192$. To resolve the compressible flow solution requires $\Omega\Delta\tau < \Omega c/(c_o + U) = 2\pi/158$. The results shown in Figure 5 indicate that reducing the time step has only a small effect if this criterion is met, and even when the time step is 20% larger than the optimum level the error is less than 1dB. However for the incompressible flow solution based on the Sears function the under prediction is of the order of 5dB.

4.3 Comparisons with measurements

In Figure 6 the predicted and measure spectra are given for an observer at 29° to the rotor axis. The rotor is operating at zero thrust and the velocity correlation function in the plane of the rotor is specified by the measurements given in Morton *et al*[22] for the same wind tunnel configuration without the rotor present. The calculations were carried by averaging over two rotor revolutions and using a time step of $\Omega\Delta\tau = 2\pi/192$.

The spectra show a broad peak that has a maximum at a frequency that is just above blade passing frequency. The measured and predicted levels agree well over the entire frequency range, apart from at the first peak in the spectra at ~500Hz and at the dip in the measured spectra at ~800 Hz. These may be the result of residual distortion of the turbulence approaching the rotor due to the rotor centerbody. This would tend to slightly stretch the turbulence, emphasizing these haystacked features. Predictions of different thrust cases are not given here because the effect of the mean flow distortion on the inflow turbulence is not included in this model.

To demonstrate the predicted directionality of the far field sound Figures 7 and 8 show the predicted spectra at two different observation angles. We note that the high frequencies, above 1000 Hz, are well predicted in all cases and the level variation, which differs by as much as 10dB between different observer angles, is accurately captured. The characteristics of the measured spectra at low frequencies however is not as well predicted, and we note that the measured peak frequency changes significantly with observer angle. It seems unlikely that this is a feature of mean flow distortion on the turbulence and is more likely caused by acoustic interference effects in the wind tunnel at these frequencies.

5. Conclusions

This paper describes a method for the prediction of broadband rotor noise that is based on a time domain approach. The inputs required are the dimensions and speed of the rotor and the four dimensional velocity correlation function in the plane of the rotor. The surface sources are integrated over each blade and both blade to blade and spanwise correlations are included so that their full effect on the directionality of the radiated sound field is retained. The effect of a near by reflecting surface is included in the calculations and there is no requirement that the observer should be in the acoustic far field. In general it was found that the time domain calculations were an order of magnitude faster than the equivalent computations based on a frequency domain method.

The crucial parameter that affects the accuracy of the computation is the size of the time step used for the numerical calculation of the blade response function. It was found that a compressible blade response function should be used and that consistent results were obtained if the time step was less than the time for an acoustic wave to travel from the leading edge to the trailing edge of the blade.

References
1. I.J. Sharland, Sources of noise in axial flow fans, *Journal of Sound and Vibration* **1**, (1964) 302-322.
2. B.D. Mugridge and C.L. Morfey, Sources of noise in axial fans, *Journal of the Acoustical Scoiety of America* **51**, (1972) 1411-1426
3. G.F. Homicz and A.R. George, Broadband and discrete frequency radiation from subsonic rotors *Journal of Sound and Vibration* **36**, (1974) 151-177
4. A.R. George and Y.N. Kim, High frequency broadband rotor noise, *AIAA Jnl*. **15,** (1977), 538-545
5. R.K. Amiet, Noise produced by a turbulent flow into a rotor or helicopter rotor, *AIAA Jnl*. **15,** (1977), 307-308
6. K.S. Aravamudan and W.L. Harris, Low frequency broadband noise generated by a model rotor, *Journal of the Acoustical Scoiety of America* **66**, (1979) 522-533
7. R.W. Paterson and R.K. Amiet, Noise from a model rotor due to ingetion of turbulence *NASA CR-3213 (*1979)
8. Sevik, M, Sound Radiation from a Subsonic Rotor Subjected to Turbulence, NASA SP 304, (1971)
9. Blake, W., *Mechanics of Flow Induced Sound and Vibration*, Wiley, New York, 1986.
10. Hanson, D B, Spectrum of Rotor Noise Caused by Atmospheric Turbulence, *Journal of the Acoustical Society of America*, **56**(1), (1974) 110-126.
11. Fink, M.R., Minimum on-axis noise from a rotor or helicopter rotor, *Journal of Aircraft* **15**, (1978) 700-702
12. Glegg, S.,Baxter, S.M., and Glendinning, A.G. ,The prediction of broadband noise from wind turbines, *Journal of Sound and Vibration* **118**(2), (1987) 217-239
13. Majumder S and Peake N, 1998, Noise Generation by the Interaction between Ingested Turbulence and a Rotating Fan, *Journal of Fluid Mechanics*, vol. 359, pp. 181-216.

14. Stephens D and Morris C, 2009, Sound Generation by a Rotor Interacting with a Casing Turbulent Boundary Layer, *AIAA Journal*, vol. 47, pp. 2698-2708.
15. Wojno J, Mueller T and Blake W, 2002, Turbulence Ingestion Noise, Part 1: Experimental Characterization of Grid-Generated Turbulence, *AIAA Journal*, vol. 40, pp. 16-25.
16. Wojno J, Mueller T and Blake W, 2002, Turbulence Ingestion Noise, Part 2: Rotor Aeroacoustic Response to Grid Generated Turbulence, *AIAA Journal*, vol. 40, pp. 26-32.
17. Morton, M A, 2012, Rotor Inflow Noise Caused by a Boundary Layer: Inflow Measurements and Noise Predictions, Master's Thesis, AOE Department, Virginia Tech, Avail: http://scholar.lib.vt.edu/theses/available/etd-08102012-103032/.
18. Catlett M R, Anderson, J M, and Stewart D O, Aeroacoustic Response of Rotors to Sheared Turbulent Inflows, 18th AIAA/CEAS Aeroacoustics Conference, Colorado Springs, CO, June 4-6, 2012, AIAA-2012-2137.
19. Morton M, Devenport W, Alexander W N, Glegg S A L, and Borgoltz A, "Rotor Inflow Noise Caused by a Boundary Layer: Inflow Measurements and Noise Predictions", 18th AIAA/CEAS Aeroacoustics Conference, Colorado Springs, CO, June 4-6, 2012, AIAA-2012-2120.
20. Glegg, S A L, Morton, M, Devenport, W, "Rotor Inflow Noise Caused by a Boundary Layer: Theory and Examples", 18th AIAA/CEAS Aeroacoustics Conference, Colorado Springs, CO, June 4-6, 2012, AIAA-2012-2263.
21. Ffowcs-Willaims, J.E., and Hawkings D.L., Theory related the noise from rotating machinery *Journal of Sound and Vibration* **10,** (1969) 10-21
22. Casper, J. and Farassat, F., Broadband trailing edge noise predictions in the time domain, *Journal of Sound and Vibration* **271,** (2002) 159-176.
23. Alexander, W. A., Devenport, W., Morton, M. A., and Glegg, S. A. L., Noise from a rotor ingesting a planar turbulent boundary layer. AIAA 19th Aeroacoustics Conference, Berlin, Germany (2013)
24. Ffowcs Williams J.E. and Hawkings, D.L. Sound from turbulence and surfaces in arbitrary motion *Proceedings of the Royal Sociey(London) Series A* **264** (1969) 321-342
25. Amiet, R.K., Gust response of a flat-plate aerofoil in the time domain *The Quarterly Journal of Mechanics and Applied Mathematics.* **39** (1986) 485-505
26. Leishman J.G., Principles of helicopter aerodynamics, *Cambridge University Press,* (2000)
27. Devenport,W J, Burdisso, R A, Borgoltz, A, Ravetta, P A, Barone, M F, Brown, K A, and Morton, M A, 2013, The Kevlar-Walled Anechoic Wind Tunnel, *Journal of Sound and Vibration*, http://dx.doi.org/10.1016/ j.jsv.2013.02.043i
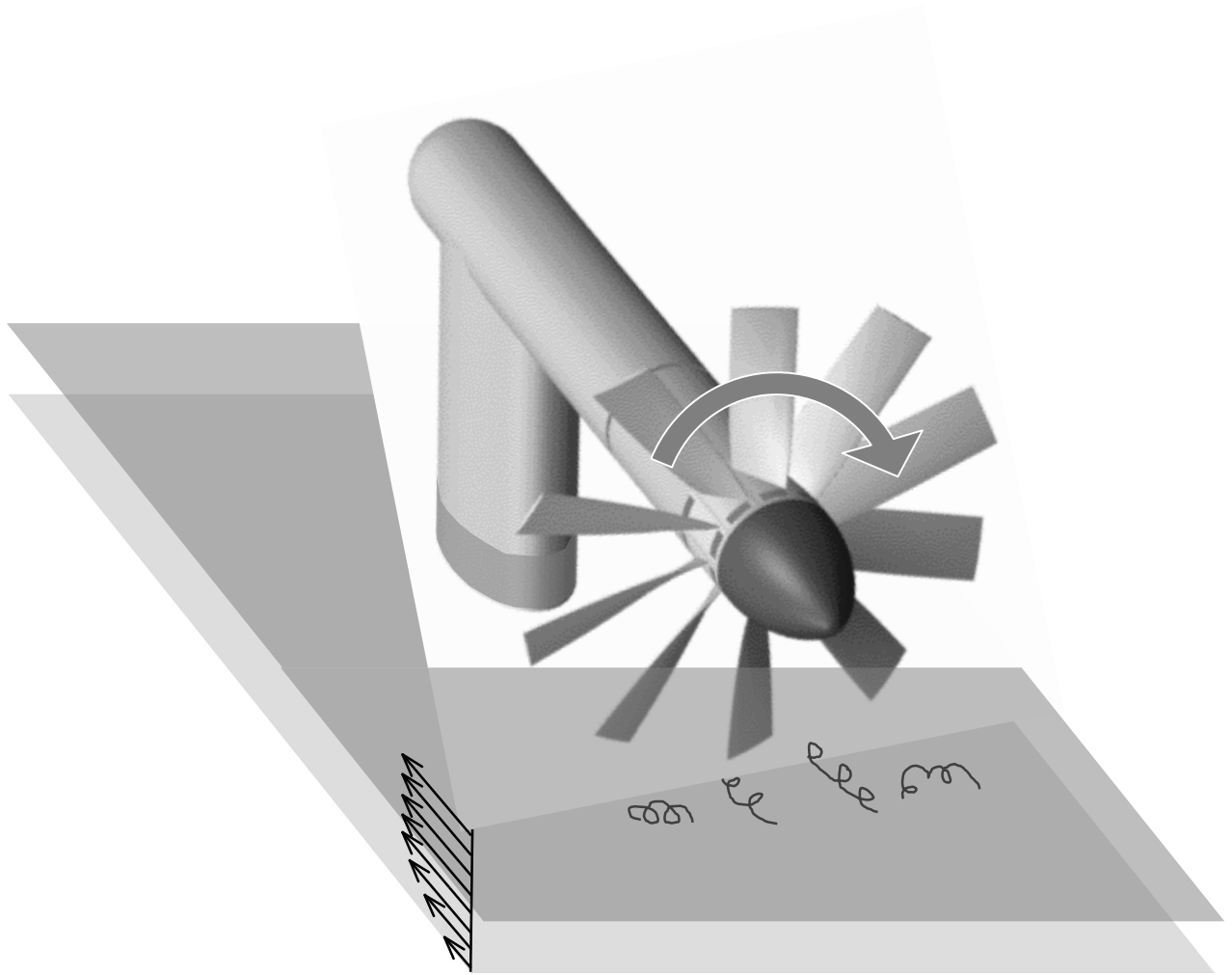
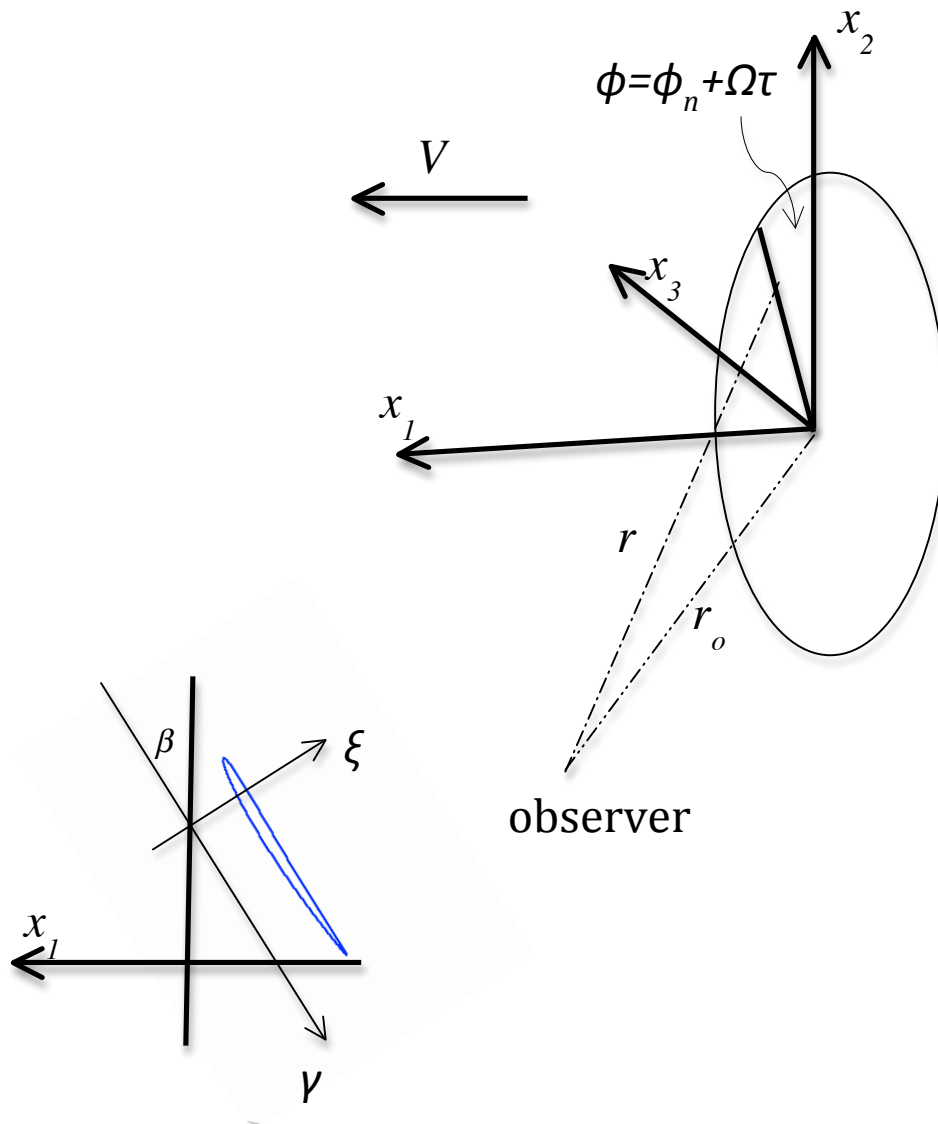Figure 1: The configuration of the Sevik rotor used in the experimental measurements

Figure 2: The coordinate system showing the rotor disc plane and the observer location.
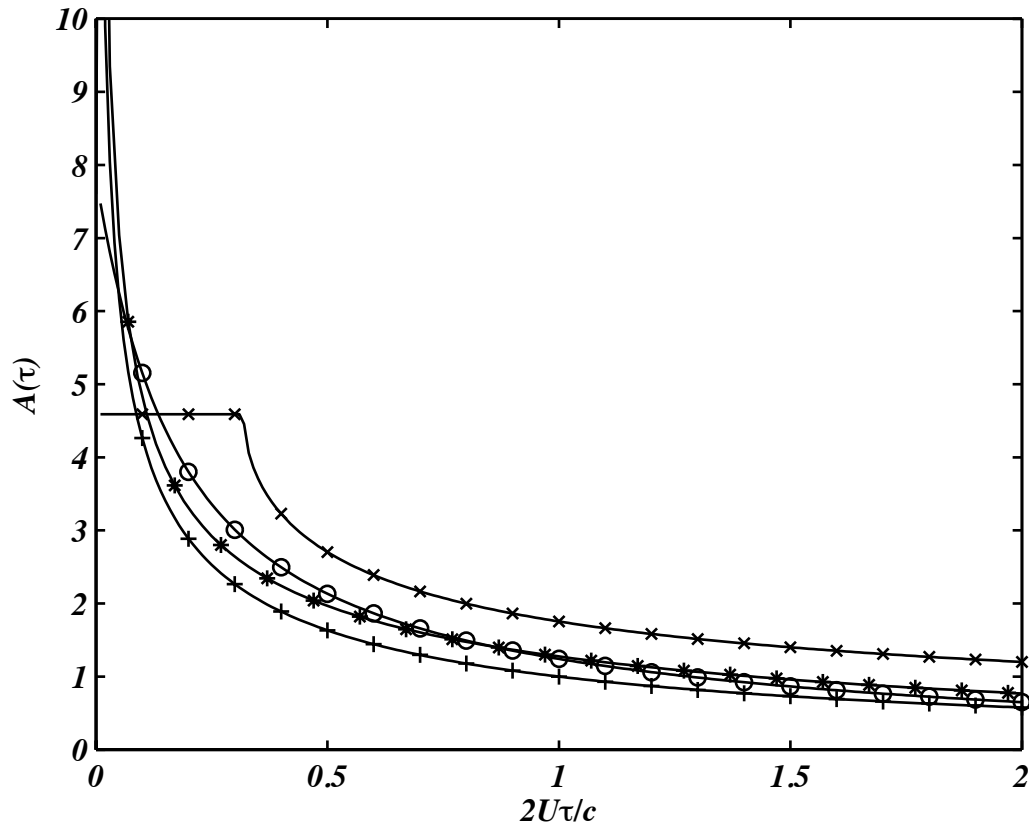
Figure 3: The non dimensional lift response function $A(\tau)=s(\tau)/\rho U^2$ for delta function gust based on different theories as a function of the non dimensional time lag $2U\tau/2$. Sears response function -*-, approximate Sears response function -+-, Kussner function, -o-, Amiet response function -x-. Calculations carried out for a Mach number $M=0.19$.
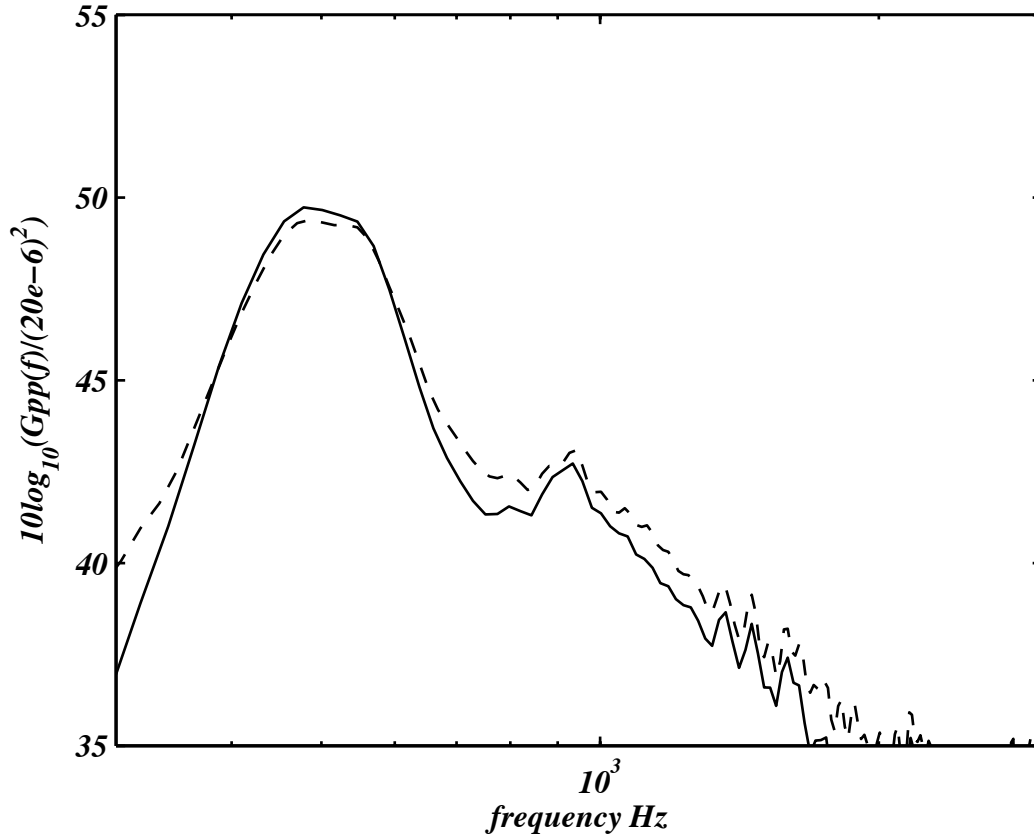
Figure 4: The effect of the analysis bandwidth on the predicted spectra. The calculation is for the 10 bladed Sevik rotor at 2734 rpm, an advance ratio $J=1.44$ and an observer angle of 29°. The solid curve uses an averaging time of two rotor revolutions and the dashed curve averages over three revolutions. The time step for both calculations is $\Omega\Delta\tau=2\pi/128$.
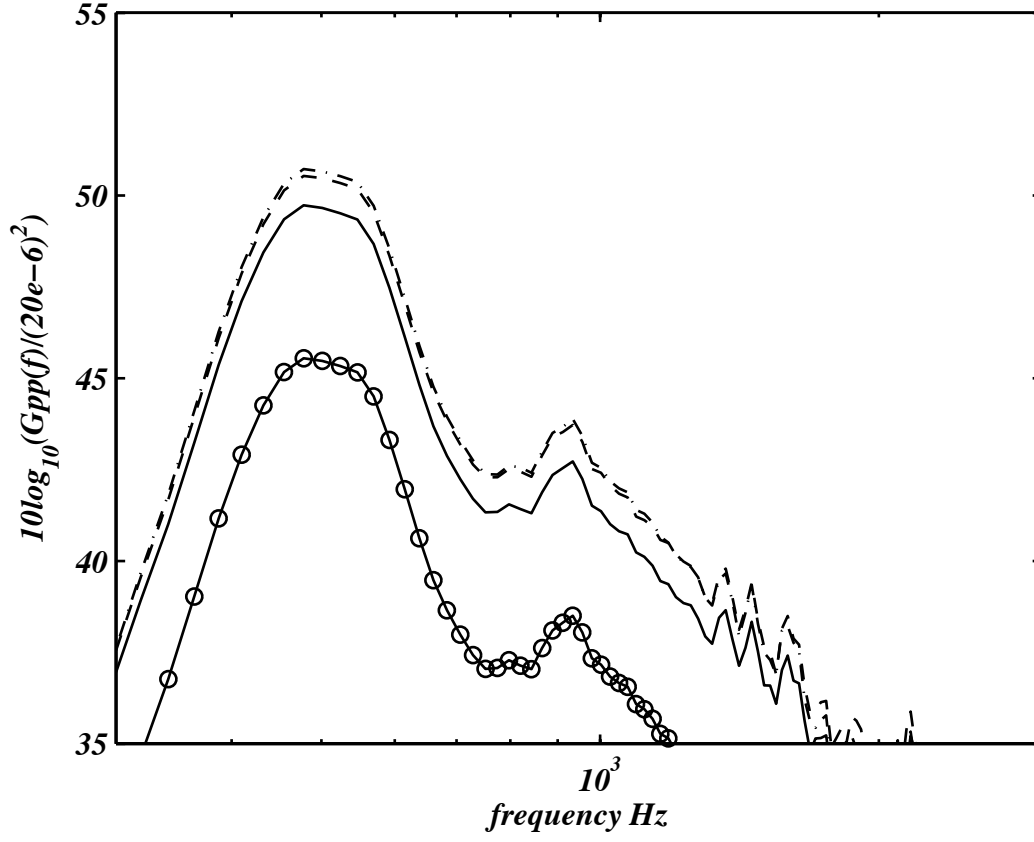
Figure 5: The effect of the blade response function on the predicted spectra. The calculation is for the 10 bladed Sevik rotor at 2734 rpm, an advance ratio $J=1.44$ and an observer angle of 29°. —— Amiet response function $\Omega\Delta\tau=2\pi/128$, ---- Amiet response function $\Omega\Delta\tau=2\pi/154$, $-\cdot-\cdot-$ Amiet response function $\Omega\Delta\tau=2\pi/192$, -o-o- Sears response function $\Omega\Delta\tau=2\pi/128$.
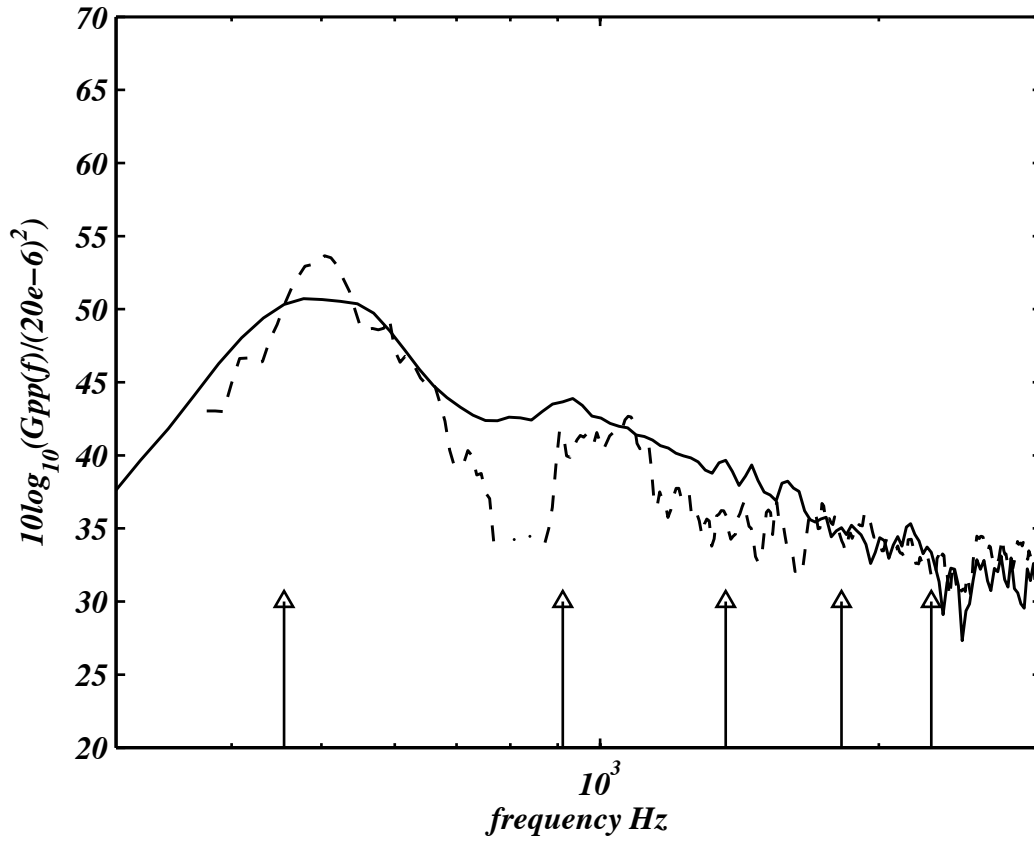
Figure 6: Comparison between measured (dashed line) and predicted spectra (solid line). The calculation is for the 10 bladed Sevik rotor at 2734 rpm, an advance ratio $J=1.44$ and an observer angle of 29º. Vertical lines give the blade passing frequencies.
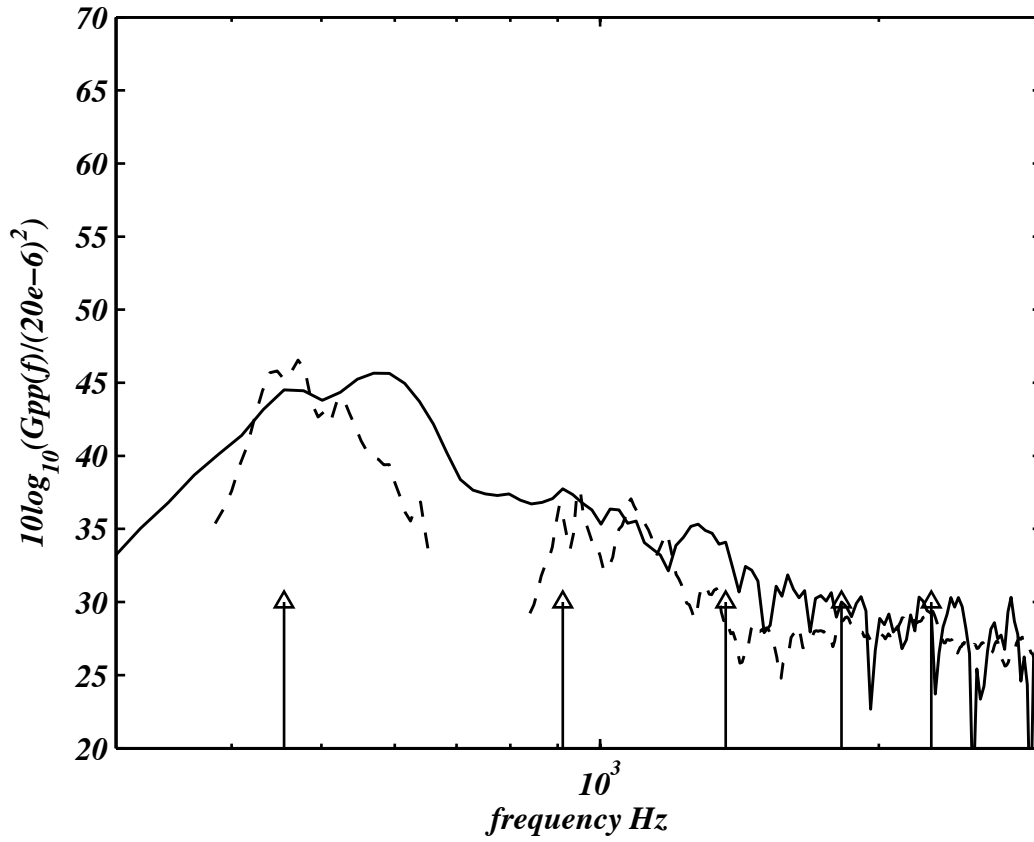
Figure 7: Comparison between measured (dashed line) and predicted spectra (solid line). The calculation is for the 10 bladed Sevik rotor at 2734 rpm, an advance ratio *J=1.44* and an observer angle of 52º. Vertical lines give the blade passing frequencies.
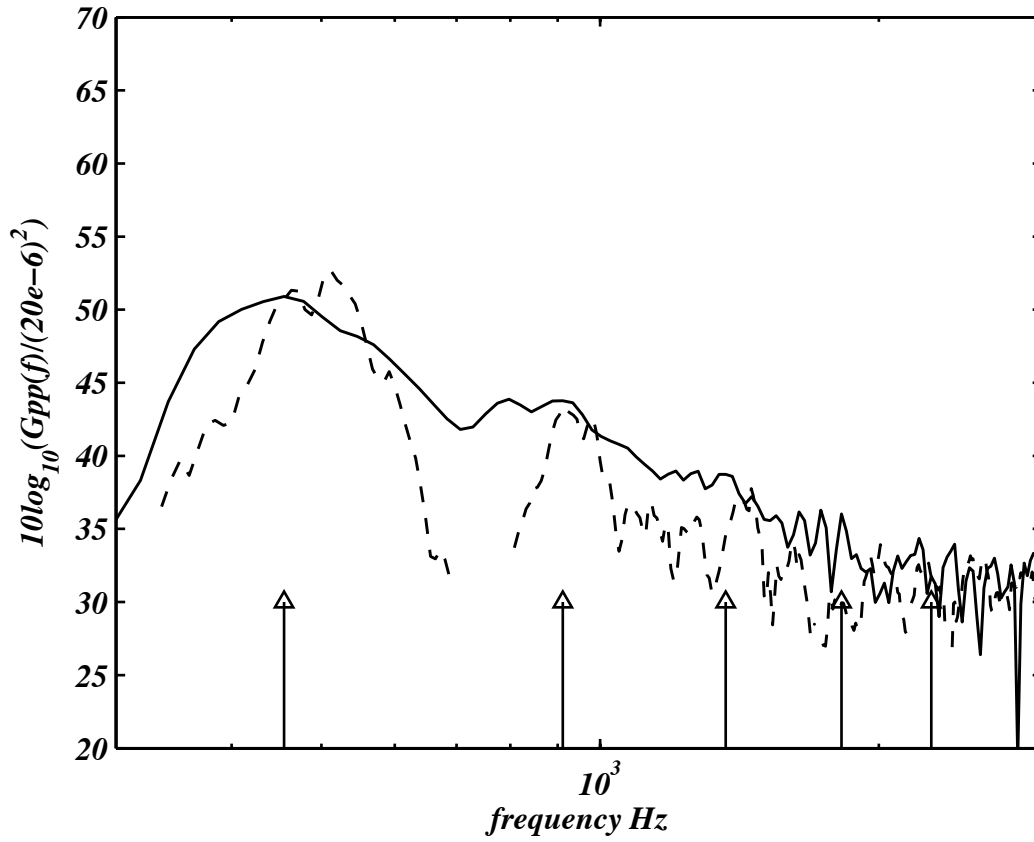
Figure 8: Comparison between measured (dashed line) and predicted spectra (solid line). The calculation is for the 10 bladed Sevik rotor at 2734 rpm, an advance ratio *J=1.44* and an observer angle of 142º. Vertical lines give the blade passing frequencies.

Part II: Rapid Distortion Theory For Rotor Inflows

Adapted from Emilia Kawashima's Masters Thesis

1. Introduction

Rotor noise caused by inflow turbulence is of interest in aerospace and naval applications where low radiated noise levels are a requirement. For a thrusting rotor the inflow turbulence is stretched and distorted as it enters the rotor and this effect can have a significant impact on the noise source levels. Many studies have been conducted to analyze the deformation of turbulent flow as it is ingested into a rotor and the sound radiation from this interaction. This report will focus on studying the distortion of turbulent inflows to a rotor and its effect on radiated noise. The main focus will be on a complicated rotor inflow that occurs when the rotor is embedded in a turbulent boundary layer. More specifically, this report will focus on how these inflows can be analyzed using Rapid Distortion Theory (RDT). The basic concept of RDT is that eddies in a turbulent flow are convected so rapidly that their evolution is determined by the mean flow distortion and non-linear effects can be ignored. In order to describe complicated flows with RDT, the theory must be verified with simpler cases. Some flows that will be considered include a pure strain (parallel) flow, a flow in a solid body rotation, a potential vortex flow, the flow over a step and both potential flows and boundary layer (shear) flows ingested by a rotor.

A significant number of studies have been carried out both theoretically, numerically and experimentally to predict sound radiation from rotor inflow turbulence distortion. However, the majority of research up to this point has been for potential mean flows and not for mean shear flows such as a turbulent boundary layer. Goldstein's (1978) approach using RDT showed that a potential flow upstream of a 3-D obstacle or a non-lifting 2-D obstacle is uniform enough to ensure that the imposed distortion field will act like a small disturbance on a constant velocity mean flow. However, the Goldstein approach cannot be readily applied in a shear flow and so its application is limited. Martinez (2006) also considered RDT in a shear flow but did not provide a closed form solution for both pressure waves and vortical waves. Studying these approaches and providing a closed form solution using RDT in a shear flow will play a major role in the completion of this work. By doing so, the RDT for various flows will be considered and the characteristics of the inflow distortion for different inflows will be examined in detail.

2. Previous Studies

2.1 Noise from Rotating Blades

Sevik (1971) analyzed broadband noise radiated from a rotor subjected to upstream turbulence. He stated that random pressure fluctuations within a turbomachine which creates broadband sound radiation can be due to turbulence generated upstream, boundary layer turbulence at duct walls, vortex shedding from blade trailing edges, and random variations of the tip vortex strength. He calculated the power spectral density of radiated sound pressure by determining the spectrum tensor of axial force fluctuations acting on a rotor from the aerodynamic response functions and the correlation tensor of the turbulent velocities. In general the comparison of the predicted spectrum levels to experimental results from a 10-bladed rotor, subjected to grid turbulence, showed good agreement but he was unable to predict the spectral humps near blade passing frequencies (BPF).

This issue was addressed in a theoretical and experimental study by Hanson (1974) of the noise spectra and blade loading in a turbofan engine that was caused by the fan interacting with inlet turbulence on an open engine test stand. Hanson showed that the majority of the noise was caused by atmospheric turbulence ingested by the engine inlet. The turbulence was shown to be highly anisotropic and the associated noise was partially coherent with narrow spectral peaks that were difficult to distinguish from blade passage frequency harmonics caused by the mean flow. This behavior, where spectral peaks occur at the blade passing frequencies (BPF) in the radiated noise spectrum, is known as haystacking. Theoretical spectrum predictions using random pulse modulation theory indicated that the peaks at the BPFs and the high-frequency broadband noise were both due to inflow turbulence. Two cases were considered in Hanson's study: a static rotor and a forward flight case. In the static case, turbulent eddies were pulled into the rotor and there was significant eddy elongation. In the forward flight case, the rotor approached the turbulent flow and there was no significant modification of the eddies before entering the rotor. The theoretical model showed that the blade forces were generated by discrete turbulence eddies with random characteristics. Experimental results showed that the inflow turbulence contained long, narrow eddies of moderately high intensity (2-3%). The ratio of streamwise to transverse integral length scales for turbulence was measured as 400:1. Eddies were observed narrower than the rotor diameter causing short, distinct lift pulses at blade passage intervals, which lead to a blade lift spectrum with significant levels at high frequencies. As long eddies pass through the rotor, they are chopped many times causing partial coherence in fluctuating blade lift. The blade pressure spectrum also showed peaks centered at multiples of shaft rotational frequency.

Majumdar and Peake (1998) reconsidered this problem and analyzed noise generation by the interaction between ingested turbulence of a steady, non-uniform mean flow and a rotating fan. A theoretical model was developed that showed how the unsteady distortion noise was caused by the ingestion of atmospheric turbulence into the fan. Deformation of turbulent eddies into long, narrow filaments occurred when entering into the engine due to strong stream tube contraction upstream of fan. The non-uniform inflow causes the streamwise lengthscale of the turbulent eddies to increase and the transverse scale to decrease. The long, narrow filaments were accelerated through the fan and were consequently sliced a number of times by the blades. This repeated chopping of the eddies produced an unsteady pressure distribution on the blades which generated sound that was scattered into the far field. Rapid Distortion Theory (RDT) in the

wavenumber domain was used for obtaining the distorted turbulent field at the face of the fan, which was simplified by assuming a large number of blades.

2.2 Rapid Distortion Theory

RDT has been frequently used to describe the evolution of a small scale turbulent eddy in a steady mean flow. It assumes eddy vorticity is conserved in turbulent fluid undergoing rapid stretching, while shear production of turbulence remains zero or unchanged. RDT was introduced by Batchelor and Proudman (1954) and variations to their original approach have been given by Townsend (1969) and Hunt and Carruthers (1990). The extension of these concepts to compressible irrotational flow was given by Goldstein (1978) and Goldstein's approach has been used extensively for problems in aeroacoustics (Attasi (1994), and Majumdar and Peake (1998)). The basic concept is that coherent structures in a turbulent flow are convected so rapidly that their evolution is completely determined by the mean flow distortion and non-linear effects can be ignored.

The theory given by Batchelor and Proudman (1954) is based on the linearized solution to the vorticity equation and gives the distortion of a harmonic gust. The difficulty with this solution is obtaining a suitable definition of the upstream vorticity and then inverting the downstream vorticity to obtain the distorted gust velocity. In contrast, Townsend (1969) gives a formulation for a harmonic gust but his solution depends on solving a Poisson's equation for the pressure and analytical solutions are only available for potential mean flows and flows with linear shear. Goldstein (1978) presented RDT for compressible flows and showed that in a potential flow the velocity associated with the pressure fluctuations in the flow was separable from the distortion of an upstream vortical gust. However they are coupled by the continuity equation, and, in the incompressible case, a Poisson's equation still has to be solved to obtain the complete solution. Goldstein's solution for the evolution of the vortical gust cannot be used for shear flows, and additional boundary conditions are required if the flow includes a stagnation point (Atassi (1986)). The main difficulty in applying any of these theories for RDT is that a Poisson's equation, either for the velocity potential or for the vorticity, has to be solved to obtain the downstream gust and that solution is limited by both upstream and downstream boundary conditions. To overcome this problem Majumdar and Peake (1998) introduced a high frequency asymptotic solution for the velocity potential in Goldstein's solution giving a closed form result for a harmonic gust.

Goldstein (1978) studied the unsteady distortions of potential flows around an arbitrary obstacle using RDT. He considered small amplitude vortical and entropic unsteady motions imposed on steady potential flows where RDT was utilized to predict changes occurring in weakly turbulent flows distorted by solid obstacles in a time short relative to the Lagrangian integral scale. A main concern of aerodynamics and hydrodynamics is high Reynolds number flows produced by solid bodies moving through a fluid at rest or with stationary bodies embedded in nearly inviscid flows that have constant velocity and physical properties far upstream. Studies were done of the unsteady flow produced when small amplitude upstream distortions are imposed on such flows, which were separated into two cases.

The first case dealt with airfoils and other bodies with at least one small transverse dimension causing only small departures from uniform upstream flow. Such flows are described by equations with constant coefficients and solutions can be found for many different conditions. For this case there is no need to assume incompressible flow or a 2-D body. Gust loading predictions on airfoils, other aerodynamic surfaces, and aeroacoustic investigations of aircraft engine-fan and compressor noise are applications where these assumptions apply.

The second case included flows about bluff bodies and other obstacles that produce a non-negligible disturbance to the upstream flow. These flows are described by equations with variable coefficients unless the flow is assumed incompressible. The first study on this flow was carried out by Lighthill (1956), who imposed an upstream vorticity field independent of time but which varied in space. RDT of the turbulence was used for the most general upstream vorticity field consistent with assumption that it represented a small disturbance of a uniform flow. This was extended by Hunt (1973) using the approaches of Ribner-Tucker (1953) and Batchelor-Proudman (1954). Goldstein's main objectives were to develop a unified approach to deal with both flow cases mentioned above and to use this approach to study more general classes of flow. An important observation Goldstein made was that potential flow upstream of a 3-D obstacle or a non-lifting 2-D obstacle is uniform enough to ensure that the imposed distortion field will act like a small disturbance on a constant velocity mean flow.

However, the Goldstein approach cannot be readily applied in a shear flow and so its application is limited. The interest of this study is to apply RDT to turbulent flow distortion in more complicated flows such as boundary layer flows (with shear) and to determine if it can be used to study the structure of turbulence as discussed by Hunt and Carruthers (1990). Hunt and Carruthers focused on local-scale turbulent structures determined by local shear and the presence of nearby boundaries. They showed that these structures were equivalent to a 'statistical eigensolution,' or linear solutions after statistical averaging, to the linear RDT analysis. It was shown that the structures formed at these local scales dominated the coherent structures in mature shear flows.

More recently Gobluev and Atassi (1998) considered the case of a swirling flow in a duct and identified that the effect of shear was to cause waves that were almost compressible and almost incompressible. Also Martinez (2006) also considered RDT in a shear flow but did not provide a closed form solution for both the pressure waves and the vortical waves.

3. Theoretical Approach

The approach used in this study is based on the theories presented by Batchelor and Proudman and Goldstein. Batchelor and Proudman (1954) showed the evolution of a turbulent flow could be described by Cauchy's solution to the vorticity equation and assumed that the turbulence was simply convected by the mean flow. This implies that the scale of the mean flow is large compared to the size of the turbulent structures and that the evolution of the turbulence was determined completely by the mean flow. Goldstein presented a solution for RDT in a compressible potential flow. It will be shown below how Goldstein's solutions combined with linearized Euler equations in a shear flow (Hunt and Carruthers (1990)) can be solved by introducing an additional potential function, providing the distortion of the mean shear by the turbulence is negligible. The resulting equations for the unsteady potential and unsteady vortical waves will be shown to be uncoupled for an incompressible flow, and coupled for the case of a compressible mean flow with shear.

3.1 The Batchelor and Proudman Approach

To summarize Batchelor and Proudman's (1954) results we will consider the flow velocity at the location $\mathbf{x}$ as defined as the sum of the mean flow $\mathbf{U(x)}$ and the turbulent flow $\mathbf{u(x,}t)$ where t is time. If the vorticity, $\boldsymbol{\omega} = \nabla \times \mathbf{u}$, is specified as a function of the Lagrangian coordinate $\mathbf{z(a,}\tau)$ where $\mathbf{z}$ is the location of the particle that was located at $\mathbf{a,}$ and has been convected by the mean flow for a time interval τ, then Cauchy's equation gives

3.1.1

$$\omega_i(\mathbf{x},t) = \frac{\partial z_i}{\partial a_j}\omega_j(\mathbf{a},t-\tau)$$

The basis of RDT is that the distortion tensor $\partial z_i/\partial a_j$ is determined entirely by the mean flow and that the turbulence itself does not alter the streamlines of the flow. This is ofcourse an important simplification to linearized theory of turbulence evolution and only applies if the mean shear Ω is much less than U/L where U is the mean flow speed and L is the lengthscale of the turbulence. Hence if the mean flow is known we can use Batchelor and Proudman's theory to calculate the evolution of the turbulence. The problem however is to determine the velocity disturbance from the vorticity disturbance, which requires an application of the Biot Savort law and the assumption of an incompressible flow. For harmonic gusts it is relatively straightforward to apply this approach but for calculations in space and time it becomes more difficult numerically.

Goldstein (1978) considered RDT in a compressible flow and obtained a more general result by splitting the unsteady velocity into a potential flow determined by the unsteady pressure p' and a remaining part $\mathbf{u}^{(g)}$ so,

3.1.2

$$\mathbf{u} = \mathbf{u}^{(g)} + \nabla\phi \qquad \frac{D_o\phi}{Dt} = -\frac{p'}{\rho_o}$$

where ρ_o is the density of the mean flow and $D_o/Dt = \partial/\partial t + U_j \partial/\partial x_j$ is the total time derivative in the frame of reference moving with the mean flow. Goldstein showed that for a vortical gust in an irrotational mean flow the solution to the linearized Euler equations could be reduced to a single equation for $\mathbf{u}^{(g)}$, which has a simple solution in terms of the upstream boundary conditions and drift coordinates (Lighthill (1956)).

For the case of a vortical gust in an incompressible irrotational mean flow Goldstein (1978) showed that

$$3.1.3$$

$$\mathbf{u}^{(g)} = \nabla X_k A_k (X_1 - U_\infty t, X_2, X_3) \qquad\qquad \nabla^2 \phi = -\nabla . \mathbf{u}^{(g)}$$

where $\mathbf{A}$ is the velocity of the gust at a large distance upstream of the mean flow distortion, and X_1, X_2, X_3 are the drift coordinates defined as the solutions to the first order differential equations:

$$3.1.4$$

$$\frac{D_o X_1}{Dt} = U_\infty \qquad\qquad \frac{D_o X_2}{Dt} = 0 \qquad\qquad \frac{D_o X_3}{Dt} = 0$$

The coordinate X_1 is described as the drift because surfaces of constant X_1 represent the locations of particles after they have been convected by the mean flow for the same amount of time along a streamline, and the speed U_∞ is constant and loosely defined as the speed of the mean flow far upstream of the region of interest. It is used as a reference velocity. For example if the particles are on the surface $X_1=0$ at time $t=0$ then the same particles will lie on the surface $X_1 = U_\infty \tau$ after they have been convected by the mean flow for a time $t = \tau$ (see Figure 1). The surfaces $X_2 = constant$ and $X_3 = constant$ represent the stream surfaces and the unit vectors normal to those surfaces are orthogonal to each other and to the direction of the mean flow (see Figure 1).

It is interesting to note that the Batchelor and Proudman approach is really just an implementation of Kelvin's circulation theorem which states that for a barotropic flow the circulation around the contour $ABCD$ in Figure 1 will be the same as the circulation around the contour $A'B'C'D'$ at a time τ later. This applies in both a potential mean flow and a sheared mean flow. Goldstein's solution $\mathbf{u}^{(g)}$ obviously satisfies the same requirement for a potential mean flow, but since it is only a function of the drift it must also satisfy Kelvins theorem for a rotational mean flow, providing the drift coordinates take the mean flow shear into account. Consequently, to correct Goldstein's solution so that it applies in a rotational flow we will add an unsteady potential flow correction such that

$$3.1.5$$

$$\mathbf{u} = \mathbf{u}^{(g)} + \nabla \phi + \nabla \varphi \qquad\qquad \frac{D_o \phi}{Dt} = -\frac{p'}{\rho_o}$$

In the following section we will show that this form of solution, which only applies to a weak shear flow where $\Omega << U/L$, can be used to give two equations for the unknown potentials ϕ and φ that are uncoupled in an incompressible flow or a potential mean flow, but coupled for the case of a weakly compressible mean shear flow.

3.2 The Linearized Euler Equations in a Shear Flow

The linearized Euler equations are well known and defined for an incompressible flow with no body forces (Hunt and Carruthers (1990)) as

3.2.1

$$\frac{D_o \mathbf{u}}{Dt} + (\mathbf{u}.\nabla)\mathbf{U} = \frac{-1}{\rho_o}\nabla p$$

(This equation also applies to an isentropic compressible flow that will be considered at the end of this section). Expanding the unsteady velocity as given in equation 3.1.5 then gives

3.2.2

$$\frac{D_o(A_k\nabla X_k + \nabla\phi + \nabla\varphi)}{Dt} + ((A_k\nabla X_k + \nabla\phi + \nabla\varphi).\nabla)\mathbf{U} = \nabla\left(\frac{D_o\phi}{Dt}\right)$$

We then use vector identities to show that

3.2.3

$$\frac{D_o(\nabla\phi)}{Dt} + (\nabla\phi.\nabla)\mathbf{U} = \nabla\left(\frac{D_o\phi}{Dt}\right) - \nabla\phi\times\mathbf{\Omega}$$

where $\mathbf{\Omega}$ is the mean flow vorticity. Since each term in equation 3.2.2 is a potential function and $D_oA_k/Dt=0$, equation 3.2.2 reduces to

3.2.4

$$\nabla\left(\frac{D_o\varphi}{Dt}\right) = \mathbf{u}\times\mathbf{\Omega}$$

Hence if we define $\phi_e=\phi+\varphi$ we find that the flow is completely defined for an incompressible shear flow by the solution to

3.2.5

$$\nabla^2\phi_e = -\nabla.(\nabla X_k A_k(\mathbf{X} - \mathbf{i}U_\infty t)) \qquad\qquad \mathbf{u} = \nabla\phi_e + \nabla X_k A_k(\mathbf{X} - \mathbf{i}U_\infty t)$$

where A_k is equal to the unsteady velocity at the upstream boundary. The interesting feature of this result is that it shows the equations that apply to a potential flow (equation 3.1.3) are equally applicable to a shear flow, the difference being that the pressure is no longer defined by the unsteady potential. However the pressure can still be obtained by solving equation 3.2.4, which depends on the mean flow vorticity.

These results can be extended to an isentropic compressible flow by using the approach given by Goldstein (1978). This results in two coupled equations for the two potentials that take the form

3.2.6

$$\nabla(\phi+\varphi)\times\Omega+\nabla\left(\frac{D_o\varphi}{Dt}\right)=\mathbf{u}^{(g)}\times\Omega$$

$$\frac{D_o}{Dt}\left(\frac{1}{c_o^2}\frac{D_o\phi}{Dt}\right)-\nabla^2(\phi+\varphi)=-\nabla.\mathbf{u}^{(g)}$$

In conclusion, we see that these equations are uncoupled in a potential mean flow and for an incompressible flow, and coupled for the case of a compressible mean flow with shear. However to complete the solutions for an incompressible flow a Poisson's equation must be solved for the velocity potential, and in a compressible flow the solution to a wave equation with non-constant coefficients is required. One of the implicit assumptions is that the circulation about a closed circuit convected by the mean flow is constant. This does not apply in strongly sheared flows in which the circulation around the contour *A'B'C'D'* in Figure 1 is increased by the distortion of the mean shear by the turbulence. To correct for this an additional rotational component $\mathbf{u}^{(s)}$ must be added to equation 3.1.5 and equation 3.2.4 becomes

3.2.7

$$\nabla\left(\frac{D_o\varphi}{Dt}\right)=(\mathbf{u}-\mathbf{u}^{(s)})\times\Omega-\frac{D_o\mathbf{u}^{(s)}}{Dt}-(\mathbf{u}^{(s)}.\nabla)\mathbf{U}$$

In the following we will not include this correction and make the assumption of weak shear so that the term $\mathbf{u}^{(s)}$ can be ignored.

3.3 Incompressible Flow and Drift Coordinates

The solution to equation 3.2.5 for an incompressible flow is given by

3.3.1

$$u_i=\frac{\partial X_k}{\partial x_i}A_k(\mathbf{X}-iU_\infty t)-\frac{\partial^2}{\partial x_i\partial x_j}\int_V\frac{\partial X_k'}{\partial x_j'}A_k(\mathbf{X}'-iU_\infty t)G(\mathbf{x}\mid\mathbf{x}')dV(\mathbf{x}')$$

where G is a Green's function for Laplace's equation that satisfies the boundary conditions on the surfaces bounding the flow. In an unbounded flow $G=1/4\pi|\mathbf{x}-\mathbf{x'}|$, which is referred to as the free-space Green's function. In general the volume integral is difficult to evaluate numerically since it is singular at $\mathbf{x}=\mathbf{x'}$. Majumdar and Peake (1998) give an approximate solution to this equation for a harmonic gust that is more readily computed. The approximation is based on the assumption that the gust wavelength is much smaller than the magnitude of the drift coordinate and gives

3.3.2

$$u_i=\left(\delta_{im}-\frac{\kappa_i\kappa_m}{|\kappa|^2}\right)\frac{\partial X_k}{\partial x_m}\tilde{A}_k(\mathbf{k})\exp(i\mathbf{k}.\mathbf{X}-iU_\infty t)\qquad\kappa_i=k_m\frac{\partial X_m}{\partial x_i}$$

To compute the drift coordinates we first compute the corner points of each drift cell, defined by *A'B'C'D'* in Figure 1 and this allows us to define the vectors $\delta\mathbf{l}^{(i)}$ as shown in Figure 2. It follows that $\delta\mathbf{l}^{(i)}.\nabla X_i=h_i$ and correspondingly the volume of the cell is $\delta\mathbf{l}^{(1)}.(\delta\mathbf{l}^{(2)}\times\delta\mathbf{l}^{(3)})=h_1h_2h_3$ (if the mean flow is incompressible). It then follows that

$$\nabla X_i = \frac{\delta \mathbf{l}^{(j)} \times \delta \mathbf{l}^{(k)}}{h_j h_k} \qquad (i,j,k) = (1,2,3),(2,3,1) \text{ or } (3,1,2)$$

and $\delta \mathbf{l}^{(i)}.\nabla X_j = \delta_{ij} h_i$.

However, implementing the solution to equation 3.3.1 requires an integral of the flow variables over a large volume in order to compute the potential part of the flow. Computationally and intuitively this has always been a significant limitation of rapid distortion theory. At a early stage in this project a solution was sought in terms of a variable lengthscale. However this was later shown to incorrectly distort the phase of the gust and so was discarded, and will not be discussed here. In the next section we will show how calculations can be carried out for an incompressible gust in the high frequency limit.

3.4 Majumdar and Peake Approach

The high frequency RDT solution given by Majumdar and Peake (1998) is given by

3.4.1

$$u_i(\mathbf{k},\mathbf{X}) = (\delta_{im} - \kappa_i \kappa_m / \kappa^2) \frac{\partial X_k}{\partial x_m} \tilde{A}_k(\mathbf{k}) e^{i\mathbf{k}.(\mathbf{X}-iU_\infty t)} \qquad \kappa_i = k_j \frac{\partial X_j}{\partial x_i}$$

where κ is the distorted wavenumber. In order to verify these solutions, we will write this solution in vector notation as

3.4.2

$$\mathbf{u} = \mathbf{u}^{(g)} - \hat{\boldsymbol{\kappa}}(\hat{\boldsymbol{\kappa}}.\mathbf{u}^{(g)}) \qquad \mathbf{u}^{(g)} = \nabla X_k \tilde{A}_k(\mathbf{k}) e^{i\mathbf{k}.(\mathbf{X}-iU_\infty t)} \qquad \hat{\boldsymbol{\kappa}} = \boldsymbol{\kappa}/|\boldsymbol{\kappa}|$$

Using the vector triple product we obtain

3.4.3

$$\mathbf{u} = \hat{\boldsymbol{\kappa}} \times (\mathbf{u}^{(g)} \times \hat{\boldsymbol{\kappa}})$$

which shows that the magnitude of the unsteady velocity is given by

3.4.4

$$|\mathbf{u}| = |\mathbf{u}^{(g)}| \sin\theta_g$$

where θ_g is the angle between the distorted wavenumber $\boldsymbol{\kappa}$ and the local gust $\mathbf{u}^{(g)}$, so

3.4.5

$$\cos\theta_g = \frac{\hat{\boldsymbol{\kappa}}.\mathbf{u}^{(g)}}{|\mathbf{u}^{(g)}|}$$

Determining θ_g is important because it shows the unsteady velocity dependence on the potential flow correction. If θ_g is $\pi/2$ then there is no need for a potential flow correction; however, if θ_g is small then the potential correction is significant. For two dimensional turbulent flows with unidirectional vorticity we can define an upstream gust and wavenumber as

$$3.4.6$$

$$\tilde{A}_1 = a_o \cos\phi \qquad k_1 = k_o \sin\phi$$
$$\tilde{A}_2 = a_o \sin\phi \qquad k_2 = -k_o \cos\phi$$

where ϕ is the angle at which the incoming upstream gust is travelling. It then follows that

$$3.4.7$$

$$u_1^{(g)} = a_o\left(\frac{\partial X_1}{\partial x_1}\cos\phi + \frac{\partial X_2}{\partial x_1}\sin\phi\right) \qquad \kappa_1 = k_o\left(\frac{\partial X_1}{\partial x_1}\sin\phi - \frac{\partial X_2}{\partial x_1}\cos\phi\right)$$

$$u_2^{(g)} = a_o\left(\frac{\partial X_1}{\partial x_2}\cos\phi + \frac{\partial X_2}{\partial x_2}\sin\phi\right) \qquad \kappa_2 = k_o\left(\frac{\partial X_1}{\partial x_2}\sin\phi - \frac{\partial X_2}{\partial x_2}\cos\phi\right)$$

and so we obtain the following relationship

$$3.4.8$$

$$\frac{|\boldsymbol{\kappa}|\left|\mathbf{u}^{(g)}\right|\cos\theta_g}{a_0 k_0} = \left(\nabla X_1.\nabla X_2\right)\left(\sin^2\phi - \cos^2\phi\right) + \left(\left|\nabla X_1\right|^2 - \left|\nabla X_2\right|^2\right)\sin\phi\cos\phi$$

where we will assume a gust of initial unit amplitude and unit wavenumber so that $a_0 = k_0 = 1$. By using this relationship, values of θ_g can be determined which contribute to the potential flow correction. Note equation 3.4.8 shows that $\cos\theta_g$ is zero if $\phi=0$ or $\pi/2$ and $\partial X_1/\partial x_2 = \partial X_2/\partial x_1 = 0$ which would imply $|\mathbf{u}| = |\mathbf{u}^{(g)}|$. In this case, the potential flow correction is not needed when determining the unsteady flow velocity. Flows in which this case applies will be studied in the next section.

3.4.1 Vector representation method for potential flows

We can consider an additional approach specifically for potential flows, which is a variation of the M&P vector representation method. This method will be used for validating the turbulence in a potential vortex and a potential flow over a step in latter sections of this thesis as well as verifying the method presented previously. The drift coordinate gradients for a two dimensional potential flow are defined as

$$3.4.9$$

$$\nabla X_1 = \frac{U_\infty}{U}\hat{\mathbf{s}} + f(\mathbf{X})\hat{\mathbf{n}} \qquad \nabla X_2 = \frac{U}{U_\infty}\hat{\mathbf{n}}$$

where $\mathbf{s}$ and $\mathbf{n}$ are vectors in the direction of the mean flow and normal to the mean flow. In this case we can write equation 3.4.8 as the following

$$3.4.10$$

$$|\boldsymbol{\kappa}|\left|\mathbf{u}^{(g)}\right|\cos\theta_g = \frac{Uf(\mathbf{X})}{U_\infty}\left(\sin^2\phi - \cos^2\phi\right) + \left(\left(\frac{U_\infty}{U}\right)^2 + f^2 - \left(\frac{U}{U_\infty}\right)^2\right)\sin\phi\cos\phi$$

To obtain the function f we note that for a 2D potential flow

$$3.4.11$$

$$X_1 = \int \frac{U_\infty}{U} ds = \int \frac{U_\infty}{U^2} d\Phi$$

$$X_2 = \frac{\Psi}{U_\infty}$$

where Φ and Ψ are the potential and stream functions for the mean flow, respectively. Hence we have

$$3.4.12$$

$$f = \int \frac{\partial}{\partial \Psi}\left(\frac{U_\infty^2}{U^2}\right) d\Phi$$

This gives a relatively simple set of equations for a 2D potential flow that identifies the characteristics of the distortion and will be used in subsequesnt sections to investigate different types of wave.

3.5 Conclusion

The theory given by Batchelor and Proudman (1954) is based on the linearized solution to the vorticity equation and gives the distortion of a harmonic gust. Batchelor and Proudman showed the evolution of a turbulent flow could be described by Cauchy's solution to the vorticity equation and assume that the turbulence was simply convected by the mean flow. This implies that the scale of the mean flow is large compared to the size of the turbulent structures and that the evolution of the turbulence was determined completely by the mean flow. The difficulty with this solution is obtaining a suitable definition of the upstream vorticity and then inverting the downstream vorticity to obtain the distorted gust velocity. Goldstein presented a solution for RDT in a compressible potential flow. This section showed how Goldstein's solutions combined with linearized Euler equations in a shear flow (Hunt and Carruthers (1990)) could be solved. The resulting equations for the unsteady potential and unsteady vortical waves were determined to be uncoupled for an incompressible flow, and coupled for the case of a compressible mean flow with shear. The main difficulty in applying any of these theories for RDT is that a Poisson's equation, either for the velocity potential or for the vorticity, has to be solved to obtain the downstream gust and that solution is limited by both upstream and downstream boundary conditions. To overcome this problem Majumdar and Peake (1998) introduced a high frequency asymptotic solution for the velocity potential in Goldstein's solution giving a closed form result for a harmonic gust. This section showed different approaches of the M&P solution including the direct solution and the vector representation. The benefit of this is that both methods give the same result, which will be verified in the next section. The advantage of the vector representation method is that the potential flow correction can be easily calculated.

Since the Goldstein approach cannot be readily applied in a shear flow making its application limited, a solution to the RDT equations based on the concept of a variable lengthscale was explored. It was found after a series of simple studies that this approach did not

maintain consistency between velocity components and so it was not a suitable approximation to the distorted flow.

4. Example Flows

4.1 Introduction

The objective of this section is to give examples of the RDT formulations derived in the previous section to some simple flows. In order to do so, we will evaluate the velocity solutions based on the solution provided by Majumdar and Peake (1998) for various simple flows which include pure strain, solid body rotation, potential vortex and flows over a step.

4.2 Applications to Solid Body Rotation

To investigate a simple flow that includes shear, a mean flow with solid body rotation will be considered in this section. In a solid body rotational flow, velocity is proportional to the radius of the streamlines and the fluid elements spin about their own centers while revolving around the origin of the flow. However there is no change in deformation of the drift cell elements as shown in Figure 3. This simple flow will be examined to determine the evolution of an unsteady vortical wave using Majumdar and Peakes's direct solution and the vector representation approach.

The mean flow for a solid body rotation is $U = \Omega R$ where Ω is the angular velocity of the revolution of each particle about the origin and R is the radius. The solid body rotation flow velocity has two components, U_1 and U_2, which correspond to the velocity in the x_1 and x_2 directions, and are respectively:

$$4.2.1$$

$$U_1 = \Omega R \cos\theta \quad U_2 = \Omega R \sin\theta \quad \text{and} \quad U_3 = 0$$

The reference velocity U_∞ is defined as a constant for the entire flow and it can be chosen to suit the problem being considered. In this case we will choose it as the mean upstream boundary velocity is $U_\infty = \Omega R_o$, where R_o is constant. It follows that the drift coordinates X_1 and X_2 can be defined as

$$4.2.2$$

$$X_1 = \int_0^s \frac{U_\infty}{U} \, ds = \frac{U_\infty}{U} \int_0^\theta R d\theta = R_0 \theta$$

$$X_2 = R$$

The corresponding drift coordinate gradients in spherical coordinates are found to be

$$4.2.3$$

$$\nabla X_1 = \frac{1}{R} \frac{\partial X_1}{\partial \theta} \hat{e}_\theta + \frac{\partial X_1}{\partial R} \hat{e}_r = \hat{e}_\theta$$

$$\nabla X_2 = \frac{1}{R} \frac{\partial X_2}{\partial \theta} \hat{e}_\theta + \frac{\partial X_2}{\partial R} \hat{e}_r = \hat{e}_r$$

In Cartesian coordinates, the drift gradients are given as

$$4.2.4$$

$$\nabla X_1 = \left(\frac{\partial X_1}{\partial x_1} \hat{x}_1, \frac{\partial X_1}{\partial x_2} \hat{x}_2 \right) = (\cos\theta \, \hat{x}_1, -\sin\theta \, \hat{x}_2)$$

$$\nabla X_2 = \left(\frac{\partial X_2}{\partial x_1} \hat{x}_1, \frac{\partial X_2}{\partial x_2} \hat{x}_2 \right) = (\sin\theta \, \hat{x}_1, \cos\theta \, \hat{x}_2)$$

where $\hat{x}_1$ and $\hat{x}_2$ are the directions describing the location of drift in a 2D Cartesian coordinate system. Similar to the pure strain application, we will consider two cases for the unsteady velocity. The first case considers a one-dimensional gust with an upstream velocity given as $A_2 = a_0 \sin(k_1(X_1 - U_\infty t))$. The velocity will be of the form $u_i^{(2)} = (u_1^{(2)}, u_2^{(2)})$. Applying the direct solution from Majumdar and Peake (1998) which is given by

$$4.2.5$$

$$u_i = \tilde{A}_j(k) \frac{\partial X_j}{\partial x_m} \left(\delta_{im} - \frac{\kappa_i \kappa_m}{|\vec{\kappa}|^2} \right) \sin(k(X - \hat{i}U_\infty t)$$

where we are interested in the index $j=2$, we obtain

$$4.2.6$$

$$u_i = a_0 \frac{\partial X_2}{\partial x_m} \left(\delta_{im} - \frac{\kappa_i \kappa_m}{|\vec{\kappa}|^2} \right) \sin(k_1(X - U_\infty t))$$

Since the local distorted wave number $\vec{\kappa}$ has the following components

$$4.2.7$$

$$\vec{\kappa} = (\kappa_1, \kappa_2) = \left(k_1 \frac{\partial X_1}{\partial x_1}, k_1 \frac{\partial X_1}{\partial x_2} \right) = (k_1 \cos\theta, -k_1 \sin\theta)$$

and we have the following solutions

$$4.2.8$$

$$u_1^{(2)} = a_0 \sin\theta \sin(k_1(X_1 - U_\infty t))$$

$$u_2^{(2)} = a_0 \cos\theta \sin(k_1(X_1 - U_\infty t))$$

The wavefronts for this gust in a solid body rotational flow are shown in Figure 4. Before distortion, the wavefronts are travelling in the x_1 direction as shown in Figure 4(a). As the wave enters a solid body rotation shown in Figure 4(b), the wavefronts rotate uniformly illustrating how the fluid particles keep rotation about their own centers while rotating as a "solid body" with the fluid as a whole.

The second case considers an upstream velocity as a two-dimensional gust travelling at an angle ϕ where

$$\tilde{A}_1 = a_0 \sin\phi \qquad\qquad k_1 = k_0 \cos\phi$$
$$\tilde{A}_2 = -a_0 \cos\phi \qquad\qquad k_2 = k_0 \sin\phi$$

The unsteady velocity will be of the form

4.2.10

$$u_i = u_i^{(1)} + u_i^{(2)}$$

where the superscript indicates the contribution from A_1 and A_2 respectively. Now if we substitute the distorted wave number terms where

4.2.11

$$\kappa_1 = k_1 \frac{\partial X_1}{\partial x_1} + k_2 \frac{\partial X_2}{\partial x_1} = k_1 \cos\theta + k_2 \sin\theta = k_0 \cos(\phi - \theta)$$

$$\kappa_2 = k_1 \frac{\partial X_1}{\partial x_2} + k_2 \frac{\partial X_2}{\partial x_2} = -k_1 \sin\theta + k_2 \cos\theta = k_0 \sin(\phi - \theta)$$

$$\text{and} \quad |\vec{\kappa}|^2 = k_0^2$$

For the superscript $j=1$ we have the following components

4.2.12

$$u_1^{(1)} = a_0 \sin^2\phi(\sin(\phi - \theta)\sin(k_1 X_1 + k_2 X_2)$$

$$u_2^{(1)} = -a_0 \sin^2\phi\cos(\phi - \theta)\sin(k_1 X_1 + k_2 X_2)$$

and similarly for superscript $j=2$ we have

4.2.13

$$u_1^{(2)} = a_0 \cos^2\phi(\sin(\phi - \theta)\sin(k_1 X_1 + k_2 X_2)\hat{x}_1$$

$$u_2^{(2)} = -a_0 \cos^2\phi\cos(\phi - \theta)\sin(k_1 X_1 + k_2 X_2)\hat{x}_2$$

This gives the total unsteady velocity as

4.2.14

$$u_i = a_0(\sin(\phi - \theta), -\cos(\phi - \theta))\sin(k_1 X_1 + k_2 X_2)$$

Figure 5(a) shows a two-dimensional gust before any influence of the flow and Figure 5(b) shows gust as it enters solid body rotation. It is observed that the deformation of the wavefronts is unchanged as before, just rotated relative to the origin of the flow.

It is also interesting to consider the vector representation of the solution, given as

4.2.15

$$\frac{|\mathbf{\kappa}||\mathbf{u}^{(g)}|\cos\theta_g}{a_0 k_0} = (\nabla X_1 . \nabla X_2)(\sin^2\phi - \cos^2\phi) + (|\nabla X_1|^2 - |\nabla X_2|^2)\sin\phi\cos\phi$$

In order to determine the unsteady velocity, we need to determine θ_g. The drift coordinate gradients for a solid body rotation flow are

4.2.16

$$\nabla X_1 = (\cos\theta, -\sin\theta) \qquad\qquad \nabla X_2 = (\sin\theta, \cos\theta)$$

therefore, $(\nabla X_1 . \nabla X_2) = 0$ and since $\left|\nabla X_1\right|^2 = \left|\nabla X_2\right|^2 = 1$ we have that

4.2.17

$$\left|\boldsymbol{\kappa}\right|\left|\mathrm{u}^{(g)}\right|\cos\theta_g = 0$$

assuming a gust of initial unit amplitude and unit wavenumber $a_o = k_o = 1$. Equation 4.2.17 equates to zero because $\left|\partial X_1/\partial x_i\right| = \left|\partial X_2/\partial x_i\right|$ for all angles ϕ. Therefore, $\cos\theta_g$ is zero for all values of ϕ because for solid body rotation the X_1 surface remains orthogonal to the X_2 surface, similar to the pure strain example. Therefore from equation 3.6.4, we see that $\left|\mathbf{u}\right| = \left|\mathbf{u}^{(g)}\right|$ which verifies there is no deformation of the gust for a solid body rotation flow as shown in Figure 4. This implies that there is no need for a potential flow correction and the unsteady flow velocity is described by the unsteady gust distortion $\mathbf{u}^{(g)}$.

4.3 Potential Vortex Application

The potential vortex is another simple flow which can be used to verify RDT. In a potential vortex, vorticity is not present in the mean flow and so Goldstein's original assumptions are met. In this case each fluid particle follows a circular path but does not rotate about its own axis as shown in Figure 6. The flow in a potential vortex is irrotational everywhere except at the origin where the vorticity is theoretically infinite.

The mean flow for a potential vortex is $U = \Gamma/2\pi R$ where R is the radius of the streamline. If we let $R = R_o$ (constant), we can choose the reference velocity as $U_\infty = \Gamma/2\pi R_o$. Therefore, it follows that the drift coordinates X_1 and X_2 can be determined where

4.3.1

$$X_1 = \int_0^s \frac{U_\infty}{U}\,ds = \frac{U_\infty}{U}\int_0^\theta R\,d\theta = \frac{R^2\theta}{R_o}$$
$$X_2 = R$$

The corresponding drift coordinate gradients are then found to be

4.3.2

$$\nabla X_1 = \frac{1}{R}\frac{\partial X_1}{\partial\theta}\hat{e}_\theta + \frac{\partial X_1}{\partial R}\hat{e}_r = \frac{R}{R_o}\left(\hat{e}_\theta + 2\theta\hat{e}_r\right)$$
$$\nabla X_2 = \frac{1}{R}\frac{\partial X_2}{\partial\theta}\hat{e}_\theta + \frac{\partial X_2}{\partial R}\hat{e}_r = \hat{e}_r$$

In Cartesian coordinates, the drift gradients are given as

$$\nabla X_1 = \left(\frac{\partial X_1}{\partial x_1}, \frac{\partial X_1}{\partial x_2} \right) = \left\{ (\cos\theta + 2\theta\sin\theta), (-\sin\theta + 2\theta\cos\theta) \right\}$$

$$\nabla X_2 = \left(\frac{\partial X_2}{\partial x_1}, \frac{\partial X_2}{\partial x_2} \right) = (\sin\theta, \cos\theta)$$

Similar to the previous flow applications, we will consider two cases where we can study the unsteady velocity. The first case considers a one-dimensional wave with an upstream velocity $A_2 = a_0 \sin(k_1(X_1 - U_\infty t))$. The velocity will be of the form $u_i^{(2)} = (u_1^{(2)}, u_2^{(2)})$. Substituting in the drift gradients and applying the 1D upstream gust to the unsteady velocity solution from Majumdar and Peake (1998) given by equation 3.6.1 and determining the local distorted wave number $\bar{\kappa}$

4.3.4

$$\bar{\kappa} = (\kappa_1, \kappa_2) = \left(k_1 \frac{\partial X_1}{\partial x_1}, k_1 \frac{\partial X_1}{\partial x_2} \right) = \left\{ k_1(\cos\theta + 2\theta\sin\theta), k_1(-\sin\theta + 2\theta\cos\theta) \right\}$$

we then have the following solutions

4.3.5

$$u_1^{(2)} = |u_1^{(2)}| \sin\theta \sin(k_1(X_1 - U_\infty t))$$

$$u_2^{(2)} = |u_2^{(2)}| \cos\theta \sin(k_1(X_1 - U_\infty t))$$

where

4.3.6

$$|u_1^{(2)}| = a_0 \left\{ \sin\theta \left[1 - \frac{(\cos\theta + 2\theta\sin\theta)^2}{4\theta^2 + 1} \right] + \cos\theta \left[\frac{(\cos\theta + 2\theta\sin\theta)(\sin\theta - 2\theta\cos\theta)}{4\theta^2 + 1} \right] \right\}$$

$$|u_2^{(2)}| = a_0 \left\{ \sin\theta \left[\frac{(\sin\theta - 2\theta\sin\theta)(\cos\theta + 2\theta\sin\theta)}{4\theta^2 + 1} \right] + \cos\theta \left[1 - \frac{(-\sin\theta + 2\theta\cos\theta)^2}{4\theta^2 + 1} \right] \right\}$$

The amplitudes $|u_1^{(2)}|$ and $|u_2^{(2)}|$ are derived in the Appendix A. Figure 7 is a plot comparing the amplitudes of both velocity components of a potential vortex for angles θ ranging from 0 to $\pi/2$. Both amplitudes consist of a $\cos\theta$ and $\sin\theta$ term, where $|u_1^{(2)}| = 0$ and $|u_2^{(2)}| = 1$ at $\theta = 0$. The left plot shows the change of amplitude as the flow rotates for a low frequency gust. As θ increases, $|u_1^{(2)}|$ increases and $|u_2^{(2)}|$ decreases and the two intersect at some θ between $\pi/3$ and $\pi/2$. If these velocity magnitudes are observed for a higher frequency, as shown in the right plot in Figure 7, we see how the magnitude of both components decrease where $|u_1^{(2)}|$ decreases more drastically than $|u_2^{(2)}|$ and there is no intersection. In Figure 8, we see how a 1D gust traveling in the x_1 direction in a potential vortex behaves by observing the change in wavefronts. It parallels the same distortion and stretching shown in the amplitude plots. Figure 8(a) is a plot of the 1D gust before any influence of the flow. The wavefronts are uniform and traveling in the x_1

direction. Figure 8(b) shows the upstream gust in a potential vortex with constant amplitude. The flow is observed to be moving faster closer to the center of the flow and slower further outwards. The same is shown in the unsteady gust $\mathbf{u}^{(g)}$ plot in Figure 8(c) with a slight change in amplitude. The faster flow toward the center and slower flow on the outside for the vortex creates a tornado effect where we observe swirling distortion. This directly shows how the fluid is irrotational everywhere except for the origin where vorticity is theoretically infinite. Lastly, we see in Figure 8(d) the wavefronts of the unsteady velocity. The same distortion occurs here with an addition of a decrease in amplitude magnitude implying the stretching of the initial gust.

Now let us consider the second case where we define a 2D gust characterized by

$$4.3.7$$

$$\tilde{A}_1 = a_o \cos\phi \qquad k_1 = k_o \sin\phi$$
$$\tilde{A}_2 = a_o \sin\phi \qquad k_2 = -k_o \cos\phi$$

It then follows for a potential vortex that the local gust amplitudes are

$$4.3.8$$

$$u_1^{(g)} = a_o\left(\frac{\partial X_1}{\partial x_1}\cos\phi + \frac{\partial X_2}{\partial x_1}\sin\phi\right) = a_o\left(\cos\theta\cos\phi + 2\theta\sin\theta\cos\phi + \sin\theta\sin\phi\right)$$

$$u_2^{(g)} = a_o\left(\frac{\partial X_1}{\partial x_2}\cos\phi + \frac{\partial X_2}{\partial x_2}\sin\phi\right) = a_o\left(-\sin\theta\cos\phi + 2\theta\cos\theta\cos\phi + \cos\theta\sin\phi\right)$$

and the distorted wavenumbers are given as

$$4.3.9$$

$$\kappa_1 = k_o\left(\frac{\partial X_1}{\partial x_1}\sin\phi - \frac{\partial X_2}{\partial x_1}\cos\phi\right) = k_o\left(\cos\theta\sin\phi + 2\theta\sin\theta\sin\phi - \sin\theta\cos\phi\right)$$

$$\kappa_2 = k_o\left(\frac{\partial X_1}{\partial x_2}\sin\phi - \frac{\partial X_2}{\partial x_2}\cos\phi\right) = k_o\left(-\sin\theta\sin\phi + 2\theta\cos\theta\sin\phi - \cos\theta\cos\phi\right)$$

In order to obtain θ_g to determine the potential flow correction, we substitute the drift coordinate gradients into equation 3.6.8 which yields

$$4.3.10$$

$$\cos\theta_g = \frac{a_o k_o\left(2\theta(\sin^2\phi - \cos^2\phi) + 4\theta^2\sin\phi\cos\phi\right)}{|\kappa||\mathbf{u}^{(g)}|}$$

where $|\kappa||\mathbf{u}^{(g)}|$ can be determined by the following

$$4.3.11$$

$$|\kappa| = \sqrt{\kappa_1^2 + \kappa_2^2} = k_o\sqrt{(1+4\theta^2)\sin^2\phi - 4\theta\cos\phi\sin\phi + \cos^2\phi}$$

and

$$\left|\mathbf{u}^{(g)}\right| = \sqrt{\left(u_1^{(g)}\right)^2 + \left(u_2^{(g)}\right)^2} = a_o \sqrt{(1+4\theta^2)\cos^2\phi + 4\theta\cos\phi\sin\phi + \sin^2\phi}$$

Detailed derivations for $\left|\boldsymbol{\kappa}\right|$ and $\left|\mathbf{u}^{(g)}\right|$ can be found in the Appendix B. It is observed that the angle θ_g depends on θ, which is the azimuthal location of the circular flow path in the potential vortex. This is important to note because as the flow rotates and θ increases, the more distortion the fluid particles experience. Figure 9 shows the potential flow correction for a 2D potential vortex where $\sin\theta_g$ is plotted against θ for various values of ϕ assuming a gust of initial unit amplitude and unit wavenumber $a_o = k_o = 1$. It is observed that the angle θ_g depends on θ, which is the azimuthal location of the circular flow path in the potential vortex. This is important to note because as the flow rotates and θ increases, the more distortion the fluid particles experience unless the flow is a boundary layer type flow where the gusts have a small angle ϕ (i.e. $k_2 \gg k_1$). In this case the small ϕ application is of practical interest. If $\sin\theta_g$ equals 1 then $\left|\mathbf{u}\right| = \left|\mathbf{u}^{(g)}\right|$ from equation 3.6.4 and the unsteady velocity is described by the pure distortion caused by the unsteady gust and there is no need for a potential correction. If the gust is only traveling in one direction where $\phi = 0$ or $\pi/2$, $\sin\theta_g$ decreases gradually from 1 when $\theta = 0$ as the flow rotates showing that there is a need for a potential correction as θ increases. As the upstream gust travels in both directions at angles ϕ smaller than $\pi/4$, the potential flow correction $\sin\theta_g$ remains equal to 1 longer and then begins to decrease as the flow rotates. It is observed in this plot that when $\phi = \pi/10$, the unsteady gust describes the velocity ($\sin\theta_g \approx 1$) for approximately the entire 90° flow rotation before a potential correction is needed. This example implies that the potential correction is small for these boundary layer types of flow where ϕ is small.

Figure 10(a) is a plot of the 2D gust traveling at an angle of 45° before any influence of the flow, hence the uniform wavefronts. Figure 10(b) shows the upstream gust in a potential vortex with constant amplitude. The flow is observed to be moving faster closer to the center of the flow and slower further outwards. The same is shown in the unsteady gust $\mathbf{u}^{(g)}$ plot in Figure 10(c) with an increase in amplitude as the flow rotates clockwise. We observe the same swirling distortion as in the 1D case. In Figure 10(d) the wavefronts of the unsteady velocity show the same distortion with an addition of a decrease in amplitude magnitude implying the stretching of the initial gust.

The vector representation can be generalized for potential flows as discussed in Section 3.6.1 and this can be used to verify the results given above. If we take the following relationship

$$\left|\boldsymbol{\kappa}\right|\left|u^{(g)}\right|\cos\theta_g = \frac{Uf(X)}{U_\infty}(\sin^2\phi - \cos^2\phi) + \left(\left(\frac{U_\infty}{U}\right)^2 + f^2 - \left(\frac{U}{U_\infty}\right)^2\right)\sin\phi\cos\phi$$

and using the definitions given above $f(X) = 2\theta$ and it follows that

$$\left|\boldsymbol{\kappa}\right|\left|u^{(g)}\right|\cos\theta_g = 2\theta(\sin^2\phi - \cos^2\phi) + 4\theta^2\sin\phi\cos\phi$$

which yields the same result found in equation 4.3.10 assuming a gust with initial unit amplitude and unit wavenumber $a_o = k_o = 1$.

4.4 Flow over a Step

The final flow considered to verify the high frequency approximation to RDT is the flow over a step. We will first consider the potential flow over a forward-facing step as shown in Figure 11. This simple flow example will be examined to determine the unsteady velocity using the Majumdar and Peake (1998) vector representation method as well as solving the direct solution. We will then compare the potential flow results to results determined numerically for a shear flow over a forward-facing step obtained from Reynolds Averaged Navier Stokes (RANS) calculations. This application will show how RDT can be applied to flows simulated using numerical methods based on the RANS equations, which has not been studied in the past.

4.4.1 Potential Flow

Let's consider the potential flow over a forward-facing step as shown in Figure 11. Using the vector representation, the function f needs to be determined in order to solve for the unsteady velocity. For a 2D potential flow, the drift coordinate gradients are given as

$$\nabla X_1 = \frac{U_\infty}{U} \hat{\mathbf{s}} + f(\mathbf{X})\hat{\mathbf{n}} \qquad \nabla X_2 = \frac{U}{U_\infty} \hat{\mathbf{n}}$$
4.4.1

where $\mathbf{s}$ and $\mathbf{n}$ are vectors in the direction of the mean flow and normal to the mean flow. For this case we have the following relationship

$$|\boldsymbol{\kappa}||\mathbf{u}^{(g)}|\cos\theta_g = \frac{Uf(\mathbf{X})}{U_\infty}(\sin^2\phi - \cos^2\phi) + \left(\left(\frac{U_\infty}{U}\right)^2 + f^2 - \left(\frac{U}{U_\infty}\right)^2\right)\sin\phi\cos\phi$$
4.4.2

where $a_o = k_o = 1$ if a gust with initial unit amplitude and unit wavenumber is considered. The drift coordinates can be calculated as

$$X_1 = \int_0^s \frac{U_\infty}{U} \, ds = \int_0^\Phi \frac{U_\infty}{U^2} d\Phi$$
4.4.3

$$X_2 = \frac{\Psi}{U_\infty}$$

where Φ and Ψ are the potential and stream functions for the mean flow, respectively. Hence we have

$$f = \int \frac{\partial}{\partial \Psi}\left(\frac{U_\infty^2}{U^2}\right) d\Phi$$
4.4.4

We note the following relationship for a flow over a step (Bryan (2013))

$$U^2 = \left| \frac{\Phi + 1 + i\Psi}{\Phi - 1 + i\Psi} \right| = \sqrt{\frac{(\Phi+1)^2 + \Psi^2}{(\Phi-1)^2 + \Psi^2}}$$

which will allow us to analytically obtain f for $\Psi > 0$ and the drift coordinate X_1.

First we will look at the behavior of a far upstream gust $\tilde{A}_k(\mathbf{k})e^{i\mathbf{k}.(X-iU_\infty t)}$ as it convects over the step. Figure 12(a) shows the distortion of a gust with wavefronts at an angle of 45° and the stretching of the wavefronts as the flow is convected over the step. The amplitude remains constant and as the flow convects downstream, and it is observed that the fluid nearest to the top of the step is slower, contributing more to the stretching behavior. Wavefronts of the unsteady gust $\mathbf{u}^{(g)}$ is shown in Figure 12(b). It is observed there is a change in amplitude magnitude as the gust travels over the step. The wavefronts closest to both the face and the top of the step have an increase in amplitude and show the most distortion. Figure 12(c) shows the wavefronts of the unsteady velocity. Figure 13 shows the comparison of the unsteady velocity wavefronts using (a) vector representation and (b) the direct solution, respectively. It is observed the two plots are identical as expected. The gust is distorted over the step as it is convected where the amplitude decreases and the wavefronts are stretched along the top of the step.

4.4.2 Shear Flow

In this section we will study the distortion of a gust in a boundary layer (shear) flow. Velocity data from an ANSYS-FLUENT model based on solutions to the RANS equations of a boundary layer flow over a forward-facing step (provided by B. Bryan (2013)) was used for the results presented in this section. These calculations not only show consistency with the previous flow applications but they also demonstrate how RDT can be applied to flows simulated using numerical solutions to the RANS equations, which has not been studied in the past.

The streamlines of the shear flow are shown in Figure 14 modeled from the interpolated velocity data from the RANS model. Modeling was done with distances and velocities normalized relative to the step height and inlet speed U_∞, respectively. Figure 15(a) shows the distortion of a far upstream gust $\tilde{A}_k(\mathbf{k})e^{i\mathbf{k}.(X-iU_\infty t)}$ traveling at an angle of 45°. Although the amplitude of the wavefronts remains constant, it is observed that the wavefronts stretch as the flow is convected over the step. As the flow convects downstream, the fluid nearest to the top of the step appears to be slower contributing to the stretching behavior. The unsteady gust and unsteady velocity results were obtained numerically using the vector representation method. Wavefronts of the unsteady gust $\mathbf{u}^{(g)}$ are shown in Figure 15(b). It is observed there is a significant change in amplitude magnitude as the gust travels over the step. The wavefronts closest to the face and top of the step increase in amplitude and show the most distortion. This plot shows the pure distortion in this shear flow. Figure 15(c) shows the wavefronts of the Majumdar and Peake approximation to the unsteady velocity. The amplitude decreases due to the wavefronts stretching as they are convected downstream over the step. It is also observed that there are less wavefronts as the flow convects downstream which contributes to the lengthening of the wavefronts due to the stretching behavior. These results from the RANS flow show consistent agreement with the potential mean flow model. Hence, in the following chapter we will look at more complicated flows such as rotor inflows modeled by RANS, and compare

results to the mean potential flow. This will further show the possibilities of applying RDT to shear flows modeled by CFD programs.

5: Applications To Rotor Inflows

In this section some examples of distorted inflows into a rotor will be discussed. We will consider a non-axisymetric flow for a rotor near a wall as shown in Figure 16, and as studied experimentally by Alexander *et al.* (2013) and Morton *et al.* (2012). Results for the axisymmetric case of a rotor in free space without a wall will also be given for comparison. Two different estimates of the mean flow into the rotor will be used. First the mean flow through the rotor for a loaded rotor will be modeled by applying Conway's (1995) actuator disc theory. In the second, the boundary layer flow, which is defined by a rotational flow with a mean shear, through the same configuration will be modeled by solutions to the Reynolds Averaged Navier Stokes (RANS) equations. To estimate the flow distortion, vortex filaments will be tracked downstream from points of order six radii upstream of the rotor disc to the rotor disc plane. Two cases were studied for each flow with varying inlet speeds U_∞ and constant rotor speed $\Omega = 2734$ [rpm]. For case 1, $U_\infty = 15$ [m/s] giving an advance ratio of $J = 0.72$. For case 2, $U_\infty = 10$ [m/s] and $J = 0.48$. (The RANS calculations were provided by A. Buono (2013) and F. Lachowski (2013) and are described in the next section)

These inflow conditions are equivalent to those studied experimentally by Alexander *et al.* (2013). All modeling was done with distances and velocities normalized relative to the rotor radius and inlet speed U_∞, respectively. The rotor disc was placed at a distance equivalent to 8.9% of its radius from the wall. Figure 16 shows the configuration of the rotor and wall in which both flows were modeled.

5.1 Potential Flow

The first flow to be considered is the potential mean flow that is both irrotational and incompressible. To model this flow, Conway's (1995) actuator disc theory was used where the time-averaged velocity field induced by the rotor is given by an actuator disc model. The mean flow is represented by an array of material lines that correspond to radial and circular lines on a disc six rotor radii upstream of the rotor plane. Figure 17 displays a ring of the material lines before and after propagation towards the rotor for case 2 both with and without a wall present. Both cases show similar behavior; however, results with the wall are more significant. Results for the models without the wall show that the distortion of the ring is axisymmetrical, and the ring is slightly compacted circumferentially. Results with the wall present show that the ring experiences non-axisymmetrical distortion and there is vertical stretching at the bottom where the ring is in contact with the wall. In Figure 18 the 2-D projection of the disc distortion for case 2 is shown as a view from the rotor axis after propagation at the final upstream position both without and with the wall. Again, both examples have similar behavior but the example with wall displays more dramatic results. It is seen that the distorted flow disc is axisymmetric without the wall and non-axisymmetric with the wall, including stretching at the bottom of the disc near the wall due to distortion of the flow. Figure 19 shows the potential inflow disc distortion with a contour surface relative to normalized streamwise velocity for both flow speeds with the wall present. These plots clearly display the magnitude of the distortion of material lines relative to the streamwise velocity. It is observed that near the wall the material lines have a

decreased streamwise velocity relative to the rest of the disc. Just above that and below the hub, the streamwise velocity is the greatest, before the flow is ingested into the rotor. Case 2, which is the lower advance ratio case, is observed to have more significant distortion.

5.2 Shear Flow

The second flow we will consider is the shear flow, which is characterized by a boundary layer. This flow was modeled in ANSYS–FLUENT based on solutions to the RANS equations using two different methods, where the first utilized a Multiple Reference Frame (MRF) fluid model (Lachowski (2013)) and the second utilized an actuator disc model.

5.2.1 The MRF model

Results presented in this section were determined using numerical data gathered by Lachowski (2013) using a MRF fluid model. Multiple reference frames are used to model flows with relative motion involving moving parts of the computational domain. However, the addition of reference frames increases the complexity of the problem and the interface between the moving frame and the fixed frame is a major limitation. The MRF model evaluates the flow in the vicinity of the rotor in the moving frame of reference, and the upstream flow in the fixed frame of reference. The flow at the interface is assumed to be homogeneous, which is not the case for a rotor near a wall as discussed here. Not withstanding this issue we will present results using this model before considering an inhomogeneous model based on a viscous flow with an actuator disc representing the rotor.

A ring of material lines before and after convection is shown in Figure 20 for each flow speed obtained from the MRF model. The ring experiences non-axisymmetrical distortion in both cases with vertical stretching at the bottom where the ring is in contact with the wall. This is due to the shearing of the flow at the wall. In case 2 the distortion is slightly more circumferentially compacted than for case 1. Figure 21 displays a 2D projection of the shear flow disc distortion at the rotor axis for both cases after propagation at the final downstream position. In both cases the disc distortion is non-axisymmetric and has horizontal stretching at the bottom of the disc near the wall due to shearing of the flow. Figure 22 shows the inflow disc distortion with a contour surface colored according to normalized streamwise velocity for both cases. Significant shearing of the flow near the wall is observed compared to the potential flow (Figure 19). Again, the material lines are slower near the wall and faster just above the wall, below the hub. From these models, the effect of the boundary layer flow is to significantly increase the distortion of the material lines. The lines appear to elongate more in the streamwise direction, which will affect the haystacking observed in the radiated sound field by Alexander *et al.* (2013).

5.2.2. Viscous Actuator Disc Model

The second method based on solutions to the RANS equations utilized an actuator disc to model the rotor. The rotor is replaced by a pressure jump in the flow and upstream flow data can be computed. Data retrieved from simulations ran using this method (Buono (2013)) showed consistent distortion behavior to the MRF approach; however, the amplitude of distortion was greater. Figure 23 shows the inflow disc distortion with a contour surface colored according to normalized streamwise velocity for both cases. It is observed that there is the same significant

shearing of the flow near the wall; however, it the velocity is greater than the results presented using the MRF model.

5.3 Correlation Function

The rotor inflow results from this chapter imply that by knowing the drift and calculating the turbulence distortion, the upwash velocity correlation function at the face of a rotor given the upstream correlation function before distortion has taken place can be determined. This application contributes to rotor noise predictions which may include the haystacking phenomenon due the stretching of the turbulent gusts. The downstream correlation function is determined as

5.3.1

$$R_{ij}(\pmb{x},\pmb{x}') = \frac{\partial X_m(\pmb{x})}{\partial x_i} \frac{\partial X_n(\pmb{x}')}{\partial x_j} R_{mn}{}^{(\infty)}(\pmb{X},\pmb{X}')$$

where the correlation based on the drift is given by $R_{mn}{}^{(\infty)}(\pmb{X},\pmb{X}')$. This assumes that the distorted gust is given by the solution $\mathbf{u}^{(g)}$ without a correction for compressibility. From the analysis given in Section 3 a potential flow correction based on Majumdar and Peake's solution is required. However $\mathbf{u}^{(g)}$ is an approximate solution, and represents an upper limit if $\sin\theta_g$ is less than one. This implies that the correlation will be less than the estimate given by 5.3.1.

The calculations presented in this section are based on the evolution of the boundary layer turbulence over six rotor radii. However there is a fundamental question as to where in the flow the rapid distortion calculation should be started. For a shear flow for which the turbulence statistics do not change significantly as a function of downstream distance, the distortion must be self preserving. When an additional distortion is added (such as that caused by the flow acceleration by the rotor) then the self preserved turbulence will be distorted. In the calculations that will be shown in the last part of this report it will be argued that the starting point for the RDT calculation should be one integral lengthscale (measured in the moving frame of reference), or equivalently the Lagranian length scale, which will be estimated as one boundary layer thickness.

6: Conclusions

This part of the report has studied Rapid Distortion Theory (RDT) and its application to various simple flows and rotor inflows with and without shear. The RDT formulation was applied to various simple flows with known solutions including a solid-body rotation flow, a potential vortex flow, and a flow over a forward-facing step. A potential vortex and the solid body rotation were considered to show the differences in distortion as a gust was convected in a potential flow and a shear flow. The distortion caused to a turbulent boundary layer being ingested into a rotor was also evaluated and examples given that showed the extent of the distortion. The fundamental problem with this type of calculation however is identifying the location where the Rapid Distortion calculation should start. It was concluded that this should be one Lagranian lengthscale of the turbulence, which can be approximated in this case by the boundary layer thickness.

REFERENCES

Alexander, W. A., Devenport, W., Morton, M. A., and Glegg, S. A. L. 2013. Noise from a rotor ingesting a planar turbulent boundary layer. AIAA 19th Aeroacoustics Conference, Berlin, Germany.

Atassi, H.M. 1986. Aerodynamics of unsteady vortical flows. Fluid Dynamics Transactions, Polish Academy of Science, vol. 13, pp. 1-33, 1986.

Atassi, H. M. 1994. Unsteady aerodynamics of vortical flows: Early and Recent Developments. *Aerodynamics and Aeroacoustics*, Editor K. Y. Fung, Ch. IV, pp. 119-169, World Scientific.

Blake, W. *Mechanics of Flow Induced Sound and Vibration*, Wiley, New York, 1986.

Batchelor, G. K. and Proudman, I. 1954. The effect of rapid distortion of a fluid in turbulent motion. Q. J. Mech. Appl. Maths. vol.**7**, pp. 83-103.

Buono, A. 2013. RANS data for viscous actuator disc model. Personal communication.

Bryan, B. S. 2013. Noise radiation from small steps and cubic roughness elements immersed in turbulent boundary layer flow. Master's Thesis, OME Department, Florida Atlantic University.

Conway, J. T. 1995 Analytical solutions for the actuator disc with variable radial distribution of load. J. Fluid Mech. vol. 297, pp. 327-355.

Durbin, P. A., and B. A. Pettersson Reif. "Rapid distortion theory." *Statistical Theory and Modeling for Turbulent Flows*. 2nd ed. Wiley, 2001.

Goldstein, M. E. 1978. Unsteady vortical and entropic distortions of potential flows round arbitrary obstacles. J. Fluid Mech. vol. 89, pp. 433-468.

Golubev, V. V. and Atassi, H. M. 1998. Acoustic-vorticity waves in swirling flows. J. Sound & Vibr. vol.209, pp.203-222.

Hanson, D. B. 1974. The spectrum of rotor noise caused by atmospheric turbulence. J. Acoust. Soc. Am. vol. 56, pp. 110-126.

Hinze, J. O. "Isotropic turbulence." *Turbulence*. 2nd ed. New York: McGraw-Hill, 1975.

Hunt, J.C.R. 1973. A theory of turbulent flow round two-dimensional bluff bodies. J. Fluid Mech. vol.61, pp.625-706.

Hunt, J.C.R. and Carruthers, D.J. 1990. Rapid distortion theory and the 'problems' of turbulence. J. Fluid Mech. vol. 212, pp. 497-532.

Kundu, P. K. "Vorticity dynamics." *Fluid Mechanics*. 3rd ed. San Diego: Academic, 1990.

Lachowski, F. F. 2013. Aerodynamic analysis of a rotor in a turbulent boundary layer flow, Master's Thesis, OME Department, Florida Atlantic University.

Lighthill, M. J. 1956. Drift. J. Fluid Mech. vol.1, pp.31-53.

Majumdar, S. and Peake N. 1998. Noise generation by the interaction between ingested turbulence and a rotating fan. J. Fluid Mech. vol. 359, pp. 181-216.

Martinez, R. and Ting, C. 2006. Rapid distortion theory for a sheared background; Part I: Effects on the source of flow noise. ONR 26th Symposium on Naval Hydrodynamics, Rome, Italy.

Morton, M. A. 2012. Rotor inflow noise caused by a boundary layer: Inflow measurements and noise predictions, Master's Thesis, AOE Department, Virginia Tech, Avail: http://scholar.lib.vt.edu/theses/available/etd-08102012-103032/.

Morton M., Devenport W., Alexander W. N., Glegg S. A. L., and Borgoltz, A. 2012. Rotor inflow noise caused by a boundary layer: Inflow measurements and noise predictions, 18th AIAA/CEAS Aeroacoustics Conference, Colorado Springs, CO, Paper number AIAA-2012-2120.

Ribner, H.S. and Tucker, M. 1953. Spectrum of turbulence in a contracting stream. Tech. Rep. 1113. NACA.

Sears, W. R. 1941. Some aspects of non-stationary airfoil theory and its practical applications. J. Aero Sci. vol.83, pp.104-188.

Sevik, M. 1971. Sound radiation from a subsonic rotor subjected to turbulence. NASA SP 304.

Townsend, A. A. 1969. Entrainment and the structure of turbulent flow. J. Fluid Mech. vol.41, pp.13-46.
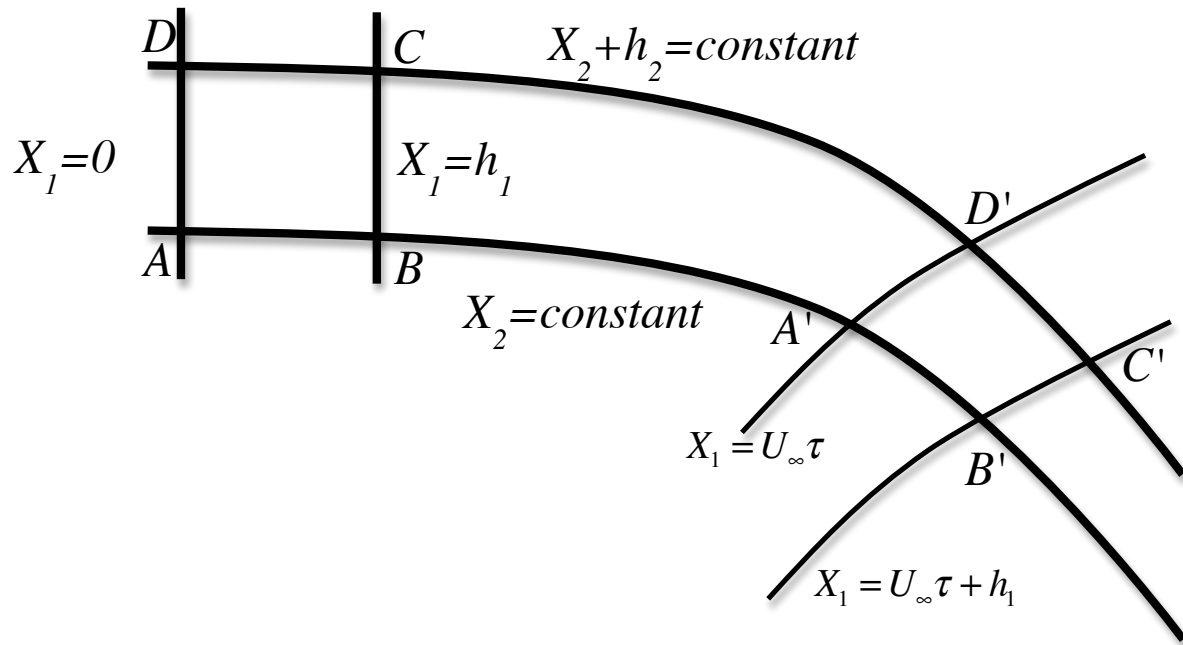
Figure 1: Drift Coordinates

In Figure 1, the following labels appear: D, C, $X_2+h_2=constant$, $X_1=0$, $X_1=h_1$, D', A, B, $X_2=constant$, A', C', $X_1=U_\infty\tau$, B', $X_1=U_\infty\tau+h_1$.
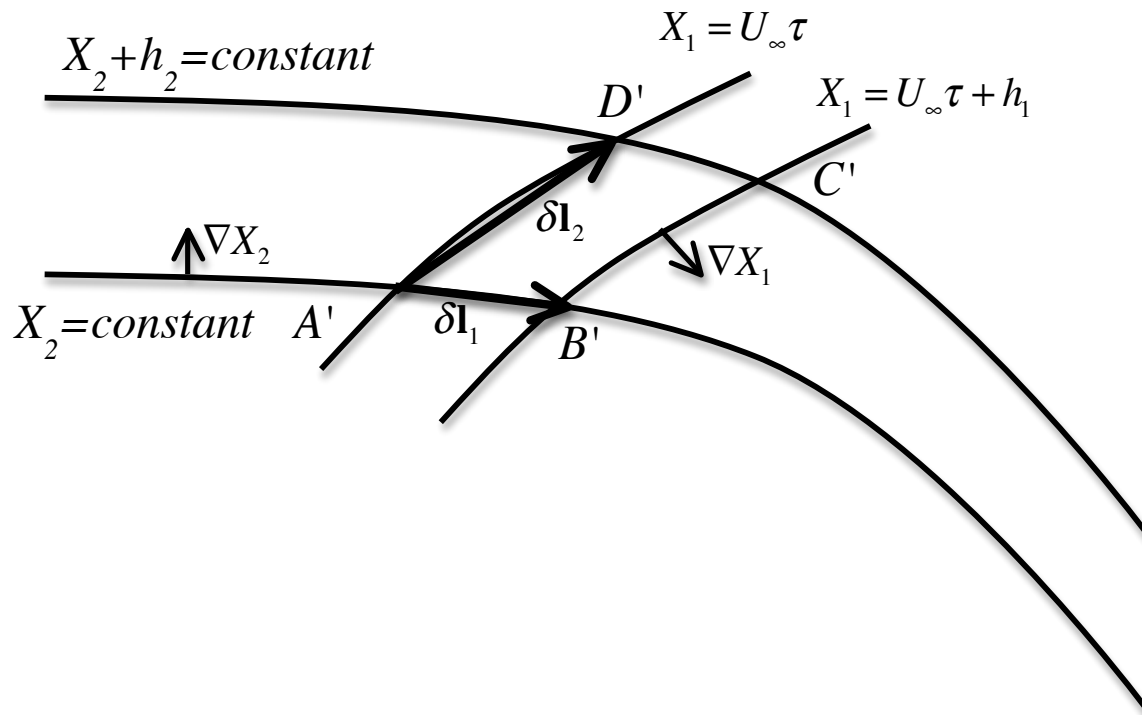
Figure 2: Details of the drift cell $A'B'C'D'$ shown in Figure 1.

In Figure 2, the following labels appear: $X_2+h_2=constant$, $X_1=U_\infty\tau$, D', $X_1=U_\infty\tau+h_1$, C', ∇X_2, $\delta\mathbf{l}_2$, ∇X_1, $X_2=constant$, A', $\delta\mathbf{l}_1$, B'.
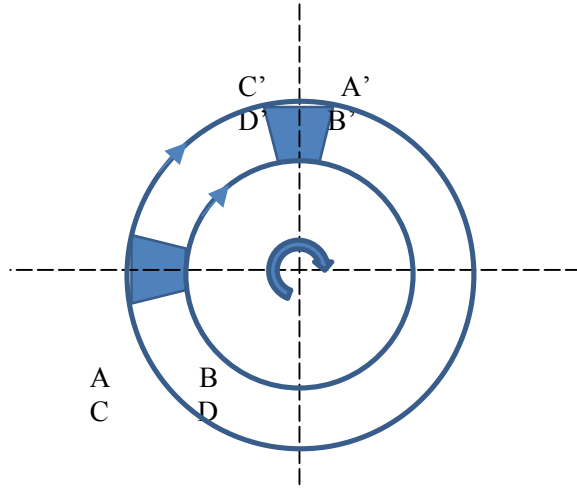
Figure 3: Solid-body rotation flow. The fluid elements spin about their own centers while revolving around the origin. There is no deformation of the drift cell elements.
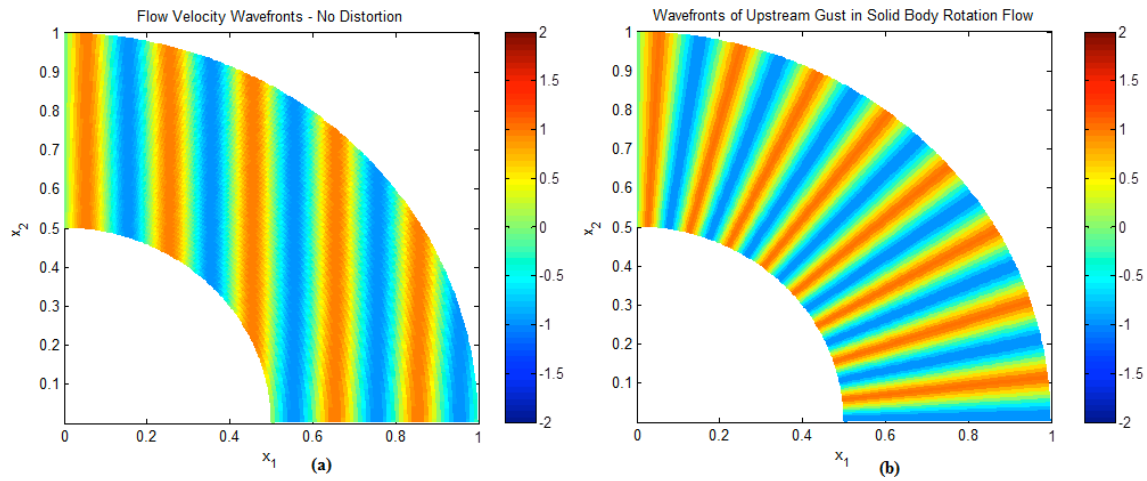
Figure 4: Solid body rotation 1D flow. The left plot (a) shows an upstream one-dimensional gust convected in the x_1 direction without any influence of the flow. The right plot (b) shows this 1D gust in solid-body rotation. The vorticity of each fluid particle is displayed by the constant unchanged wavefront distortion relative to the origin of the flow as it convects clockwise.
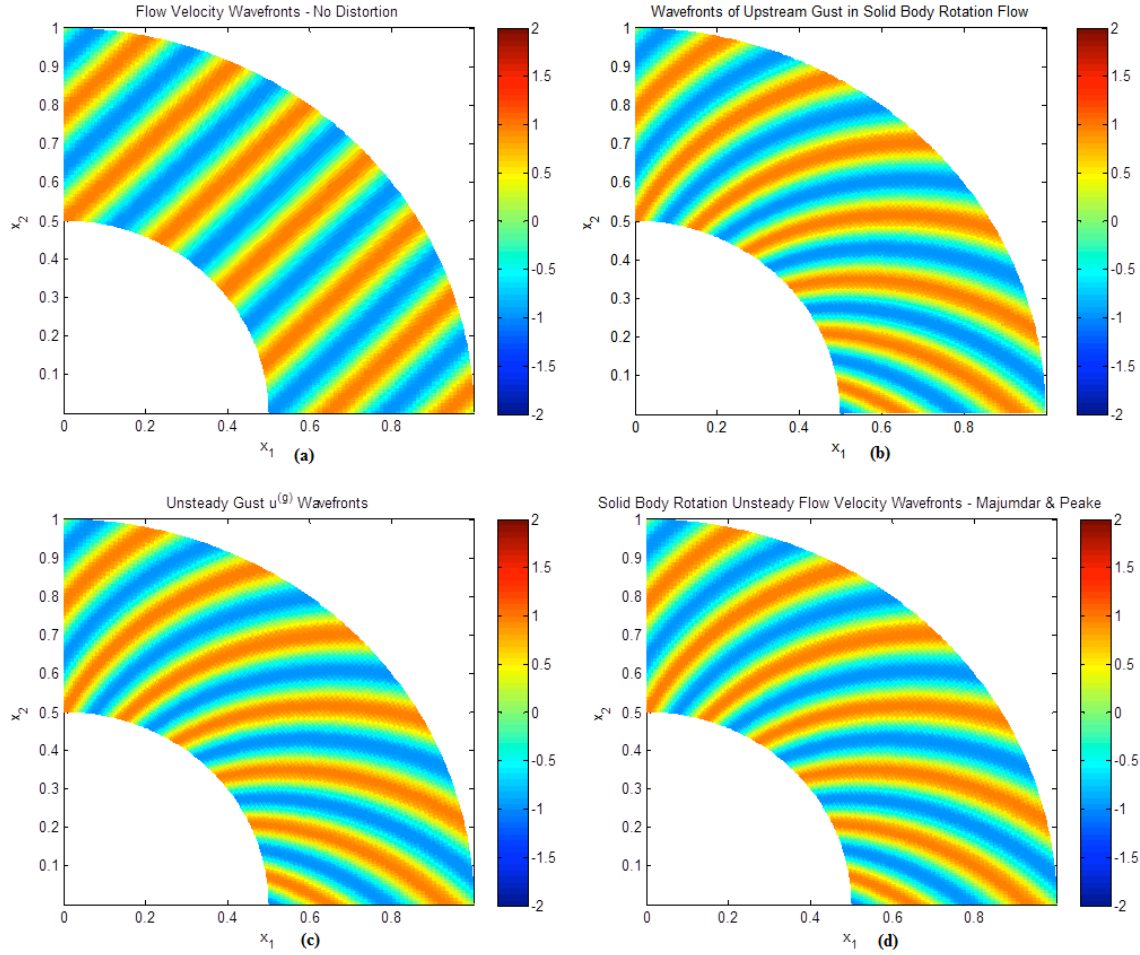
Figure 5: Solid body rotation 2D flow. Plot (a) shows an upstream two-dimensional gust convected at an angle of 45° in the x_1 and x_2 directions before influence of the flow. The upper right plot (b) shows this 2D flow in solid-body rotation. The vorticity of each fluid particle is displayed by the constant unchanged wavefront distortion relative to the origin of the flow as it convects clockwise. It is observed that the wavefronts closer to the center are traveling slower than those on the outer edge. The same exact behavior with no change in amplitude is observed in plots (c) and (d) which are the wavefronts of the unsteady gust $\mathbf{u}^{(g}$ and the total unsteady velocity of the gust, respectively. This is because there is no potential flow correction and $|\mathbf{u}^{(g)}| = |\mathbf{u}|$.
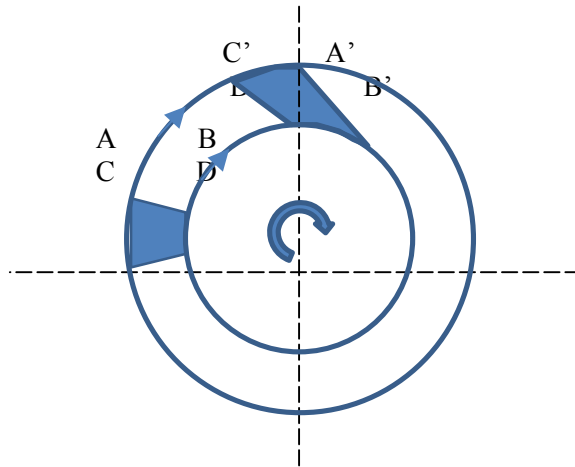
Figure 6: Potential vortex flow. This is an example of an irrotational vortex where vorticity of a fluid element is theoretically infinite at the origin and zero everywhere else.
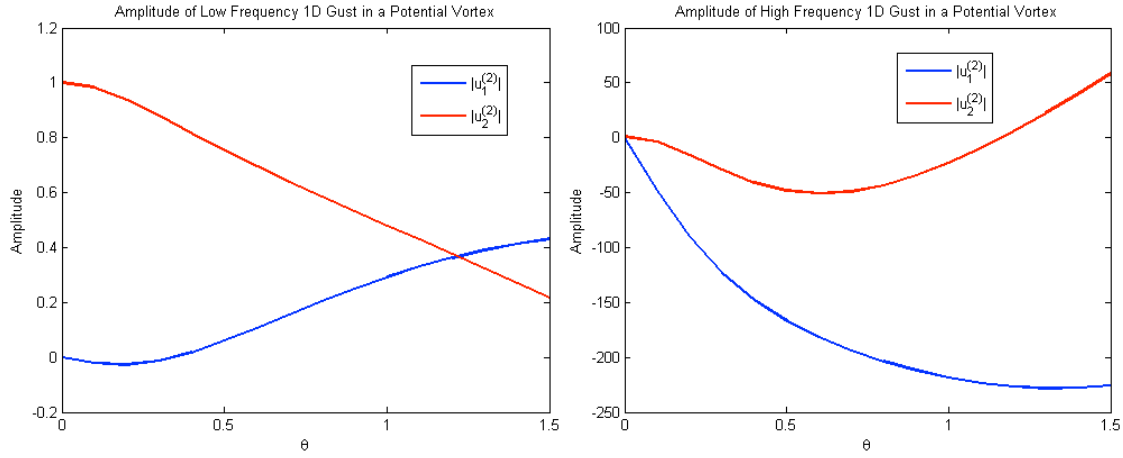
Figure 7: Amplitudes of both velocity components of a potential vortex for angles θ ranging from 0 to $\pi/2$. Both amplitudes consist of a *cosθ* and *sinθ* term, where $|u_1^{(2)}| = 0$ and $|u_2^{(2)}| = 1$ at $\theta = 0$. The left plot shows the change of amplitude as the flow rotates for a low frequency gust. As θ increases, $|u_1^{(2)}|$ increases and $|u_2^{(2)}|$ decreases and the two intersect at some θ between $\pi/3$ and $\pi/2$. If these velocity magnitudes are observed for a higher frequency, as shown in the plot to the right, we see how the magnitude of both components decrease where $|u_1^{(2)}|$ decreases more drastically than $|u_2^{(2)}|$ and there is no intersection.
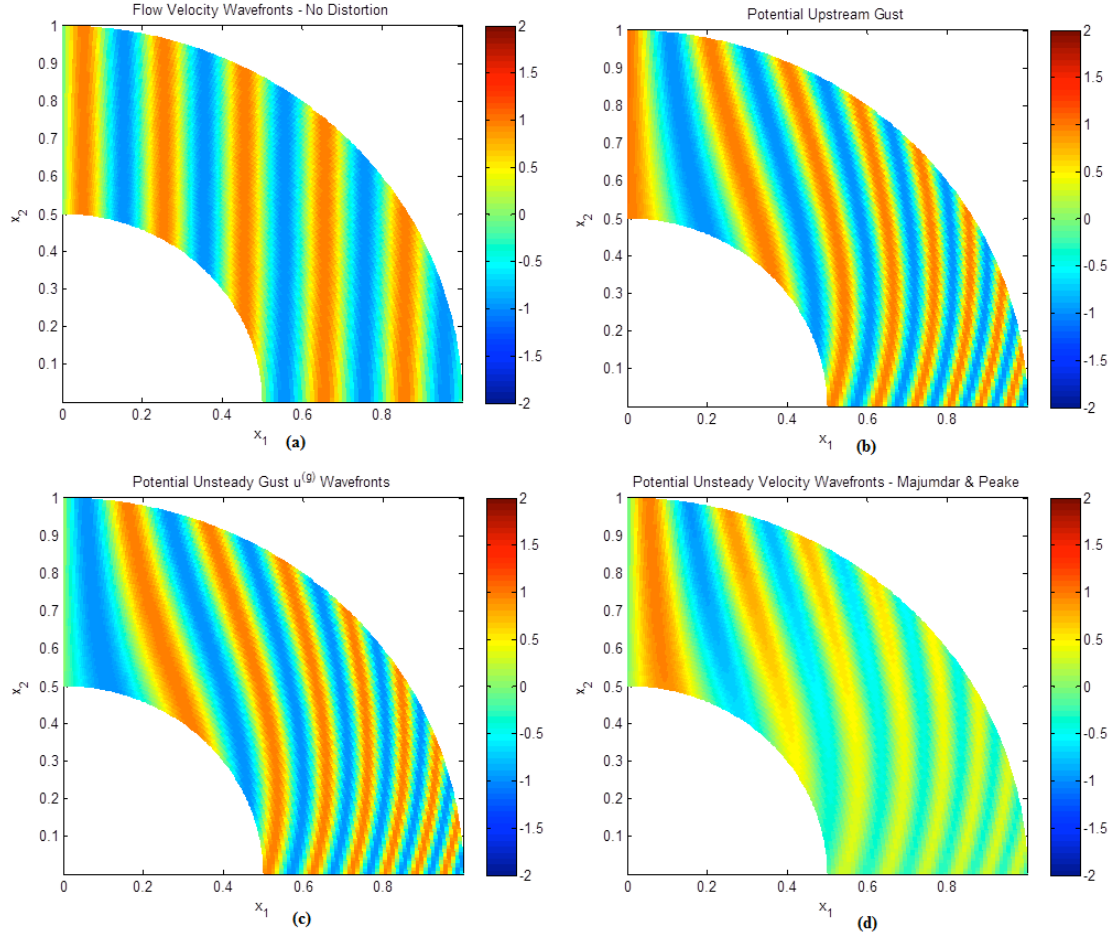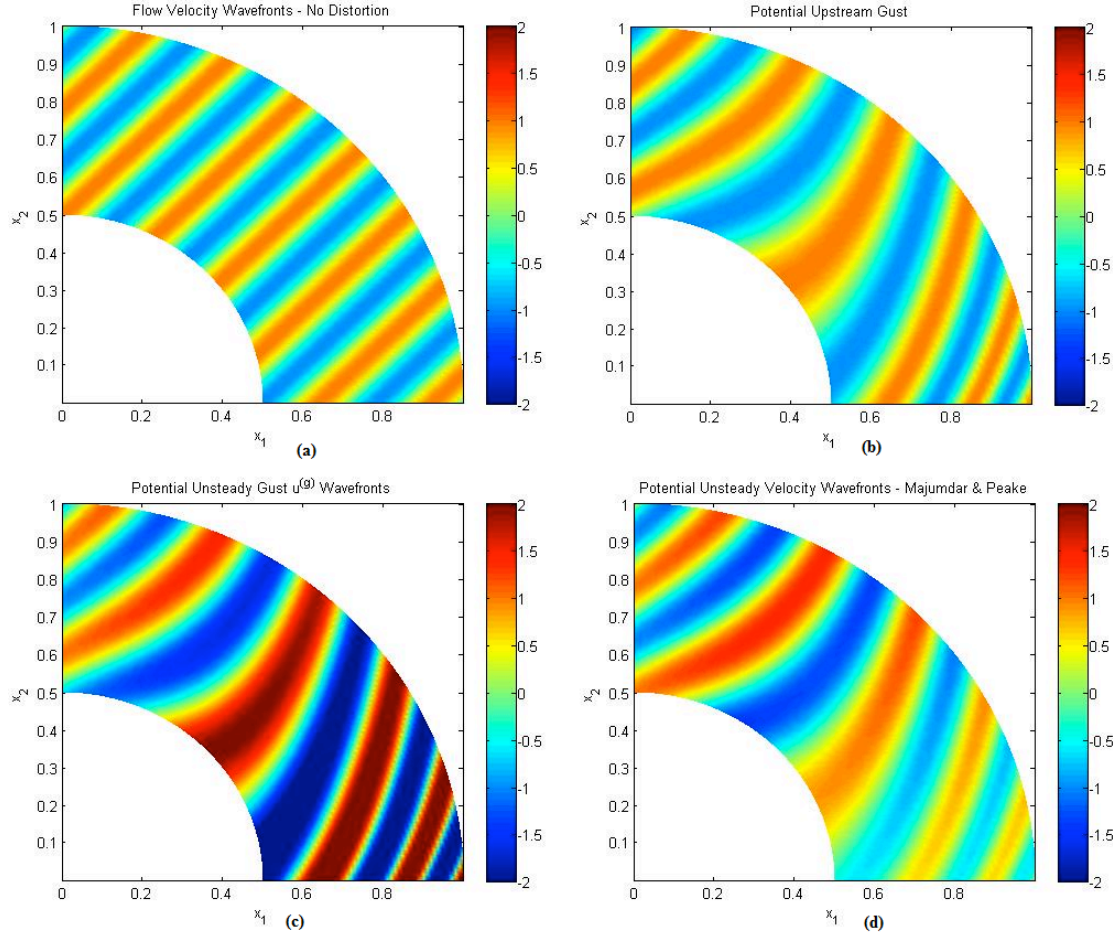
Figure 8: A one-directional gust in a potential vortex. Plot (a) displays the wavefronts of a 1D upstream gust without any influence of the flow. As the flow enters a potential vortex and rotates clockwise as shown in (b), it is observed the wavefronts are travelling faster toward the center of the flow and slower by the outer edge of the vortex. The fluid is stretched and a "tornado" effect is created since the individual particles are not rotating on their own axis. The amplitude remains constant. Plot (c) displays the wavefronts of an unsteady gust $\mathbf{u}^{(g}$ where there is a slight change in amplitude magnitude and an increase in wavelength as the gust is convected. The wavefronts of the unsteady velocity of the gust is displayed in (d) where the same behavior is observed with a decrease in amplitude due to stretching.
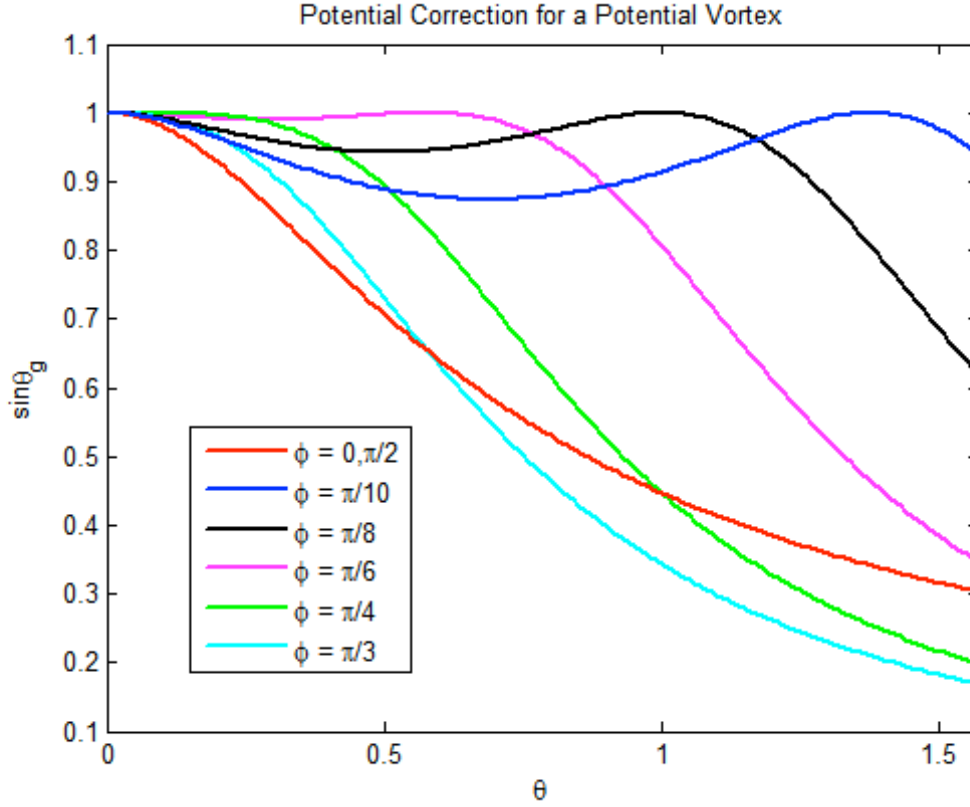
Figure 9: Potential flow correction for a 2D potential vortex where $\sin \theta_g$ is plotted against θ for various values of ϕ. It is observed that the angle θ_g depends on θ, which is the azimuthal location of the circular flow path in the potential vortex. This is important to note because as the flow rotates and θ increases, the more distortion the fluid particles experience unless the flow is a boundary layer type flow where the gusts have a small angle ϕ (i.e. $k_2 >> k_1$). If $\sin \theta_g$ equals 1 then $|\mathbf{u}| = |\mathbf{u}^{(g)}|$ from equation 3.6.4 and the unsteady velocity is described by the pure distortion caused by the unsteady gust and there is no need for a potential correction. If the gust is only traveling in one direction where $\phi = 0$ or $\pi/2$, $\sin \theta_g$ decreases gradually from 1 when $\theta = 0$ as the flow rotates showing that there is a need for a potential correction as θ increases. As the upstream gust travels in both directions at angles ϕ smaller than $\pi/4$, the potential flow correction $\sin \theta_g$ remains equal to 1 longer and then begins to decrease as the flow rotates. It is observed in this plot that when $\phi = \pi/10$, the unsteady gust describes the velocity ($\sin \theta_g \approx 1$) for approximately the entire 90° flow rotation before a potential correction is needed. This example implies that the potential correction is small for these types of flow.

Figure 10: A two-directional gust in a potential vortex. Plot (a) displays the wavefronts of a 2D upstream gust traveling at an angle of 45° without any influence of the flow. As the flow enters a potential vortex and rotates clockwise as shown in (b), it is observed the wavefronts are travelling faster toward the center of the flow and slower by the outer edge of the vortex. The fluid is stretched and a "tornado" effect is created since the individual particles are not rotating on their own axis. The amplitude remains constant. Plot (c) displays the wavefronts of an unsteady gust $\mathbf{u}^{(g)}$ where there is an increasing amplitude magnitude and an increase in wavelength as the gust is convected. This plot displays the pure distortion. The wavefronts of the unsteady velocity of the gust is displayed in (d) where the same behavior is observed with a decrease in amplitude due to stretching.
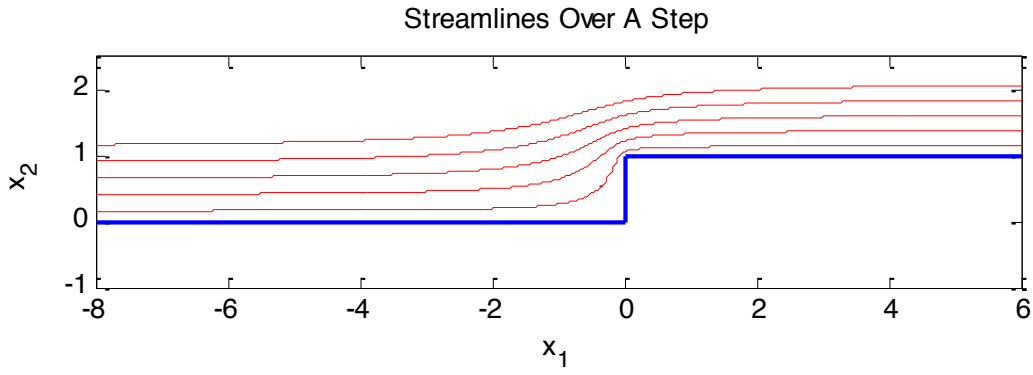
Figure 11: Streamlines over a forward-facing step. As the flow convects over the step, the fluid particles are distorted and stretched.
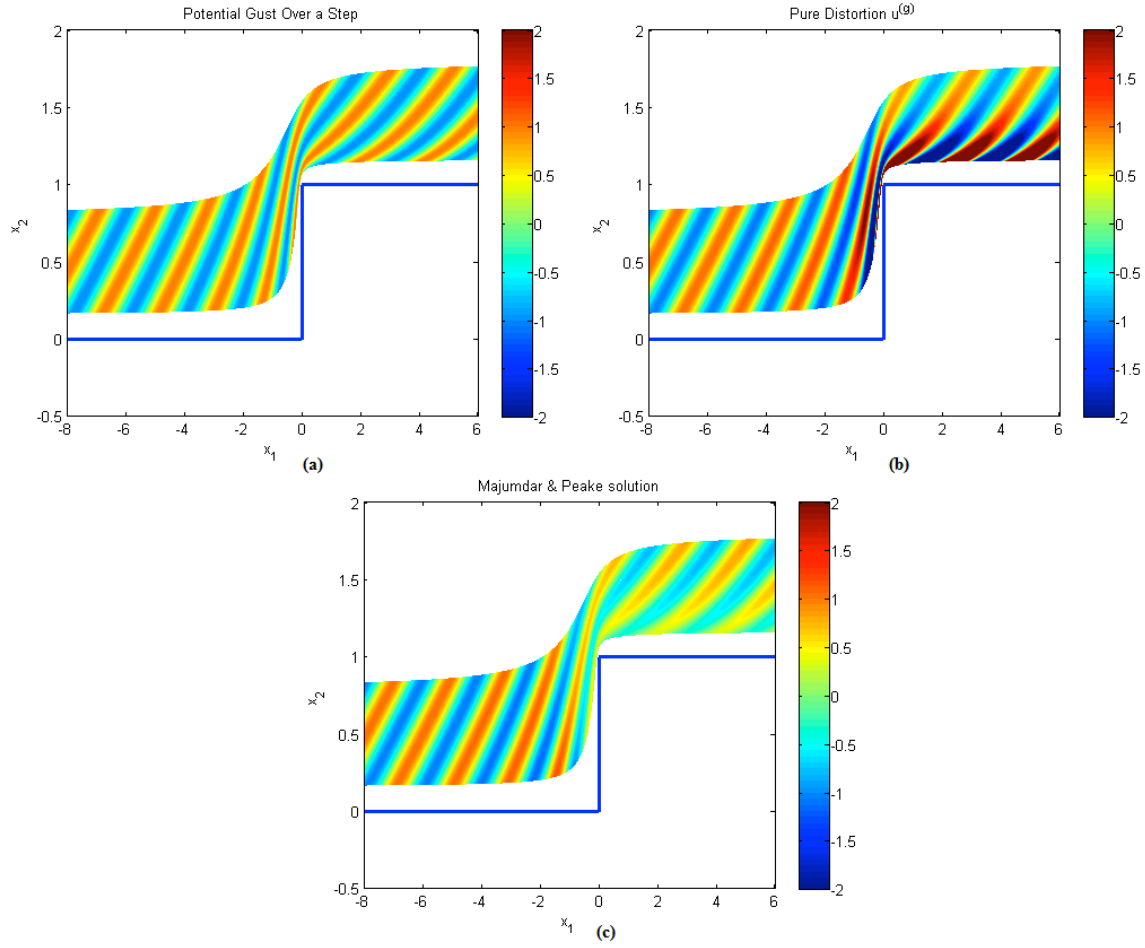
Figure 12: The top plot displays an upstream gust approaching a forward-facing step at an angle of 45°. There is distortion as the flow is convected over the step. The wavefronts are stretched; however, the amplitude remains constant. As the flow continues downstream the fluid nearest to the top of the step appears to be slower contributing to the stretching behavior. The bottom plot are the wavefronts of the unsteady gust $\mathbf{u}^{(g)}$. Compared to the top plot, it is observed there is a change in amplitude magnitude and an increase in wavelength as the gust is convected over the step.
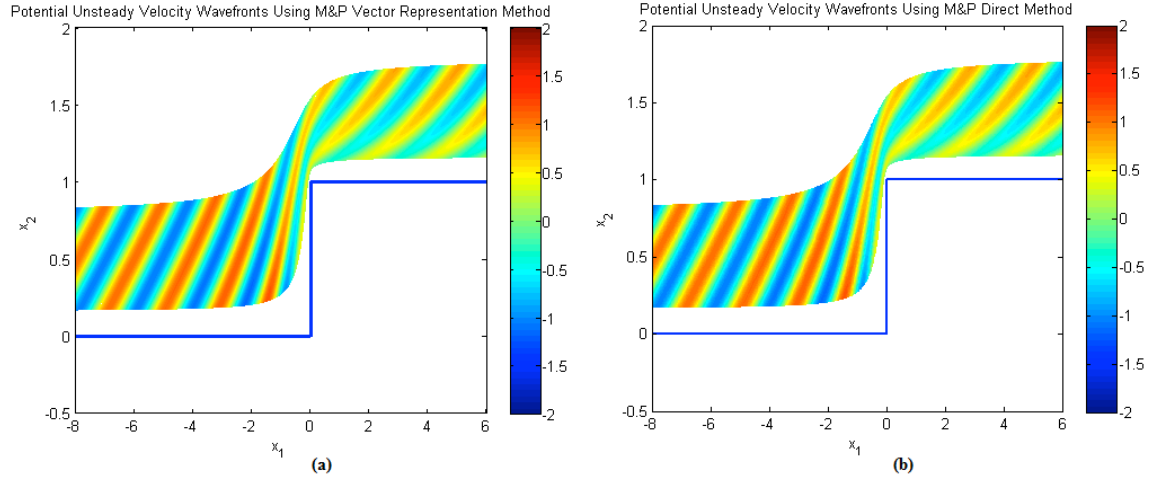
Figure 13: Potential flow over a forward-facing step. The left image (a) displays the wavefronts of the unsteady velocity determined using Majumdar and Peake's vector representation method. The right image (b) was determined using M&P's direct solution. Notice the two plots are identical in which the incoming 2D gust is stretched over the step as it is convected. The wave amplitude decreases and the wavefronts are distorted due to the stretching of the flow across the top of the step.
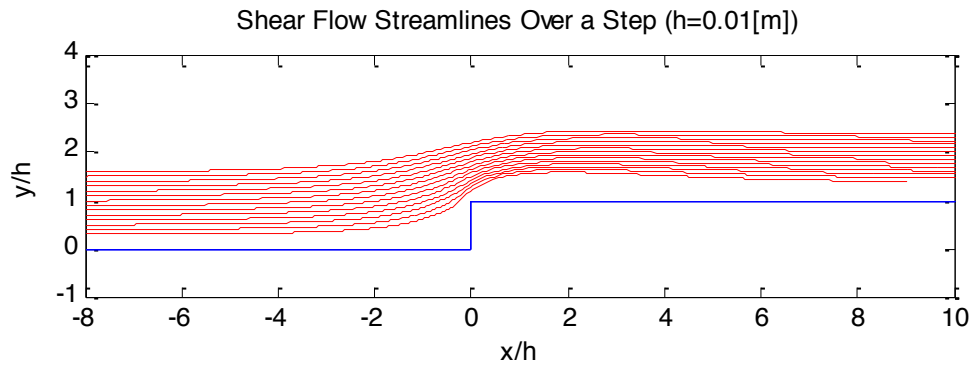
Figure 14: Shear flow streamlines over a forward-facing step. The shear flow is modeled by solutions to the RANS equations.
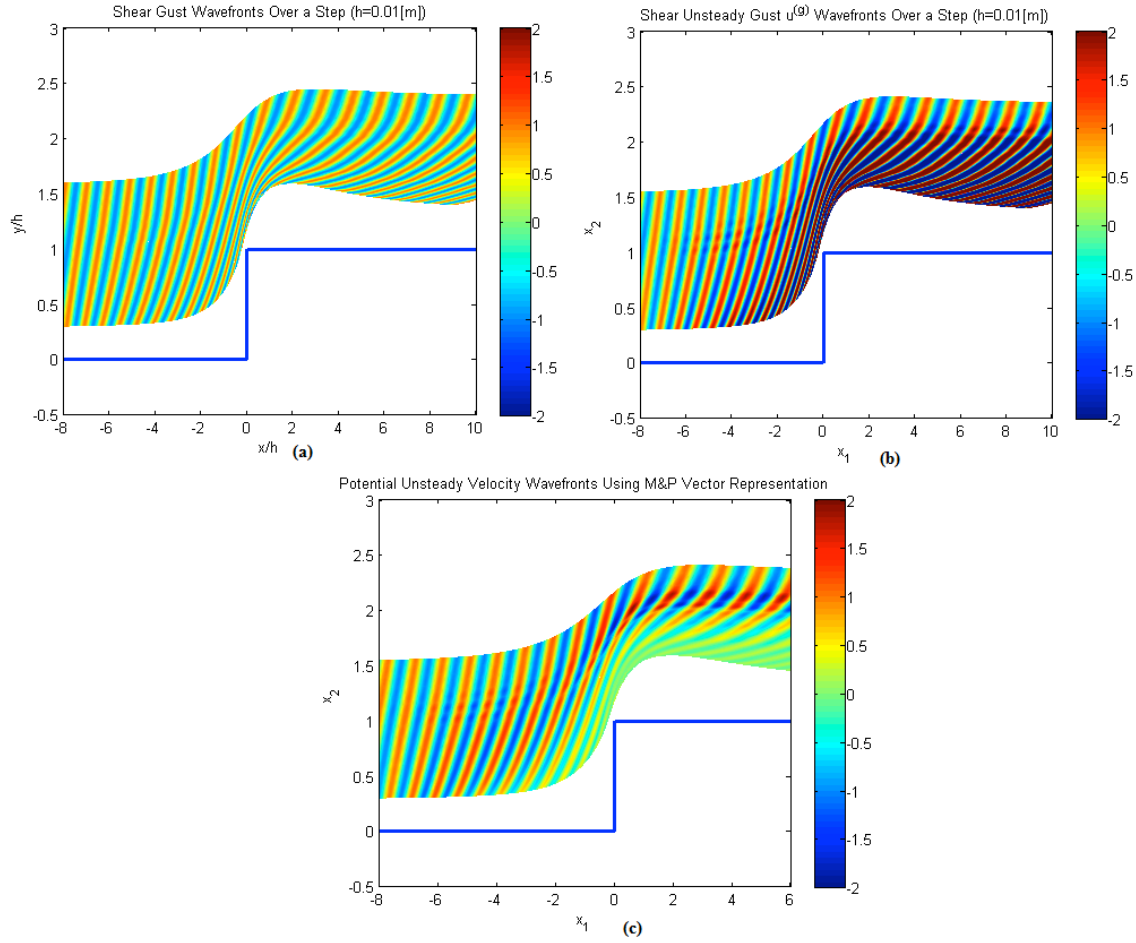
Figure 15: Shear flow over a step. The flow was modeled by RANS with a boundary layer thickness 120% of the step height. The distortion of a far upstream gust traveling at an angle of 45° is shown in (a). The amplitude of the wavefronts remains constant; however, it is observed that the wavefronts stretch as the flow is convected over the step. As the flow convects downstream, the fluid nearest to the top of the step appears to be slower contributing to the stretching behavior. Wavefronts of the unsteady gust $\mathbf{u}^{(g)}$ are shown in (b). It is observed there is a significant change in amplitude magnitude as the gust travels over the step. The wavefronts closest to the face and top of the step increase in amplitude and show the most distortion. This plot shows the pure distortion in this shear flow. Plot (c) shows the wavefronts of the Majumdar and Peake unsteady velocity. The amplitude decreases due to the wavefronts stretching as they are convected downstream over the step. It is also observed that there are less wavefronts as the flow convects downstream which contributes to the lengthening of the wavefronts due to the stretching behavior. There is a slight noticeable increase in amplitude in the middle of the flow which may be due to numerical error.
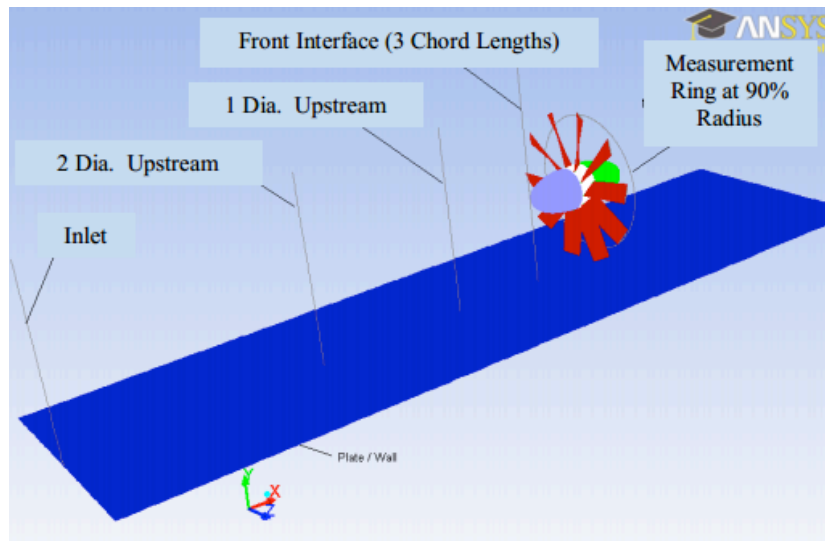
Figure 16: The configuration of the rotor and wall in which both potential and shear flows were modeled.
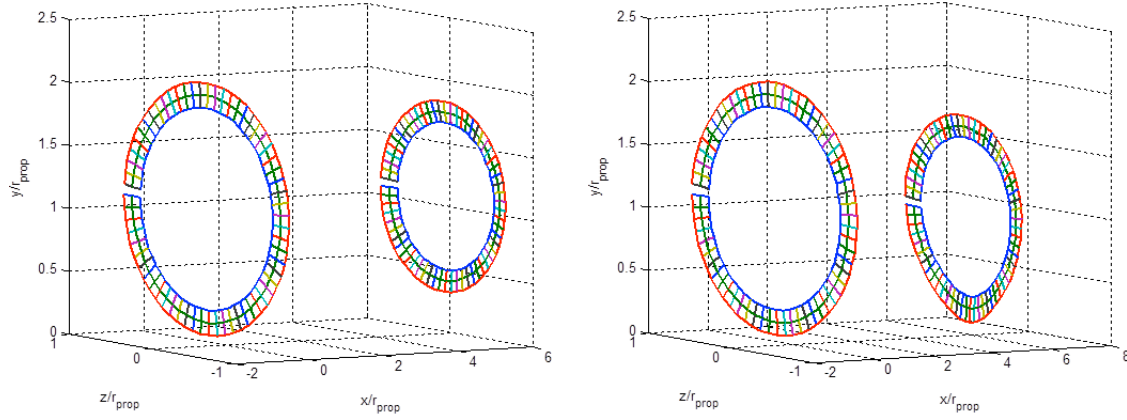
Figure 17: Potential flow ring distortion before and after convection (initial and final positions upstream of rotor) Case 2: J=0.48 without (left) and with (right) the wall present. Without the wall, the distortion of the ring is axisymmetrical. The ring is slightly compacted circumferentially. With the wall, the ring experiences non-axisymmetrical distortion. There is vertical stretching at the bottom where the ring is in contact with the wall.
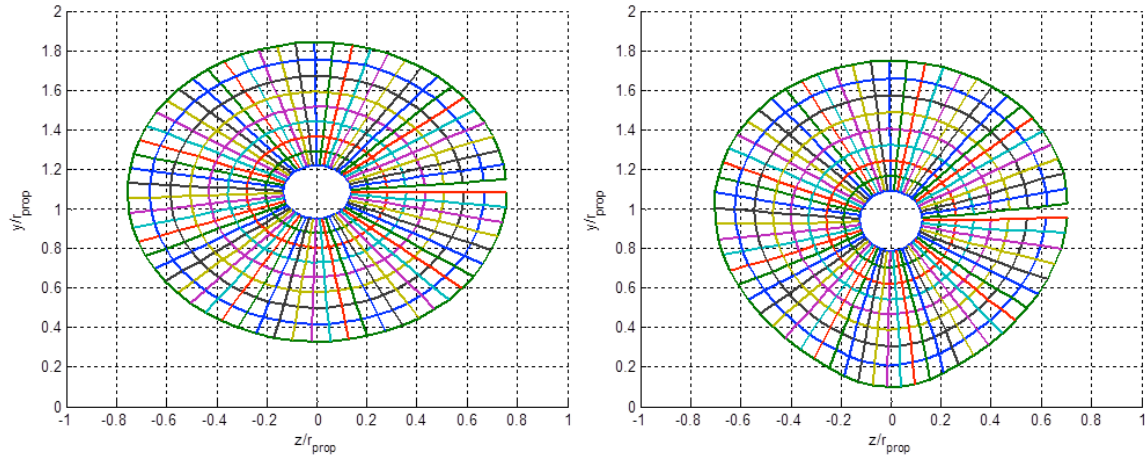
Figure 18: Potential flow 2-D projection of disc distortion at the rotor axis after convection at the final upstream position - Case 2: J=0.48 without (left) and with (right) the wall present. Without the wall, the distortion is axisymmetrically compacted. With the wall, it is non-axisymmetricaland has stretching at the bottom of the disc near the wall due to shearing of the flow.
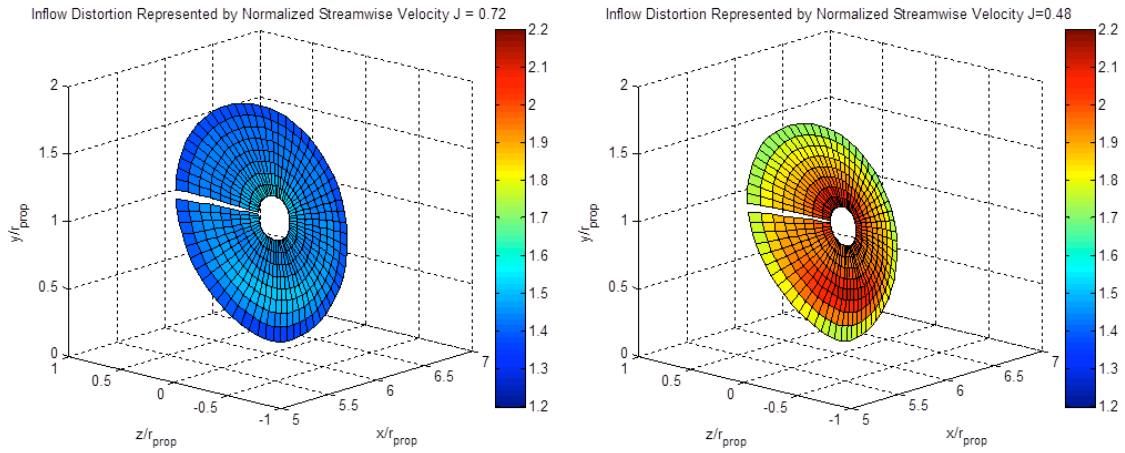
Figure 19: Potential flow surface contour disc distortion relative to streamwise velocity (normalized by unit radius) with wall present. Case 1: J=0.72 (left) and Case 2: J=0.48 (right). These plots represent the magnitude of distortion in the streamwise direction. The darker red areas are of higher velocities whereas the blue signifies lower velocities. In both cases, the most distortion occurs near the bottom of the disc where the material lines are slower near the wall and fast just above that, below the hub. For case 1, the normalized streamwise velocities range from 1.2 – 1.6 and for case 2 from 1.8 – 2.2. Case 2, which is the lower advance ratio case, is observed to have more significant distortion.
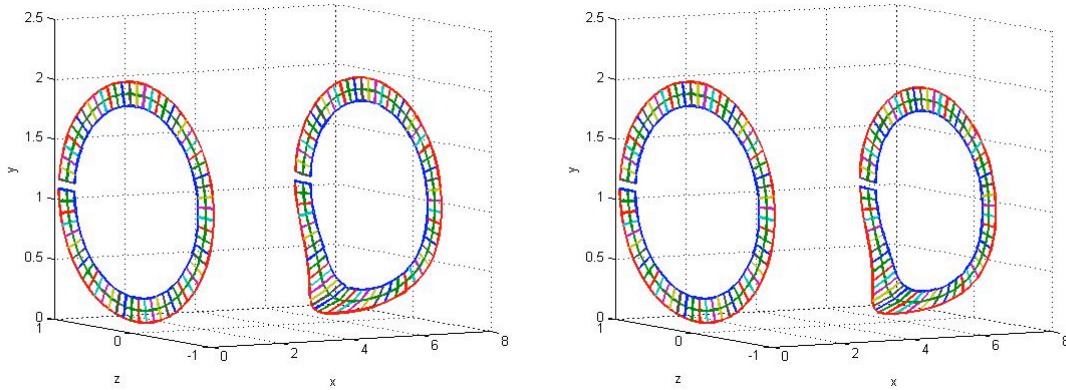
Figure 20: Shear flow ring distortion before and after propagation (initial and final positions upstream of rotor). Case 1: J=0.72 (left) and Case 2: J=0.48 (right) with the wall present. The ring experiences non-axisymmetrical distortion in both cases with vertical stretching at the bottom where the ring is in contact with the wall. This is due to the shearing of the flow at the wall. In case 2 the distortion is slightly more circumferentially compacted.
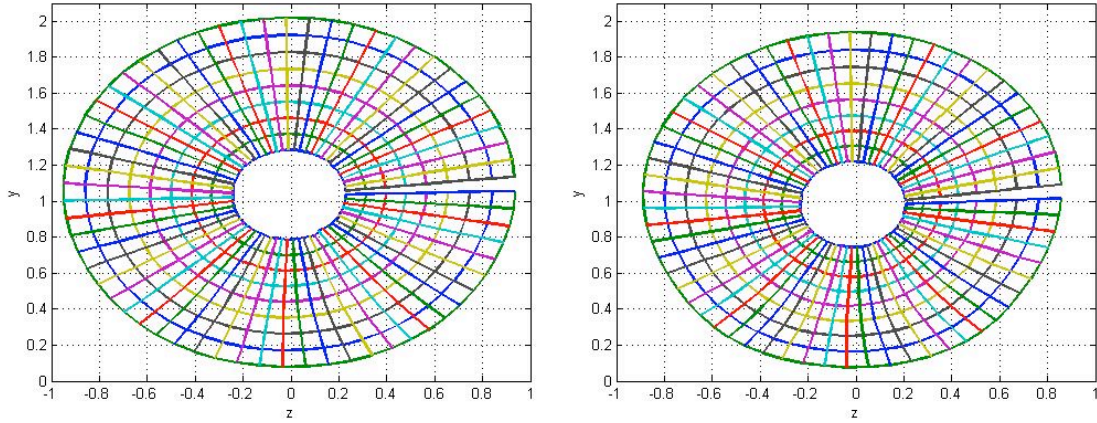
Figure 21: Shear flow 2-D projection of disc distortion at the rotor axis after propagation at the final upstream position - Case 1: J=0.72 (left) and Case 2: J=0.48 (right) with the wall present. In both cases the disc distortion is non-axisymmetrical and has horizontal stretching at the bottom of the disc near the wall due to shearing of the flow. In case 2 the distortion is slightly more circumferentially compacted and flatter at the bottom of the disc.
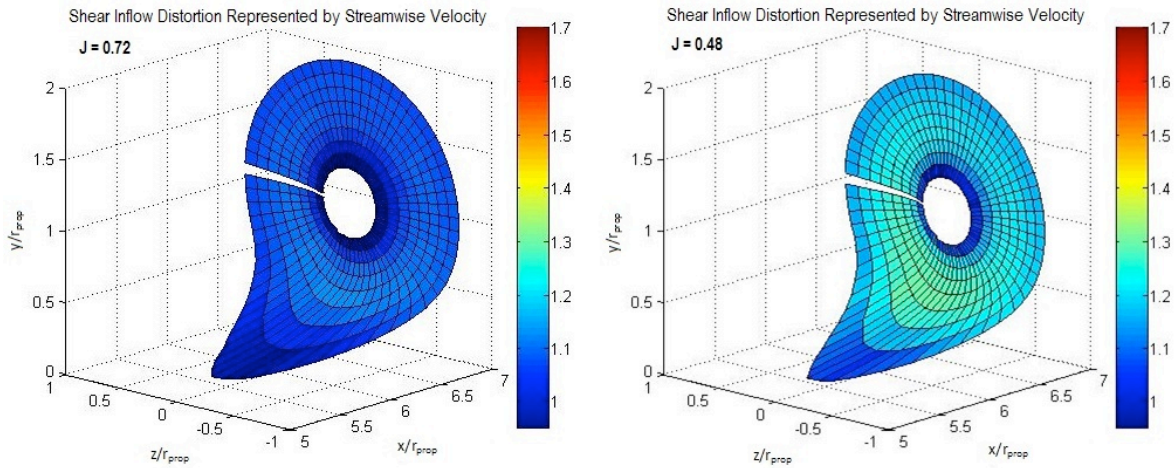

Figure 22: Shear flow surface contour disc distortion represented by the multiple reference frame RANS model relative to streamwise velocity (normalized by unit radius) with wall present. Case 1: J=0.72 (left) and Case 2: J=0.48 (right). These plots represent the magnitude of distortion in the streamwise direction. Note the significant shearing of the flow at the wall. The darker red areas are of higher velocities whereas the blue signifies lower velocities. In both cases, the most distortion occurs near the bottom of the disc where the material lines are slow near the wall and fast just above that, below the hub. For case 1, the normalized streamwise velocities range from 0.95 – 1.30 and for case 2 from 1.25 – 1.70.
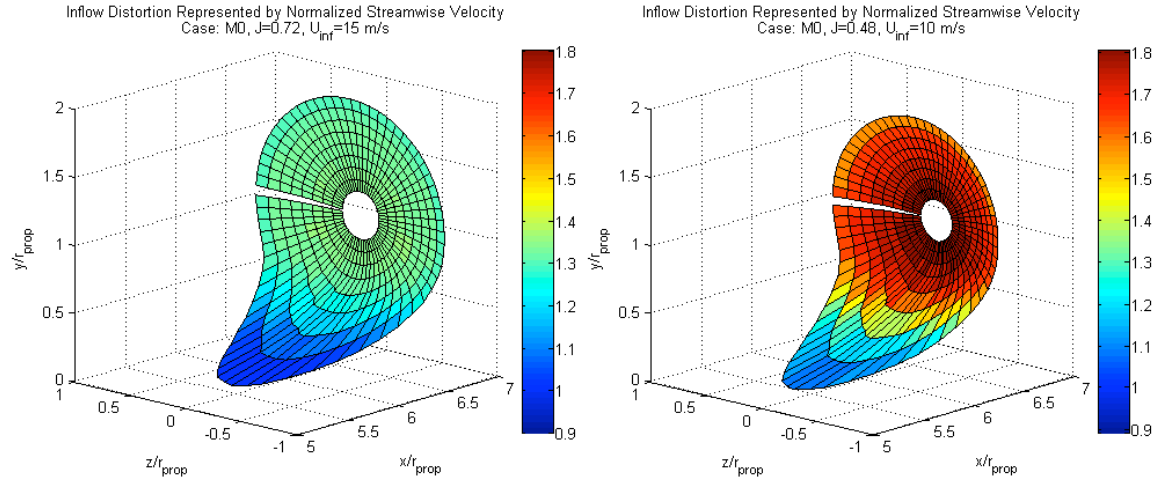
Figure 23: Shear flow surface contour disc distortion represented by the actuator disc RANS model relative to streamwise velocity (normalized by unit radius) with wall present. Case 1: J=0.72 (left) and Case 2: J=0.48 (right). These plots represent the magnitude of distortion in the streamwise direction. Note the significant shearing of the flow at the wall. The darker red areas are of higher velocities whereas the blue signifies lower velocities. In both cases, the most distortion occurs near the bottom of the disc where the material lines are slower near the wall. This model shows good agreement to the shear case using the MRF model in reference to the distortion shape; however, this model shows greater velocities compared to the MRF model.

APPENDIX

A. The unsteady velocity for a one dimensional gust in a potential vortex:

The drift coordinate gradients for a potential vortex are given

$$\nabla X_1 = \left(\frac{\partial X_1}{\partial x_1} \hat{x}_1, \frac{\partial X_1}{\partial x_2} \hat{x}_2 \right) = \{(\cos\theta + 2\theta\sin\theta)\,\hat{x}_1, (-\sin\theta + 2\theta\cos\theta)\,\hat{x}_2)\}$$

as

$$\nabla X_2 = \left(\frac{\partial X_2}{\partial x_1} \hat{x}_1, \frac{\partial X_2}{\partial x_2} \hat{x}_2 \right) = (\sin\theta\,\hat{x}_1, \cos\theta\,\hat{x}_2)$$

Consider a one-dimensional gust with an upstream velocity $A_2 = a_0 \sin(k_1(X_1 - U_\infty t))$. The velocity will be of the form $u_i^{(2)} = (u_1^{(2)}\hat{x}_1, u_2^{(2)}\hat{x}_2)$. Substituting in the drift gradients and applying the 1D upstream gust to the unsteady velocity solution from Majumdar and Peake (1998) given by

$$u_i = \tilde{A}_k(k) \frac{\partial X_j}{\partial x_m} \left(\delta_{im} - \frac{\kappa_i \kappa_m}{|\bar{\kappa}|^2} \right) \sin(k(X - \hat{i}U_\infty t)$$

and determining the local distorted wave number $\bar{\kappa}$

$$\bar{\kappa} = (\kappa_1, \kappa_2) = \left(k_1 \frac{\partial X_1}{\partial x_1}, k_1 \frac{\partial X_1}{\partial x_2} \right) = \{k_1(\cos\theta + 2\theta\sin\theta), k_1(-\sin\theta + 2\theta\cos\theta)\}$$

therefore,

$$|\bar{\kappa}|^2 = \kappa_1^2 + \kappa_2^2 = k_1^2(4\theta^2 + 1)$$

we then have the following solutions

$$u_1^{(2)} = |u_1^{(2)}| \sin\theta \sin(k_1(X_1 - U_\infty t))\,\hat{x}_1$$

$$u_2^{(2)} = |u_2^{(2)}| \cos\theta \sin(k_1(X_1 - U_\infty t))\,\hat{x}_2$$

where $|u_1^{(2)}|$ and $|u_2^{(2)}|$ are derived as the following:

For index $i=1$

$$|u_1^{(2)}| = a_0 \left\{ \frac{\partial X_2}{\partial x_1} \left[1 - \frac{\kappa_1^2}{|\bar{\kappa}|^2} \right] + \frac{\partial X_2}{\partial x_2} \left[-\frac{\kappa_1 \kappa_2}{|\bar{\kappa}|^2} \right] \right\}$$

$$= a_0 \left\{ \sin\theta \left[1 - \frac{(\cos\theta + 2\theta\sin\theta)^2}{4\theta^2 + 1} \right] + \cos\theta \left[\frac{(\cos\theta + 2\theta\sin\theta)(\sin\theta - 2\theta\cos\theta)}{4\theta^2 + 1} \right] \right\}$$

and similarly, for index $i=2$ we have

$$|u_2^{(2)}| = a_0 \left\{ \frac{\partial X_2}{\partial x_1} \left[-\frac{\kappa_1 \kappa_2}{|\kappa|^2} \right] + \frac{\partial X_2}{\partial x_2} \left[1 - \frac{\kappa_2^2}{|\kappa|^2} \right] \right\}$$

$$= a_0 \left\{ \sin\theta \left[\frac{(\sin\theta - 2\theta\sin\theta)(\cos\theta + 2\theta\sin\theta)}{4\theta^2 + 1} \right] + \cos\theta \left[1 - \frac{(-\sin\theta + 2\theta\cos\theta)^2}{4\theta^2 + 1} \right] \right\}$$

APPENDIX B: The unsteady velocity for a two-dimensional gust in a potential vortex:
A 2D gust is characterized by

$$\tilde{A}_1 = a_o \cos\phi \qquad k_1 = k_o \sin\phi$$
$$\tilde{A}_2 = a_o \sin\phi \qquad k_2 = -k_o \cos\phi$$

It then follows for a potential vortex that the local gust amplitudes are

$$u_1^{(g)} = a_o \left(\frac{\partial X_1}{\partial x_1} \cos\phi + \frac{\partial X_2}{\partial x_1} \sin\phi \right) = a_o \left(\cos\theta\cos\phi + 2\theta\sin\theta\cos\phi + \sin\theta\sin\phi \right)$$

$$u_2^{(g)} = a_o \left(\frac{\partial X_1}{\partial x_2} \cos\phi + \frac{\partial X_2}{\partial x_2} \sin\phi \right) = a_o \left(-\sin\theta\cos\phi + 2\theta\cos\theta\cos\phi + \cos\theta\sin\phi \right)$$

and the distorted wavenumbers are given as

$$\kappa_1 = k_o \left(\frac{\partial X_1}{\partial x_1} \sin\phi - \frac{\partial X_2}{\partial x_1} \cos\phi \right) = k_o \left(\cos\theta\sin\phi + 2\theta\sin\theta\sin\phi - \sin\theta\cos\phi \right)$$

$$\kappa_2 = k_o \left(\frac{\partial X_1}{\partial x_2} \sin\phi - \frac{\partial X_2}{\partial x_2} \cos\phi \right) = k_o \left(-\sin\theta\sin\phi + 2\theta\cos\theta\sin\phi - \cos\theta\cos\phi \right)$$

In order to obtain θ_g to determine the potential flow correction, we substitute the drift coordinate gradients into equation 3.6.8 which yields

$$\cos\theta_g = \frac{a_0 k_0 \left(2\theta(\sin^2\phi - \cos^2\phi) + 4\theta^2 \sin\phi\cos\phi \right)}{|\kappa| |u^{(g)}|}$$

where $|\kappa| |u^{(g)}|$ can be determined by the following

$$|\kappa| = \sqrt{\kappa_1^2 + \kappa_2^2}$$

$$= k_o \sqrt{\left(\cos\theta\sin\phi + 2\theta\sin\theta\sin\phi - \sin\theta\cos\phi \right)^2 + \left(-\sin\theta\sin\phi + 2\theta\cos\theta\sin\phi - \cos\theta\cos\phi \right)^2}$$

$$= k_o \sqrt{[(1+4\theta^2)\sin^2\phi - 4\theta\cos\phi\sin\phi + \cos^2\phi](\sin^2\theta + \cos^2\theta)}$$

$$= k_o \sqrt{(1+4\theta^2)\sin^2\phi - 4\theta\cos\phi\sin\phi + \cos^2\phi}$$

and

$$\left| \mathbf{u}^{(g)} \right| = \sqrt{\left(u_1^{(g)} \right)^2 + \left(u_2^{(g)} \right)^2}$$

$$= a_o \sqrt{\left(\cos\theta\cos\phi + 2\theta\sin\theta\cos\phi + \sin\theta\sin\phi \right)^2 + \left(-\sin\theta\cos\phi + 2\theta\cos\theta\cos\phi - \cos\theta\sin\phi \right)^2}$$

$$= a_o \sqrt{[(1+4\theta^2)\cos^2\phi - 4\theta\cos\phi\sin\phi + \sin^2\phi](\sin^2\theta + \cos^2\theta)}$$

$$= a_o \sqrt{(1+4\theta^2)\cos^2\phi + 4\theta\cos\phi\sin\phi + \sin^2\phi}$$

Part III: Noise Predictions for a Thrusting Rotor

1. Introduction

The first two parts of this report discussed the prediction of sound from a non thrusting rotor and the rapid distortion of boundary layer turbulence as it entered a rotor, as shown in Part 1:Figure 1. This section of the report will discuss the prediction of sound from the same rotor when it is operating at low advance ratios with a net positive thrust. The noise predictions will be based on the time domain method described in Part I, which requires as an input the turbulence velocity correlation function at the face of the rotor. For a thrusting rotor we will use equation 5.3.1 to estimate this parameter. This is only a approximate solution for the complete rotor inflow distortion, but it represents an upper bound when mean shear perturbations are ignored.

The experimental arrangement for the rotor operating in the Virginia Tech wind tunnel is described in Part I: section 4.1 and will not be repeated here. In this section of the report we will consider the rotor operating with advance ratios *J=0.96* and *J=0.72*. Measurements were also made at lower advance ratios, but these will not be considered as flow separation in the boundary layer near the rotor was observed experimentally at high thrust conditions and so the RDT approach will not work under these conditions.

In order to predict the unsteady flow at the rotor face RANS calculations were carried out for the rotor configuration described above. The sections 2 and 3 will describe the details of these calculations, and the features of the flow. This will be followed by a description of the rotor noise calculations for the thrusting rotor and a comparison with measurements.

2. RANS Calculations of the Rotor Inflow using the MRF Model

Adapted from Felipe Lachowski's Masters Thesis

2.1 Introduction

The calculation of the flow into a rotor near a wall is complicated by the interaction of the moving parts with the stationary wall. This requires the specification of a rotating mesh for the flow through the rotor and a stationary mesh for the flow over the wall, and this is described as a Multiple Reference Frame (MRF) model.

The multiple reference frame model (MRF) allows for the specifications of cell zones which are also known as subdomains. In the MRF model, the cells in the mesh do not move and the flow velocity is calculated relative to its frame of reference. However, in cases where rotating parts are present, the interactions between the subdomains are not accounted for in this model. The rotor is modeled by imparting a constant rotational velocity to the flow in its subdomain and so in the rotating domain all velocities are computed for given the position of the rotor. This is often referred to as the 'Frozen Rotor Approach'. This method clearly introduces errors if the velocities on the interfaces with the stationary domain are not uniform. However if only the upstream flow is of interest (as is the case in tis study) and the upstream interface is chosen to be sufficiently far upstream that the inflow is azimuthally independent of inter blade flow, then the

MRF model is a reasonable approximation. However inaccuracies will occur close to the blade tips, and this is a concern with this approach.

To overcome this problem an actuator disc model was also considered and will be described in section 3. In this model the rotor is replaced by a pressure jump in the flow and blade to blade interactions are ignored. This provided more detail about the flow close to the wall near the rotor tips and helped to confirm the experimental results that showed flow separation near the wall.

In this section we will first discuss the modeling of the rotor using the MRF approach and results that were obtained.

2.2 The Sevik Rotor

The Sevik rotor has blades with constant chord along its span (without skew) and squared tips. The blade pitch angle varies nonlinearly. Airfoil geometry is constant along the span with the max airfoil thickness at mid chord for both the root and tip profiles. These properties are summarized in Table 2.1

Table 2.1 – Rotor Geometry

ROTOR PROPERTIES	
Chord Length	57.2 mm
Blade Span	165.1 mm
Blade Pitch Angle (Root)	55.6 °
Blade Pitch Angle (Tip)	21.2 °
Diameter of Blade Plane	457.2 mm
Hub Diameter	127 mm
AIRFOIL DESIGN	
Max Airfoil Thickness (Root)	0.097 t/c
Max Airfoil Thickness (Tip)	0.84 c

The diagram of the blade profile and angle of twist is shown in Figure 2.1 with the angle of twist ranging from 55.6 degrees at the root to 21.2 degrees at the tip and linear interpolation was used to obtain the pitch at every spanwise cross section. The hub used in the calculations was simplified as shown in Figure 2.2.

The wind tunnel section represents the inclusion of the entire fluid around the rotor which is necessary in order to model the fluid flow in ANSYS – FLUENT. The dimensions of this section were created by minimizing the boundary effects on the flow, except in the floor region. Calculations were carried out with three different configurations as shown in Figures 2.3 and 2.4. The inflow direction is along the positive x-axis and in the configuration 2 and 3. The positive y-

axis direction is in the spanwise direction towards the rotor and normal to the near wall. The z-axis follows the right hand rule. All three configurations use the same coordinate system directions.

The origin is placed at the inlet as shown by Figure 2.3 and 2.4, so that the tip of the front hub cone is at coordinates (1500, 0, 0). The dimensions were determined based on measurements in terms of diameters of the rotor. The distance upstream of the rotor spanwise centerline is slightly greater than three and a half diameters in length. The distance downstream of the rotor spanwise centerline is slightly greater than seven diameters in length. The lateral distances are slightly larger than three diameters and in the case of configuration 1, the lateral distance extends in both y and z directions removing any near wall effects. The only difference between configuration 1 and configuration 2 and 3 is the proximity of the wall. In configuration 2 and 3 the wall was placed as in the experimental setup. The clearance between the blade tips and the wall is 20.3 mm which leads to a distance from the hub center to the wall of 248.90 mm. Other dimensions were solely based on preliminary CFD computations of different model setups and lengths. After several trials, these dimensions presented zero boundary effects. Figure 2.5 shows the size of the domains and the dimensions of the rotational domain.

The rotational domain is shown in 2.5(c) and is the same dimensions for all three configurations. This domain encases the entire rotor up to three chord lengths in front and behind the rotor disc plane. The radial extension is limited to 102% of the rotor's diameter. If this region was larger radially, possible unphysical flow could be expected. The domain length was chosen as three chord lengths in either direction in order to fully encase the hub sections and most importantly, obtain a relatively uniform flow at the interface of the rotational domain. This is a requirement for utilizing the MRF model as mentioned previously. The rotational domain was based on a SolidWorks drawing of the rotor and then exported as an IGES file into the meshing software which will be discussed in the next sections.

2.3 Mesh

The mesh was produced using ANSYS – ICEM software and then imported into ANSYS – FLUENT as a mesh file.

2.3.1 The Stationary Domain

The stationary domain is the wind tunnel section excluding the rotational domain. This is equivalent to the domain shown in Figure 2.5 (a) or (b) subtracting Figure 2.5(c). Figure 2.6(a) and (b) show the mesh for the stationary domain excluding the rotational domain and rotor. The yellow region in 2.6(b) is a portion of the wall that was strategically separated from the surrounding walls in order to obtain full control of mesh sizes and inflation rate for that region only, thus reducing the need to refine the entire wall region. Doing so reduces total element size and at the same time refines the regions of interest. The inlet is shown in blue and the outlet is in red. Notice how the center of 2.6(a) and (b) are refined due to the mesh densities placed at the inlet. The stationary domain contains approximately 47% of all elements within the grid while the remainder are located within the rotational domain Figure 2.6(c).

2.3.2 The Rotational Domain

Over half of all elements are located within this subdomain due to the need for refinement to accurately represent the flow. This region contains complex flow features such as

swirl, which increases diffusion and numerical error. Therefore, in an attempt to minimize these errors, reduced elements sizes were used, as well as, tetrahedral inflation rates. A single mesh density was strategically located in this region to enforce inflation in regions of interest. Figure 2.6 (c) shows the mesh for the rotational domain including the interface in front of the rotor in blue and the interface behind the rotor in red. The rotor is seen within the domain. The rotor surface does not allow penetration of fluid.

2.3.3 Mesh Refinement and Densities

In order to accurately capture the flow characteristics and quantities a well-developed mesh is necessary. Flows where the boundary layer is of interest require a locally structured mesh comprised of rectangular prism or hexahedral elements; however, for complex geometries obtaining such mesh characteristics becomes more complex and is limited by the meshing. If prism layers are formed at surfaces it is required to ensure that the overall mesh quality has not been degenerated due to geometry complexities. Prism layers were attempted; however, the overall mesh quality was found to be reduced drastically. Therefore, an unstructured mesh was created in surface regions and tetrahedral elements were used to replace the elements in the boundary layer. Several meshes were generated and computed using different inflation ratios and element sizes until a final mesh was obtained. Reasonable results for boundary layers are still attainable even without the use of a prism layer for boundary layer regions; however, this is an area for improvement and refinement.

The domains and subdomains were refined depending the flow characteristics. In this setup, the mesh was not scaled; the maximum element size was set to 200 and the minimum to 1. Surface curvature and proximity based refinement was utilized in order to capture the blade edges correctly. This however, created small elements at the blade root where the hub meets the blade. Since no filets were created, ANSYS – ICEM attempts to recreate the surface by placing minimum sized elements in the corners, which later introduce problems related to wall y-plus values in the solver. If the mesh sizes in this region were larger, ANSYS – ICEM would not be able to correctly mesh these sharp corners and thus would create additional surfaces to patch the sharp corners.

The regions of interest include the flow leading up to the rotor, as well as, the rotor wake region. Configurations 2 and 3 need an additional refinement for the boundary layer region near the wall. Therefore, a mesh density was set for all configurations shown in Figure 2.7. In Figure 2.7(a), the darker region is the wake refinement density set to a maximum size of 50 while the orange region is the boundary layer refinement density set to a maximum size of 20 with inflation ratio of 1.3. Inflation ratios are set to zero in these densities unless otherwise state. This inflation dictates the ratio increase in tetrahedral size in the outer portions of the grid. This allows the solver to fully capture the boundary layer profiles. The wake refinement includes a rectangular prism initiating at the inlet and extending past the rotor to a length of 2650 mm. with edge lengths of 600mm and center located at the origin. Therefore it encompasses the rotor blades entirely and extends through the downstream wake region. The boundary layer refinement region exists only in configuration 2 and 3 and is another rectangular prism set flush with floor and extending in the y-direction 102 mm (boundary layer height). It also initiates at the inlet and extends 2224 mm in the x-direction. This allows for refinement in the boundary layer past the regions of measurement. This refinement is applied for configuration 2 and 3 with the same density box dimensions. Another density refinement applied for all configurations is a triangular prism shaped density zone. This is shown in Figure 2.7(b). It extends within the rotational

domain and refines the region of measurement for comparison to experimental data. The dimensions include a base initiating at *x* value of 1837 mm outwards to an *x* value of 1990 mm. There is an inflation ratio of 1.1 for the exterior of this region. The triangular shape allows for further refinement within the regions of experimental measurement. Another feature is the restrictions on the surfaces which limit the growth of tetrahedral elements. Limitations were placed along the entire rotor surface, wall boundary layer section shown in yellow in Figure 2.6 (b), along the rotational domain interfaces, and within the fluid region of the rotational domain. Together these densities and refinements produced a final mesh of 3, 819, 656 total elements for configuration 1 and 5, 128, 872 total elements for configuration 2 and 3.

The main refinement difference between configurations 1 and 2 or 3 is in the wall region as shown in Figure 2.8.and 2.9. Notice that all configurations include refined regions at the interfaces, as well as, the blades. The unstructured mesh in Figure 2.10(a) clearly shows the inflation applied to the surfaces and at the boundary layer regions. Comparing Figures 2.8 and 2.9 shows that the refinement at the bottom of the rotor in configuration 1 is the same as in the top region. Since it is an axisymmetric flow without wall influences refinement is not needed at the bottom region in this case. A general circumferential refinement can be applied.

Refinements of the stationary and rotational domains are shown in full detail in Figure 2.10(a) and (b) respectively. Notice how well defined the rotational domain is compared to the stationary domain. This was necessary in order to obtain grid independence in this region. Figure 2.11(a) and (b) show a cross section in the XY plane of the mesh definition at the rotor surface and boundary between the blade tips and near wall. These are regions were locally structured prism layer mesh are most beneficial.

The mesh quality was checked and all elements were found to be above 0.30 for tetrahedral elements in all configurations, and the skew and aspect ratios met all requirements.

2.4 Solver

A pressure based solver and an absolute velocity formulation was chosen to perform the computation. The MRF fluid model was chosen for steady state computation of the rotor in different configurations. Given that the experimental testing of the rotor was in air, the same fluid was chosen for CFD analysis.

2.4.1 Turbulence Models

The turbulence model used in the solver was the Spalart–Allmaras (S.A.) model because of its ability to resolve boundary layers for external flow and its performance under adverse pressure gradients. Several other turbulence models were tested including κ - ϵ standard model, κ - ϵ realizable model, κ - ϵ model with and without near-wall treatments, $\kappa - \omega$ standard, $\kappa - \omega$ SST, and the Reynolds Stress model. One of the main reasons for choosing the Spalart–Allmaras model was because of the type of mesh generated. Spalart–Allmaras is less demanding than the other turbulence models and allows for an unstructured mesh to be used and corrects for poor mesh regions along the walls where meshing is most complicated for complex geometries. Using the mesh generated for this project, all other models (RSM, κ - ϵ, and $\kappa - \omega$) produced similar results to the S.A. model. The constants used for this turbulence model are listed in Table 2.2. The S.A. production option chosen was vorticity–based; however, to increase resolution of vortices a strain/vorticity–based production is recommended. Both options were attempted and showed little to no difference in results. This is in part due to the MRF limitations and inability to resolve vortices shed from the blade tips as this is a fluid instability.

Table 2.1 – Spalart – Allmaras Model Constants

MODEL CONSTANTS	
C_{b1}	0.1355
C_{b2}	0.622
C_{v1}	7.1
C_{w2}	0.3
C_{w3}	2
Prandtl Number	0.667

2.4.2 Cell Zone Conditions

Cell zone conditions were equal for all configurations, except for configuration 3. However, all configurations and flow conditions shared the same frame motion characteristics. They all included two zones, the stationary and rotational zone. The stationary zone and rotational zone each include its own reference frame. Table 2.3 and Table 2.4 show the details of the setup of these reference frames depending on flow conditions.

Table 2.2 – Stationary Zone: Cell Zone Conditions

ALL CONFIGURATIONS AND DATA SETS	
Rotation – Axis Origin	(0, 0, 0)
Rotation – Axis Direction	(1, 0, 0)
Translational Velocity	0 m/s
Rotational Velocity	0 RPM
Relative Specification	Absolute
UDF: Zone Motion Function	None

The stationary zone does not require translational velocity since that inflow velocity is applied as a boundary condition.

Table 2.3 – Rotational Zone: Cell Zone Conditions

ALL CONFIGURATIONS EXPERIMENTAL DATA SET	CONFIGURATION 3 ACOUSTIC DATA SET
Rotation – Axis Origin	
(0, 0, 0)	

Rotation – Axis Direction	
(1, 0, 0)	
Translational Velocity	
0 m/s	
Rotational Velocity	
1500 RPM	
2000 RPM	2734 RPM
2502 RPM	
2734 RPM	
Relative Specification	
Absolute	
UDF: Zone Motion Function	
None	

The rotational cell zone conditions only change for Configuration 3 since the results obtained for these cases will be used for RDT calculations.

2.4.3 Boundary Conditions

Table 2.5 shows the setup for all of the wall conditions.

Table 2.4 – Wall Boundary Conditions

ROTOR SURFACE	WIND TUNNEL SURFACE
Adjacent Cell Zone	
Rotational Cell Zone	Stationary Cell Zone
Wall Motion	
Moving Rotational Wall	Moving Rotational Wall
Motion	
Relative to Adjacent Cell Zone	Absolute
Speed	
0 RPM	0 RPM

Rotation – Axis Origin
(0, 0, 0)
Rotation – Axis Direction
(1, 0, 0)
Shear Condition
No – Slip Condition
Wall Roughness
Height of 0 mm (smooth wall) and roughness constant of 0.5 (default)

The inlet boundary conditions are given by Table 2.6.

Table 2.6– Inlet Boundary Conditions

CONFIGURATION		
1 and 2	**3**	**3**
EXPERIMENTAL DATA		**ACOUSTIC DATA**
Velocity Specification Method		
Components		
Coordinate System		
Cartesian		
Reference Frame		
Absolute		
X - Velocity		
Constant 15 m/s	UDF 15 m/s	UDF 10m/s
		UDF 15 m/s
		UDF 20 m/s
Constant 30 m/s	UDF 30 m/s	UDF 25 m/s
		UDF 30 m/s
TURBULENCE		
Turbulent Intensity		

1 %	
Hydraulic Diameter	
1795.23 mm	

User Defined Functions (UDF) were utilized in order to apply an inlet boundary layer with a height of 102mm and a case by case nominal inflow velocity. Configuration 1 and 2 applied constant inlet velocities which varied from 15 m/s to 30 m/s depending on the advance ratio. Note that for configuration 1, the rotor is in the middle of the domain with zero wall influence except for the no-slip condition on the rotor surface. Configuration 2 does have a wall, but, no special functions were applied for the boundary layer definition. Hence, the inlet velocity is constant throughout, except for the boundary layer created by the no-slip condition. Configuration 3 has a thick boundary layer of 102 mm in height applied by the UDF. This is the same boundary layer applied for the acoustic data set, the only difference being the varying boundary conditions set by the rotational velocity in the cell zones and the inlet velocities. The UDF code generated for the 15 m/s case is shown in Lachowski (2013). These UDFs were individually loaded into ANSYS − FLUENT and set as the *x*-velocity component. The *y* and *z* velocities were set to zero. In the case where the *x*-velocity is constant no UDF was selected.

Lastly, all other boundary conditions were the same for all configurations and data sets. The outlet was set as an outflow surface with a flow rate weighting of one. This ensures that the mass conservation is applied to this boundary and relates to the mass flow through the inlet since there is no mass flow through the wind tunnel walls.

2.4.4 Initialization

The first thirty iterations were performed using first order discretization for all types. After these thirty iterations, the order of discretization was increased to second order for two hundred additional iterations. This was followed by five total reductions of under-relaxation factors. These reductions were spaced apart by fifty to forty iterations. The under-relaxation factors initiate at their default values and decrease to 0.05 for modified turbulence viscosity, 0.05 for turbulence viscosity, and 0.2 for body forces. Explicit relaxation factors and courant numbers were left unchanged. The residual were scaled globally. The criteria used for the residuals are shown in Table 2.7. The range given for continuity residual indicates that the solutions required a maximum of 0.01 to a minimum of 0.001in residual values in order to obtain convergence.

Table 2.7– Residual Criteria

RESIDUAL	ABSOLUTE CRITERIA
Continuity	0.001 - 0.01
X – Velocity	0.001
Y – Velocity	0.001
Z – Velocity	0.001
Modified Turbulence Viscosity	0.001

2.4.5 Computation Solution Methods

The solution methods used for the final 90% of all iterations are shown in Table 2.8. Several other methods were attempted prior to choosing these final settings. They include using the standard, second order, and body force weighted pressure interpolation schemes.

Table 2.8 – Solution Methods Settings

SOLUTION METHODS	
Pressure – Velocity Coupling	
Scheme	Coupled
Spatial Discretization	
Gradient	Least Squares Cell Based
Pressure	Second Order
Momentum	Second Order Upwind
Modified Turbulent Viscosity	Second Order Upwind

Additionally, momentum and modified turbulent viscosity discretization were also changed from first order up to third order MUSCL. Fist order was used for initialization; however, third order MUSCL was used to determine if greater accuracy is possible. Comparison of second order and third order MUSCL results show little to no difference in results. Therefore, the extra computational effort needed for third order MUSCL scheme was avoided by using second order scheme for both momentum and modified turbulent viscosity.

2.5 Grid Independence Study

A grid independence study was performed for all configurations; however, only the grid difference for configuration 3 will be shown. Table 2.9 shows five different grid sizes initiating with the original mesh, referred to as mesh zero, and increasing refinement in strategic locations until a final converged grid is used for final results computation. Results for each case for configuration 3 were run for each mesh generated. The solutions were compared and plotted, for each case and mesh, along the 90% radius circumferential line shown in Figure 2.13. The flow velocities were found to converge to within 3%.

Table 2.9 – Configuration 3: Grid Independence Study

GRID INDEPENDENCE STUDY		
Grid Number	**Total Element Size**	**Refinement Description**

0	679, 254	Original coarse mesh
1	1, 748, 134	Add: Wake mesh density, surface refinements
2	2, 547, 426	Add: Prism Layers to surfaces
3	2, 557, 232	Remove: Prism Layers from surfaces Add: BL mesh density, wake mesh density and surface refinements
4	4, 243, 693	Add: Wake measurement plane mesh density
5	5, 128, 872	Add: Refine wake measurement plane mesh density, refine rotor surface

In addition, a convergence check of the boundary layer was made at 0.79 m. upstream of the rotor. The results are shown in Figure 2.14. The results show almost identical values at all points. The grid study showed that between the third and fifth mesh, equivalent results were being acquired. Mesh three could have been used for all computations, however, the refinement of mesh five produced smoother results and was therefore a more attractive choice.

2.6 Results

The details for the flow through the rotor can be found in Lachowski(2013) and here we will only present the results for the distortion and acceleration of the wall boundary layer flow, since this is most relevant to the noise calculations to be presented in section 4.

Figures 2.15 through 2.35 show the boundary layer profiles on the axis of the rotor for each flow speed of interest. The advance ratio is defined for each case and varies between 0.48 and 1.44, the highest being the no thrust case. Figure 2.36 shows the calculated performance characteristic of the rotor, with a maximum thrust coefficient of 0.4 at an advance ratio of 0.48.

In Figures 2.15-20 the boundary layer profile is compared at different upstream locations. Each curve on the plot refers to a different advance ratio. It is seen that the profile is distorted differently for each advance ratio and the largest effects occur close to the rotor disc plane. In Figures 2.18-2.20 the effect of the hub is shown and causes a large drop in level at hub height (~2.2 δ). Under the hub the flow is accelerated significantly at the lower advance ratios, and Figure 2.19 and 2.20 show the presence of reverse flow near the wall, indicating a possible region of flow separation that occurs at high thrust.

Figures 2.21-2.25 show the development of the boundary layer with downstream distance, in the region upstream of the hub (more than one diameter upstream). Each figure is for a different advance ratio, and the largest effects are seen for the highest thrust (lowest advance ratio) case. At advance ratios of 0.96 and above very little effect is observed. More dramatic effects are observed between the front of the hub and the rotor disc plane as shown in Figure 2.26-35. In these figures the region above the hub and the region below the hub have been plotted separately.

The reverse flow is clearly shown in Figure 2.27 and 2.29, but Figure 2.31 indicates that there is no reverse flow for the advance ratio of *J=0.96*.

2.7 Conclusions

This section has described the detailed RANS calculations of the flow into the rotor tested in the Virginia Tech Wind Tunnel in a companion project. These calculations were based on the MRF model of the rotor which includes all the details of the rotor in a rotating frame of reference, and evaluates the wind tunnel flow in a fixed frame of reference. The method assumes a smooth interface between the flow in the fixed frame, and the rotating frame used to specify the flow near the rotor. While this appears to be a significant limitation the approach has provided some valuable insights into the problem. First the operating characteristics of the rotor (Figure 2.26) have been obtained and, secondly, the boundary layer profiles on the fixed wall near the rotor indicate that there is a reverse flow region near the rotor disc plane at the higher thrust conditions. This will be investigated further in the following section.

3. RANS Calculations of the Rotor Inflow using an Actuator Disc Model

3.1 Introduction

In the previous section a RANS calculation was described that was based on an MRF model. This showed that there was the possibility of reverse flow close to the rotor disc, but there was a concern because, in this region, the mesh included the interface between the rotating grid required for the flow near the rotor and the stationary grid required to describe the flow near the wall. To address this issue a calculation was also performed using an actuator disc to replace the rotor. The implementation of this model followed the same steps as were described in section 2, but the rotating frame was removed and replaced by a thin disc which supported a uniform pressure jump that corresponded to the thrust developed by the rotor. These calculations were carried out both with and without a rotor hub.

3.2 Results

The actuator disc model was verified by comparing it to the potential flow model given by Conway (1995, see part II), with a set of image sources to account for the presence of the wall. The results are shown in Figure 3.1 for an advance ratio of $J=0.72$ for the actuator disc RANS calculation implemented with zero viscosity. The two calculations are seen to be in close agreement as expected. The effect of the viscous flow in the wall boundary layer is shown in Figure 3.2 for the same conditions, and the difference with the Conway calculation is clear in the near wall region.

The concern about the reverse flow effect near the wall is illustrated in Figure 3.3, which also shows the mesh used to define the actuator disc surface. This figure shows the flow 1mm above the plate surface for an advance ratio of $J=0.48$. Clearly seen is the change in flow direction in the area between the rotor disc and the wall. The reverse flow dominated at advance ratios $J=0.48$, were small at an advance ratio of $J=0.72$, and negligible at $J=0.96$.

An alternate view of the reverse flow calculation is shown in Figure 3.4, which gives the flow in a vertical slice through the axis of the rotor. The reverse flow is seen to extend into the rotor disc plane at the blade tip. The pressure jump across the disc is set to be constant in these calculations and not affected by the local flow. The separation near the wall is likely to be more severe when the dynamic loading on the rotor is taken into account.

The computational results have also been compared to the flow visualizations made in the Virginia Tech Wind Tunnel using wool tufts, as shown in figure 3.5. Remarkably good agreement is found and the extent of the separated flow appears to be well modeled by the CFD. This will clearly have an important impact on the inflow turbulence close to the rotor, and suggests that the unsteady flow may be self induced as distinct from an inflow turbulence effect.

4. Noise Calculations for a Thrusting Rotor

4.1 Approach

The approach used to calculate the noise radiated by a thrusting rotor is based on the time domain method described in part I of this report. This calculates the radiated noise from the four point correlation function of the unsteady flow in the rotor disc plane. To obtain the correlation function for a thrusting rotor the distortion of the flow in the vicinity of the disc plane must be taken into account, and this is achieved by using the methods described in part II of this report. The inflow distortion requires a specification of the mean flow which is obtained by using the RANS calculations described in the previous section for the actuator disc model. Since the reverse flow effects were significant at the lowest advance ratio *J=0.48*, only the results from advance ratios of *J=0.72* and *J=0.96* will be considered.

One of the major issues in this calculation was deciding the point at which the rapid distortion of the turbulence should be initiated. Figure 4.1 shows the impact on the material surface by starting the calculation at different points upstream of the rotor disc plane. In the left figure the distortion is started 6 radii upstream of the rotor disc plane and considerable distortion is found to occur. However the turbulence in the boundary layer is continually evolving and so it appears reasonable to take this feature into account by limiting the distortion to one Largranian lengthscale, which is approximately one boundary layer thickness, or half a rotor radii. The right hand part of Figure 4.1 shows the material surface for the flow distorted over this limited scale, and the effects are seen to be much smaller.

The input turbulence was taken from the four point correlation function measured in a companion project at Virginia Tech was described in Part I of this report. Noise calculations were carried out at multiple angles to the rotor axis and compared to acoustic measurements made in the Virginia Tech Wind Tunnel.

4.2 Predicted Spectra

Predictions of the far field noise spectra are shown in Figure 4.2-4.5. For a receiver at 29º to the rotor axis and the higher advance ratio (lower thrust) of *J=0.96* the predictions are quite consistent with the measurements, but interestingly the calculations without distorting the turbulence using RDT are better than when the distortion is included. This conclusion is emphasized in Figure 4.3 which shows the same comparison with measurements at the lower advance ratio (higher thrust) of *J=0.72*. The distortion has only a small effect on the predicted spectra at high frequencies but the distortion lowers the levels at frequencies close to the blade passing frequency. This is a consequence of the rapid distortion lowering the levels of the turbulence in the mean flow. Furthermore at the lower advance ratio the haystacking is more pronounced, presumably because the flow is slowing through the rotor and the mean flow turbulence is no correctly characterized by the upstream boundary layer characteristics.

The calculations at different angles to the rotor axis are shown in Figures 4.4 and 4.5 for each advance ratio. The levels at 52º to the axis are in general lower than the levels at the other angles due to the expected dipole type directivity from the far field noise. The spectral shapes are complete consistent with the predictions and measurements at other angles, with more pronounced haystacking at the lower advance ratio and lower predicted levels close to blade passing frequency when the distortion is included.

5. Conclusions

The third part of this report has shown how a time domain approach to rotor noise prediction, based on measured inputs with no intermediate turbulence modeling, has been combined with rapid distortion theory to predict the far field noise from a thrusting rotor. The approach used for the rotor noise prediction was the same as used in Part I of the report that based the predictions on the four point velocity correlation function in the plane of the rotor. The measured correlation function was corrected for mean flow distortion using Batchelor and Proudmans form of Rapid Distortion Theory (in which the mean shear remains undistorted).

Implementation of RDT requires the calculation of the mean flow and this has been carried out using three different inflow models, a RANS model with a multiple reference frame grid, a RANS model with an actuator disc replacing the rotor, and a potential flow model with an actuator disc. The RANS model with the actuator disc was found to be most satisfactory and was consistent with flow visualizations in the wind tunnel experiment. One of the most important conclusions from this study was that the flow in the boundary layer near the rotor showed the effect of separation at the lower advances ratios. This will cause the boundary layer turbulence to be significantly modified and the RDT approach is not suitable for these conditions. There was also an issue as to where the RDT calculation should be started to properly reflect the effect of the distortion on the turbulence. It was concluded that this should be one Lagranian lengthscale upstream of the rotor disc plane.

The predicted noise levels for a thrusting rotor were compared to measurements at three different angles to the rotor axis and at two different advance ratios. The agreement between the measurement and predictions was good at high frequencies. However, around the blade passing frequency where haystacking effects were most dominant, the measured levels were underpredicted, and the RDT correction was shown to reduce rather than increase the predicted levels. It was concluded that for a thrusting rotor the effect of separation in the boundary layer near the disc plane and its effect on the turbulence needed to be modeled more accurately.
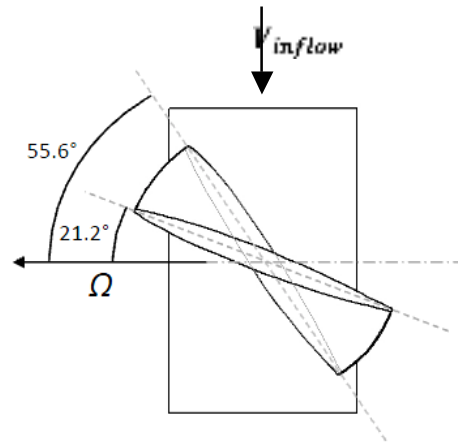
Figure 2.1 – Single Blade Diagram of Blade Twist and Flow Direction Showing flow direction and blade rotation. Blade twist varies nonlinearly from 55.6° (root) to 21.2° (tip). Figure obtained from Glegg et al. [6].
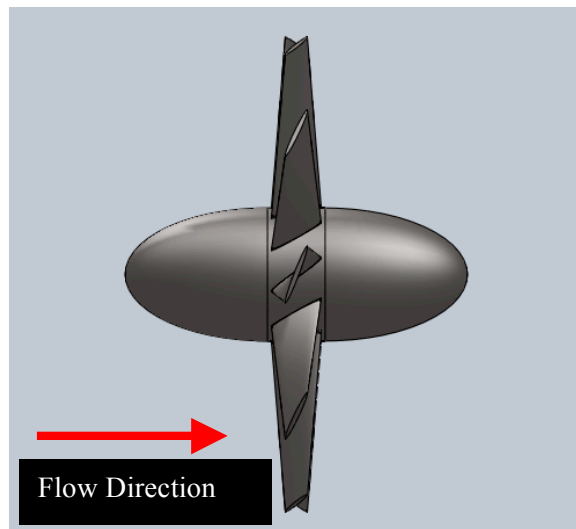
(a)

Flow Direction

(b)

Flow Direction

(c)

Flow Direction
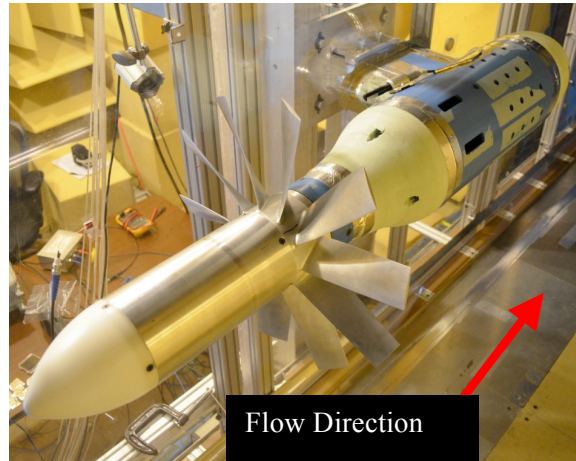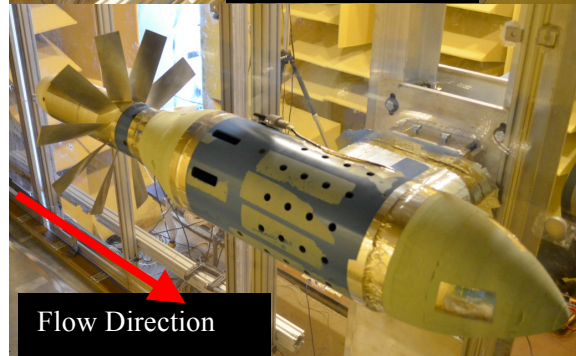
Figure 2.2 – Geometry Differences (Hub)

(a) Actual Rotor - Showing anterior section of hub.
(b) Actual Rotor - Showing posterior section of hub.
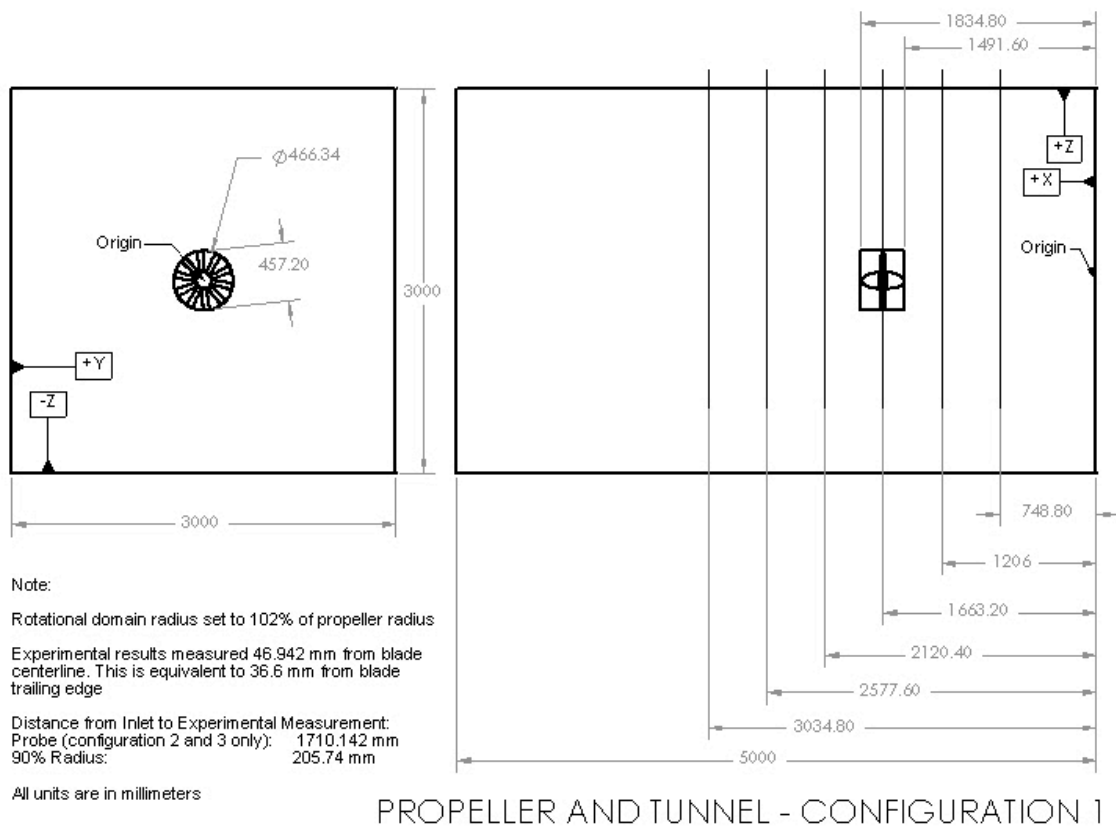**(c) CAD model - Showing simplified hub sections.**

PROPELLER AND TUNNEL - CONFIGURATION 1

Note:

Rotational domain radius set to 102% of propeller radius

Experimental results measured 46.942 mm from blade centerline. This is equivalent to 36.6 mm from blade trailing edge

Distance from Inlet to Experimental Measurement:
Probe (configuration 2 and 3 only):   1710.142 mm
90% Radius: 205.74 mm

All units are in millimeters

Figure 2.3 – Drawing of Configuration 1

PROPELLER AND TUNNEL - CONFIGURATION 3

Note:

Tip Gap: 20.3mm

Rotational domain radius set to 102% of propeller radius

Experimental results measured 46.942 mm from blade centerline. This is equivalent to 36.6 mm from blade trailing edge

Distance from Inlet to Experimental Measurement:
Boundary Layer: 875.80 mm
Probe: 1710.142 mm
90% Radius: 205.74 mm

All units are in millimeters
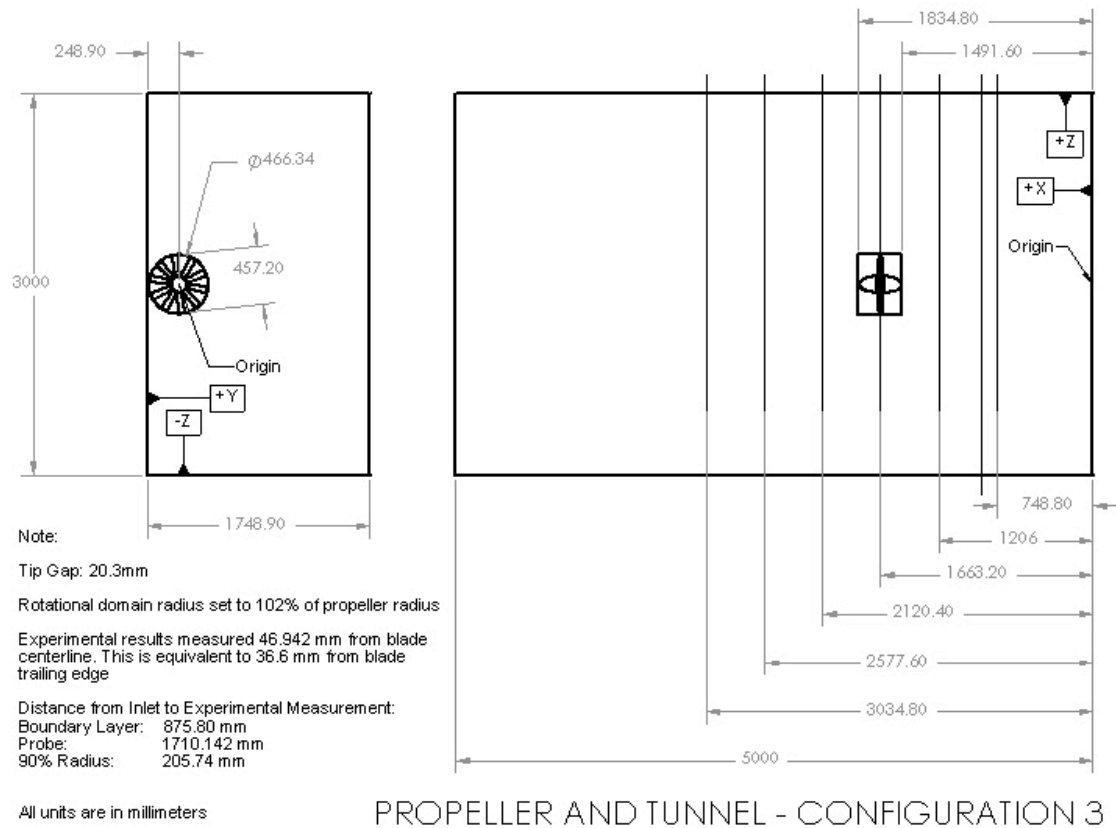
Figure 2.4 – Drawing of Configuration 3

Configuration 2 uses the same drawing of Configuration 3

(a)

(b)

(c)
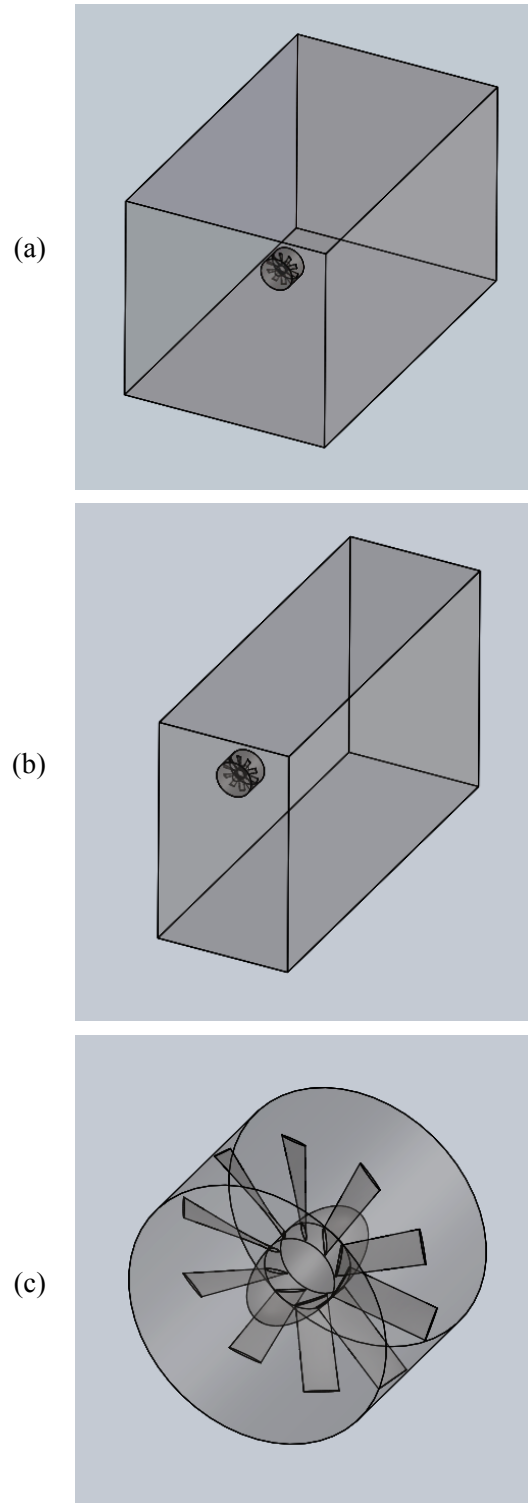
Figure 2.5 – Geometry of Domains and Subdomain

(a) Configuration 1 view of all domains
(b) Configuration 2 and 3 view of all domains
(c) Configuration 1, 2, and 3 view of rotational subdomain.

(a)

(b)

(c)
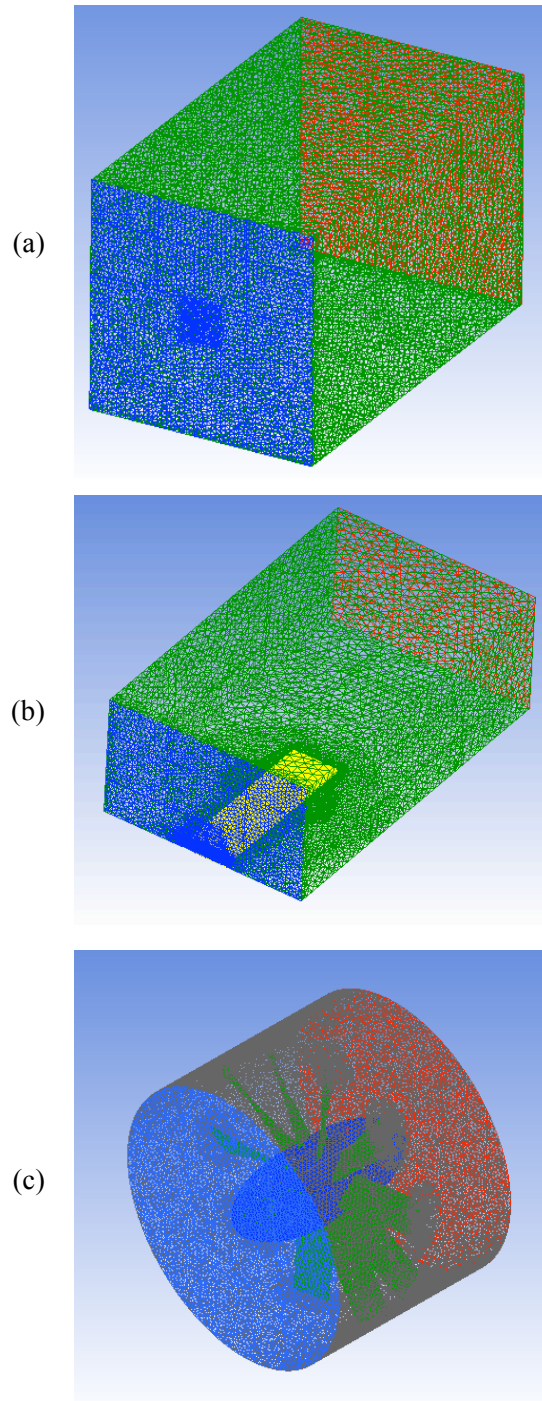
Figure 2.6 – Mesh of Domain and Subdomain

(a) Stationary Domain (Configuration 1) without rotor and rotational domain (b) Stationary Domain (Configuration 2 and 3) without rotor and rotational domain. Blue – Inlet, Red – Outlet, Yellow – Boundary layer wall, Green – Exterior walls. (c) Rotational Domain mesh including rotor. Blue – Interface in front of rotor, Red – Interface in back of rotor,

(a)

(b)

Figure 2.7 – Mesh Densities
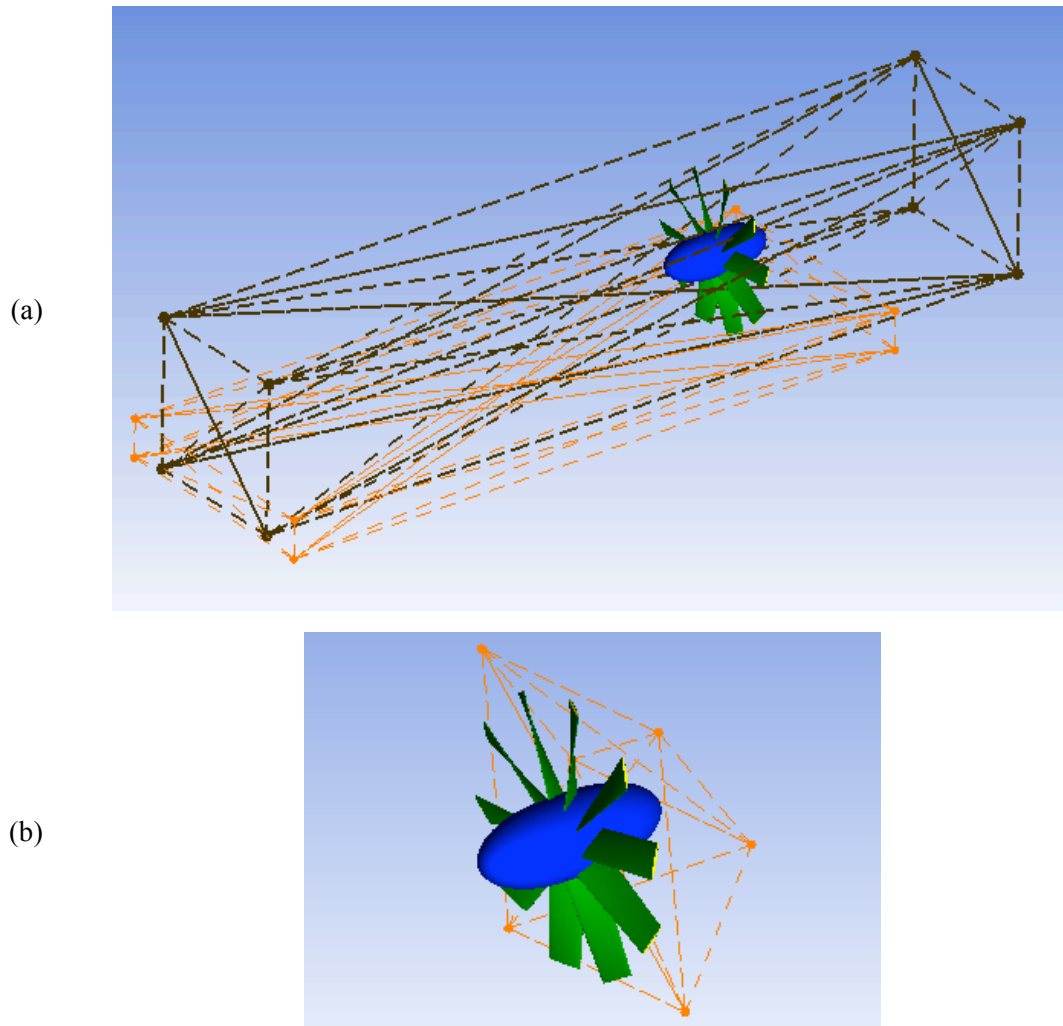
(a) Mesh Densities in Stationary and Rotational Domain.
Dark brown – Wake Density
Orange – Boundary Layer Density
(b) Mesh Density in Rotational Domain.
Orange – Experimental measurement region.
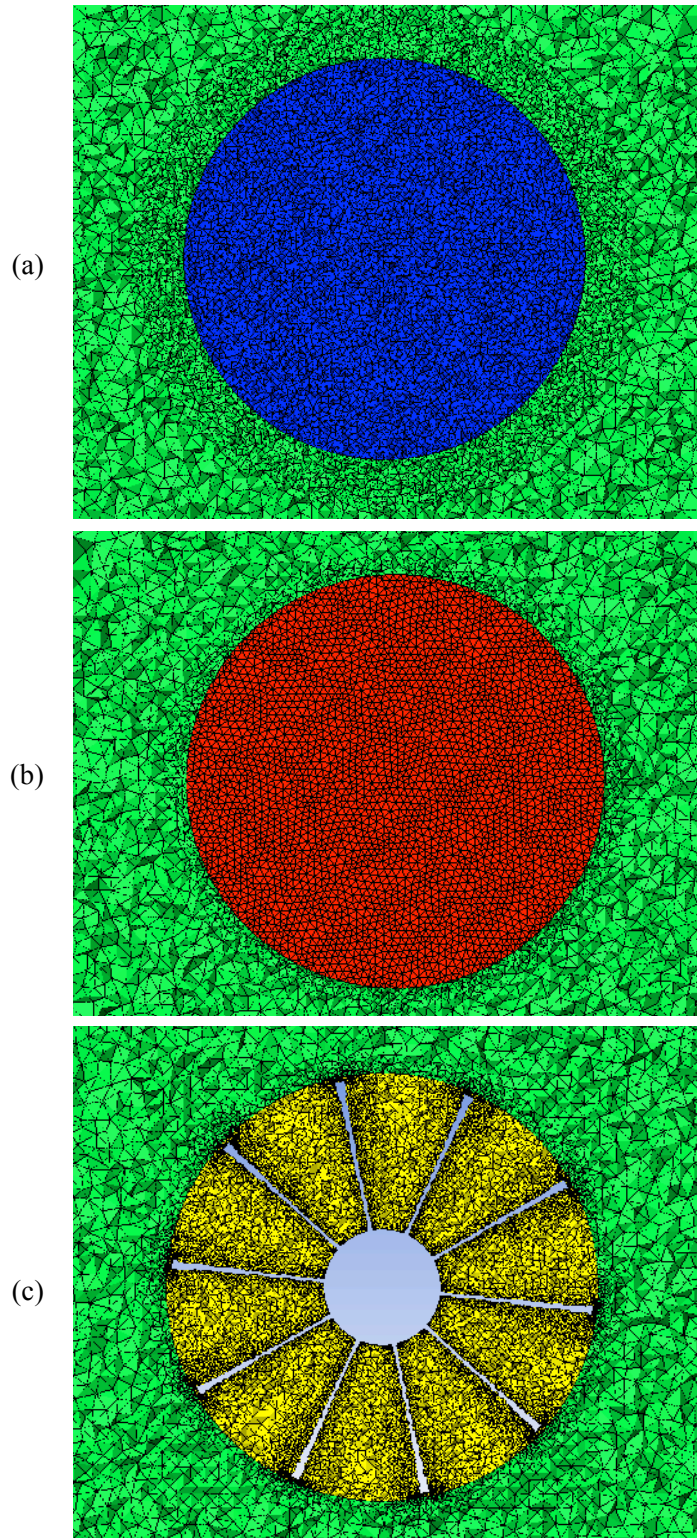
Figure 2.8 – Configuration 1 Mesh at Interfaces

(a) Front interface (blue) and surrounding stationary domain mesh (green). (b) Rear interface (red) and surrounding stationary domain mesh (green). (c) Plane at blade spanwise centerline

(a)

(b)

(c)
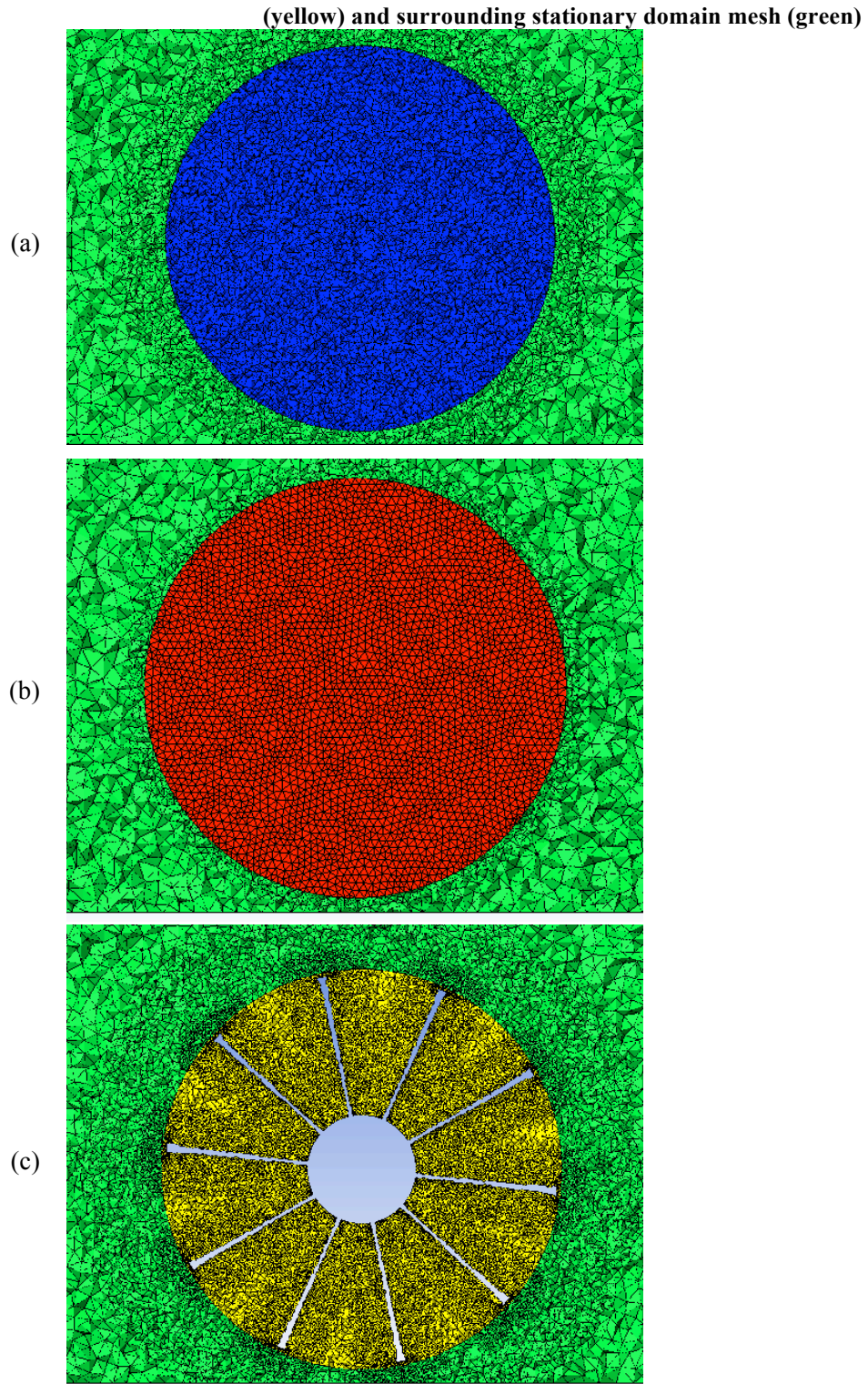
Figure 2.9 – Configuration 2 and 3 Mesh at Interfaces

(a) Front interface (blue) and surrounding stationary domain mesh (green). (b) Rear interface (red) and surrounding stationary domain mesh (green). (c) Plane at blade spanwise centerline (yellow) and surrounding stationary domain mesh (green). (a-c) is extended down to the near-wall.

(a)

(b)
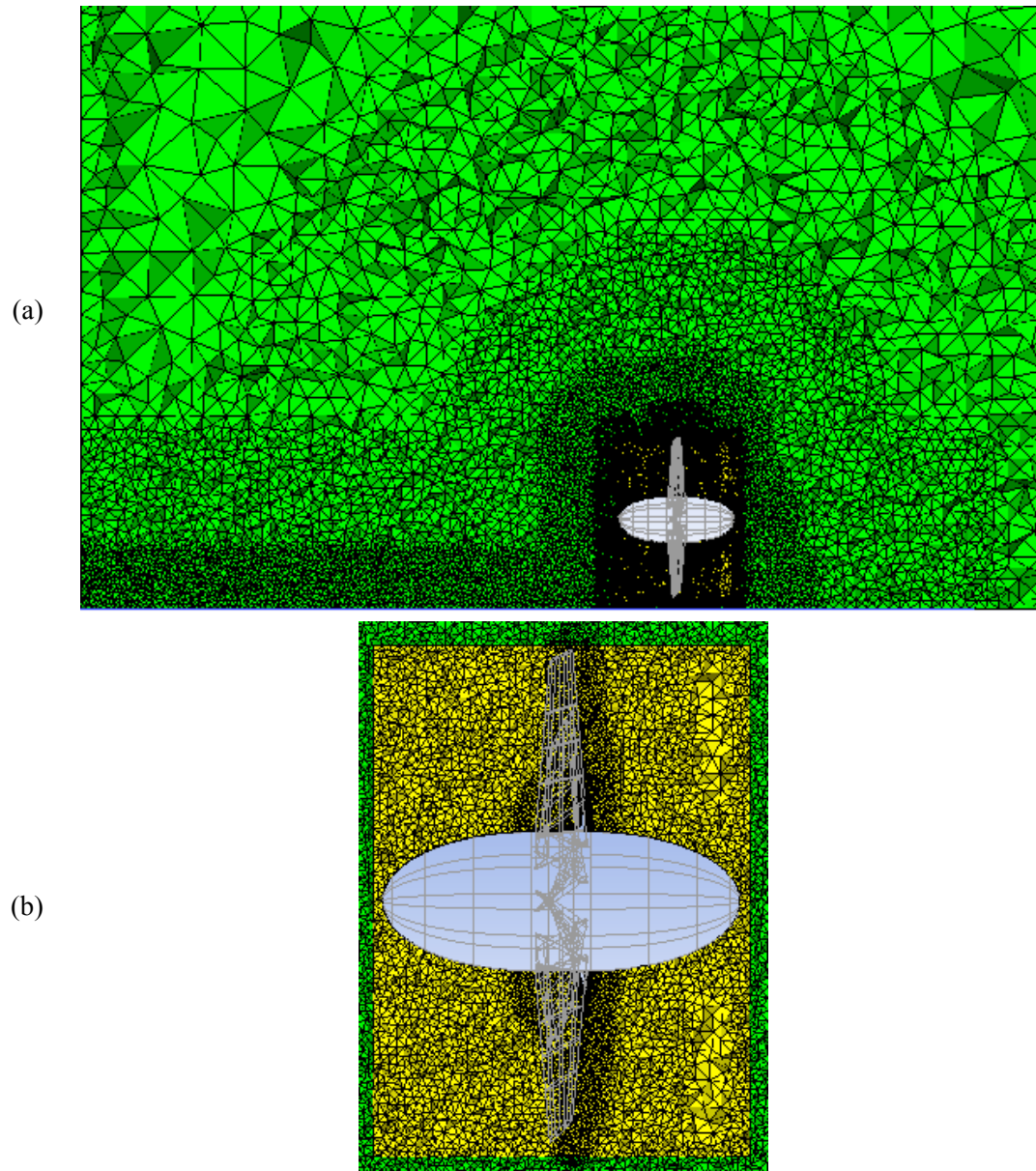
Figure 2.10 – Cross Section Display of Domain and Subdomain Mesh

(a) Stationary Domain (green) and rotational domain (yellow). Rotor is shown in grey. Shows inflation, density, and surface refinements. (b) Rotational domain mesh refinement. Inflow direction is from left to right.

(a)

(b)
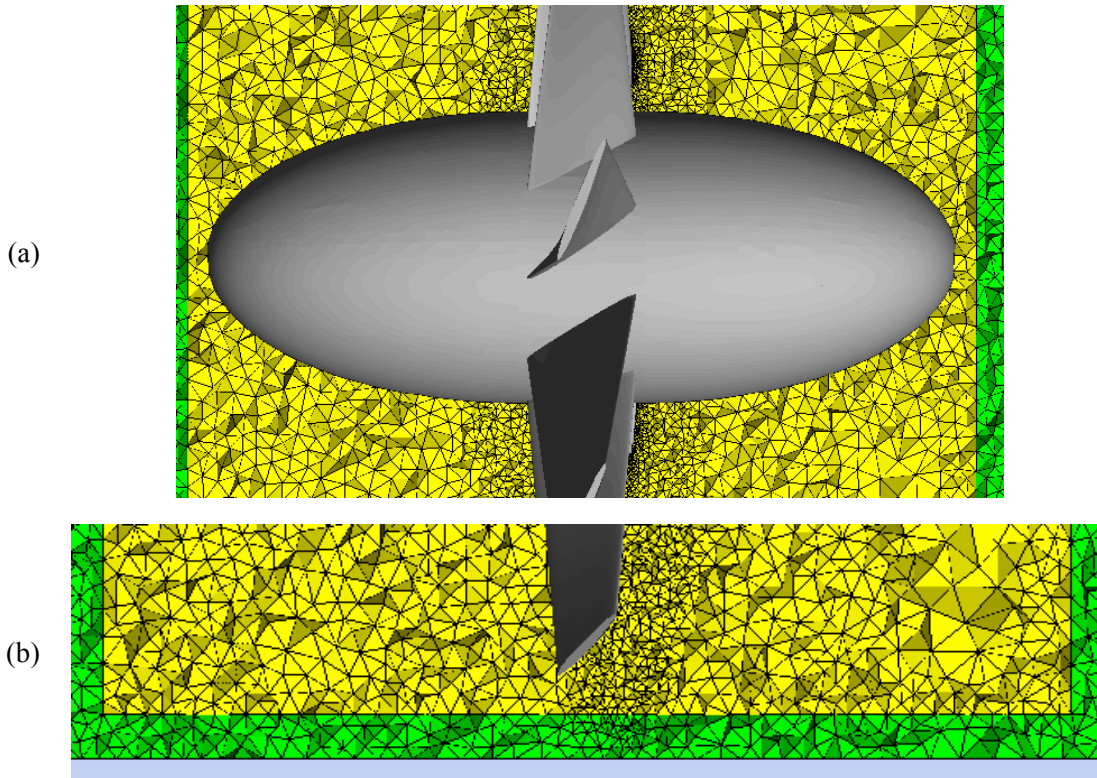
Figure 2.11 – Cross Section Display of Boundary Layer Mesh

(a) Cross section of boundary layer refinement at surface of rotor.
(b) Cross section of boundary layer refinement at near wall. Blade tip is shown in grey.
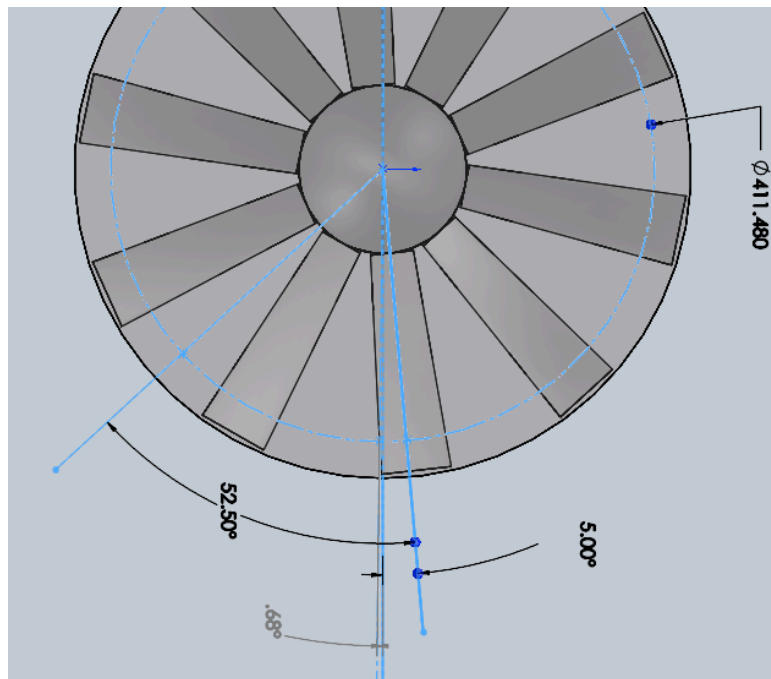
Figure 2.12 – Front View of Rotor Blade Locations (CFD)

CFD rotor position at time of CFD computation showing reference values to experimental Results
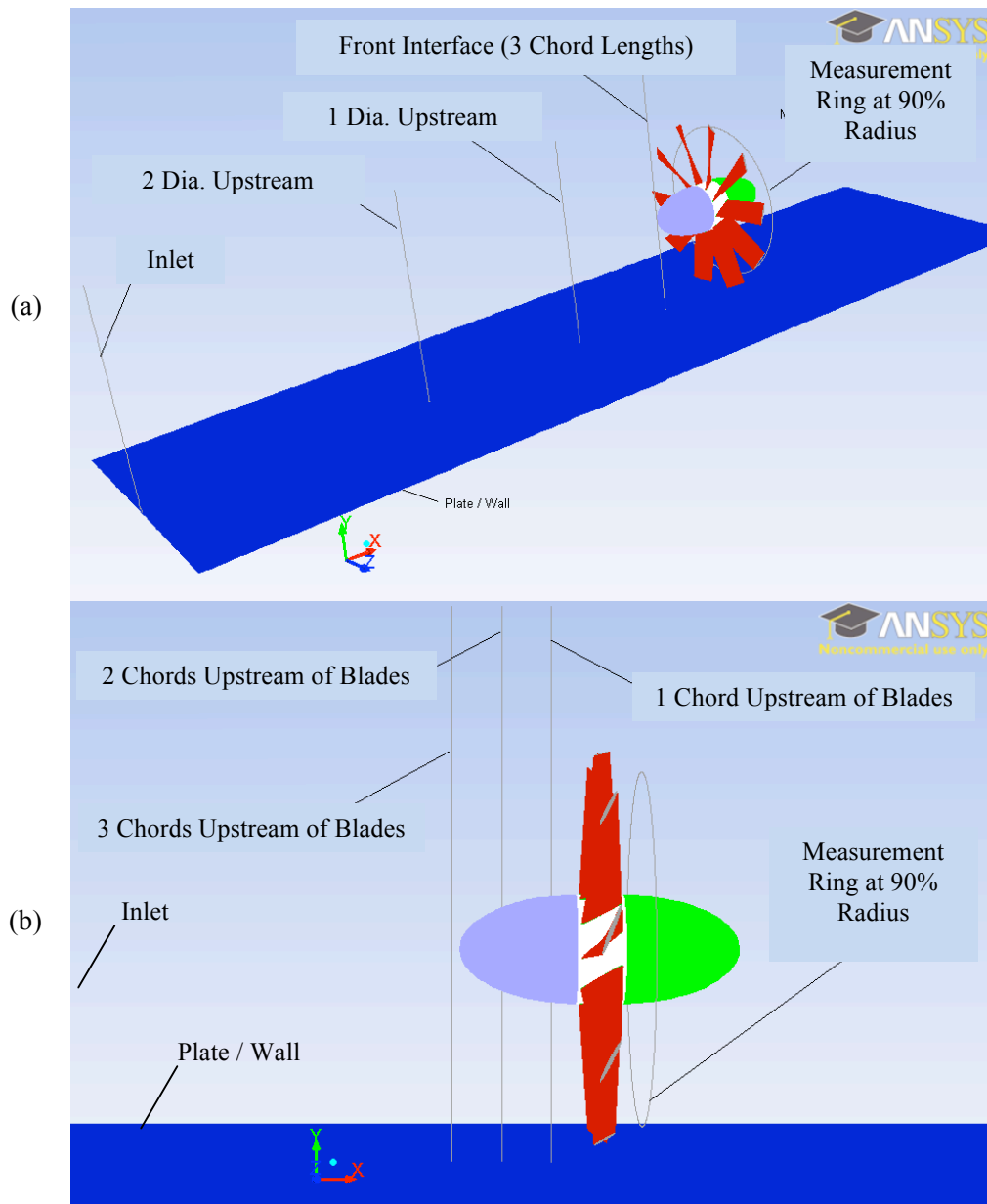
Figure 2.13 – Locations for Boundary Layer Plots

(a) Far Measurements
(b) Near Measurements
Boundary layer plots are generated over these lines. Also shown, is the 90% radius measurement ring where wake measurements are made.
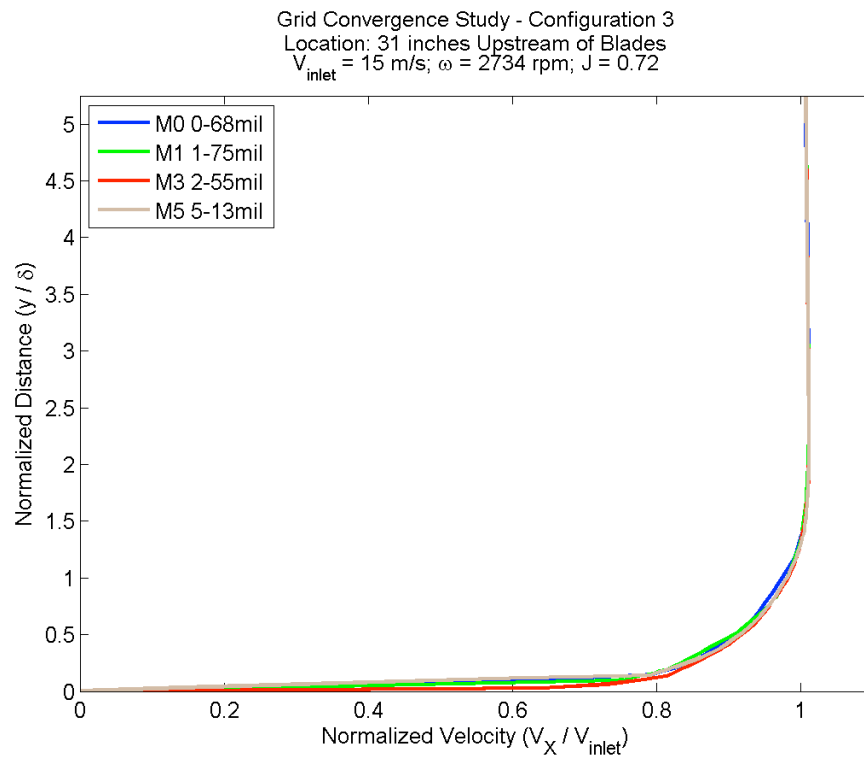
Figure 2.14 – Grid Ind. Study Results for J = 0.72 (BL)   **Configuration 3**

ACOUSTIC DATA - BOUNDARY LAYER PROFILES - FULL OPERATIONAL RANGE
LOCATION: INLET ω = 2734 rpm
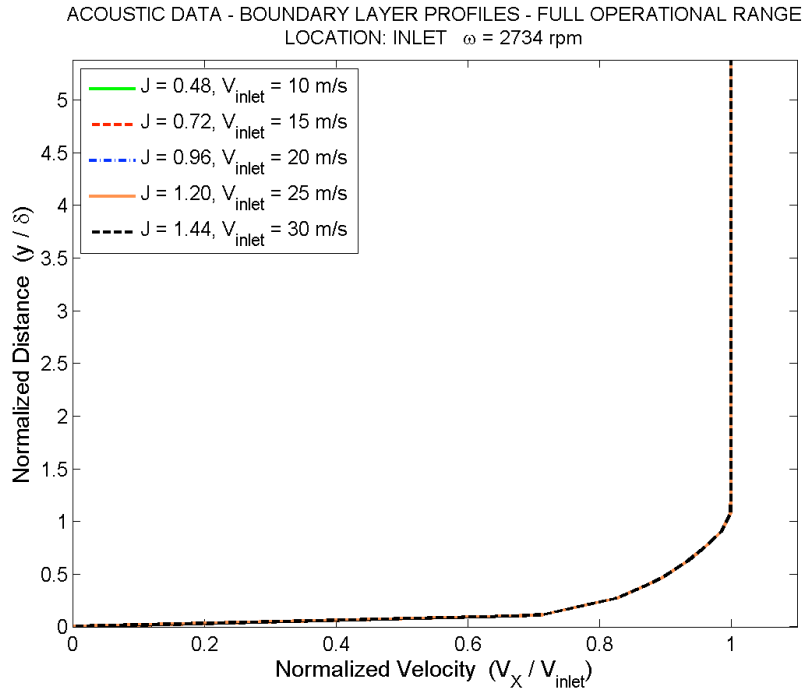
Figure 2.15 – Acoustic: BL Profile at Inlet for All Case Files

All acoustic data set cases are plotted on the same chart demonstrating the change in boundary layer profile with advance ratio.
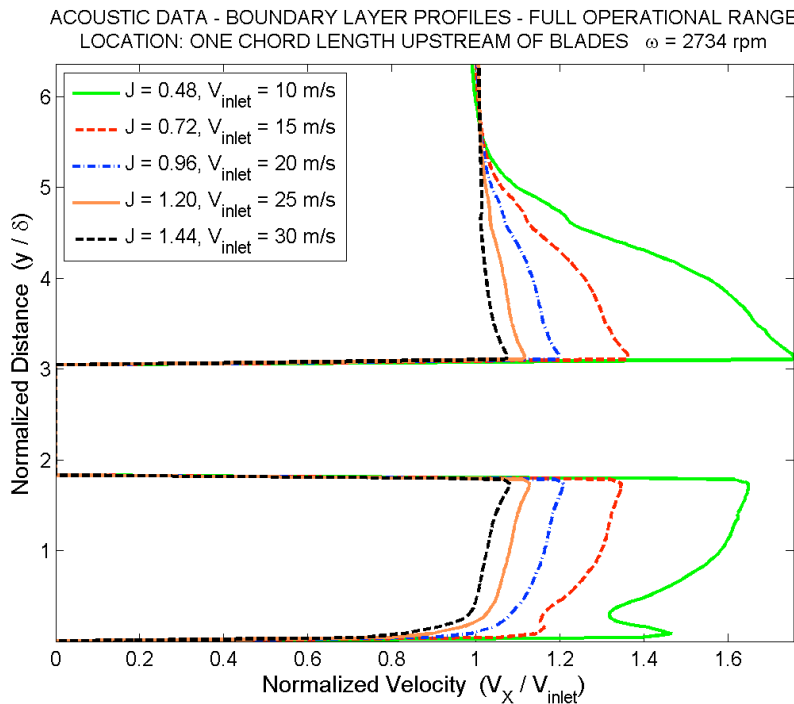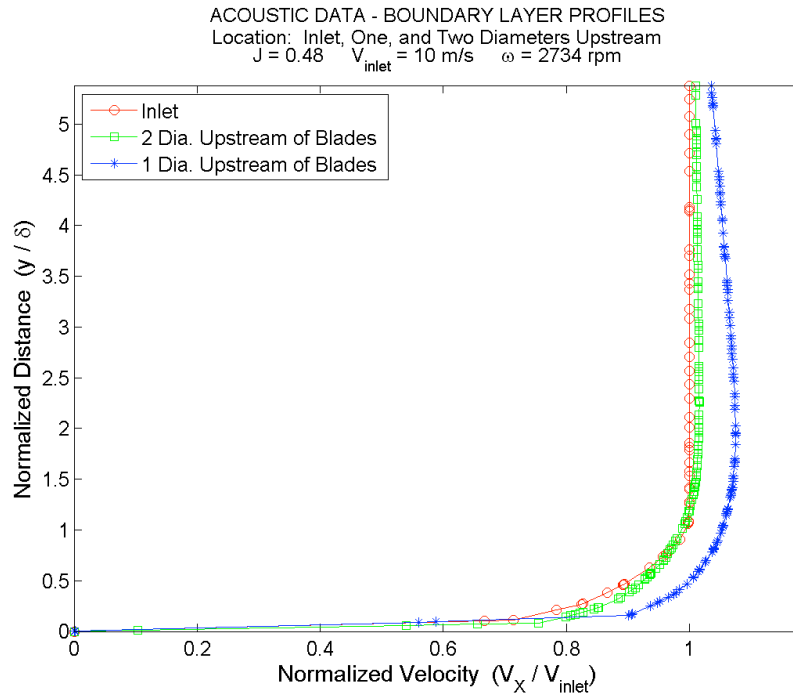
ACOUSTIC DATA - BOUNDARY LAYER PROFILES - FULL OPERATIONAL RANGE
LOCATION: TWO DIAMETERS UPSTREAM OF BLADES ω = 2734 rpm
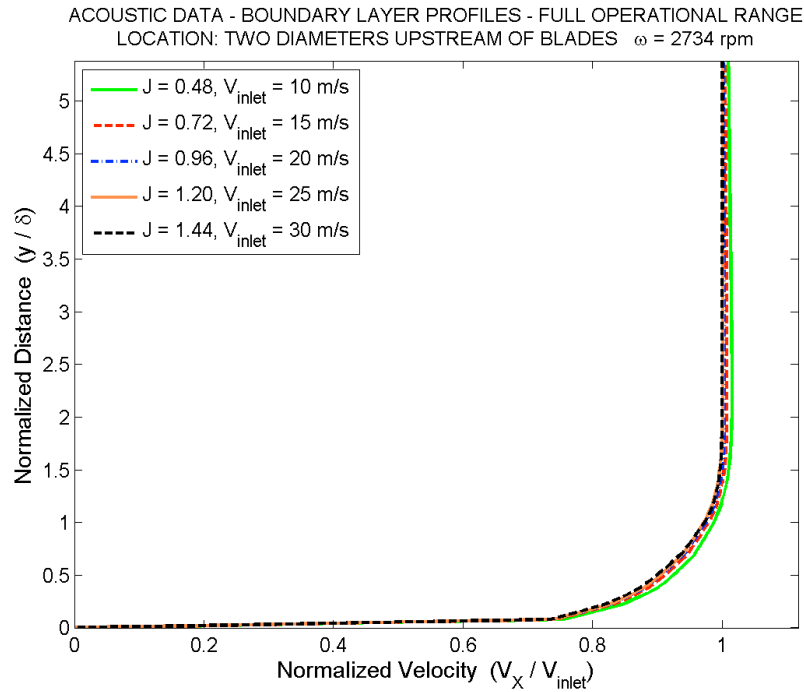
Figure 2.16 – Acoustic: BL Profile at 2 Diameters Upstream for All Case Files

All acoustic data set cases are plotted on the same chart demonstrating the change in boundary layer profile with advance ratio.

ACOUSTIC DATA - BOUNDARY LAYER PROFILES - FULL OPERATIONAL RANGE
LOCATION: ONE DIAMETER UPSTREAM OF BLADES ω = 2734 rpm
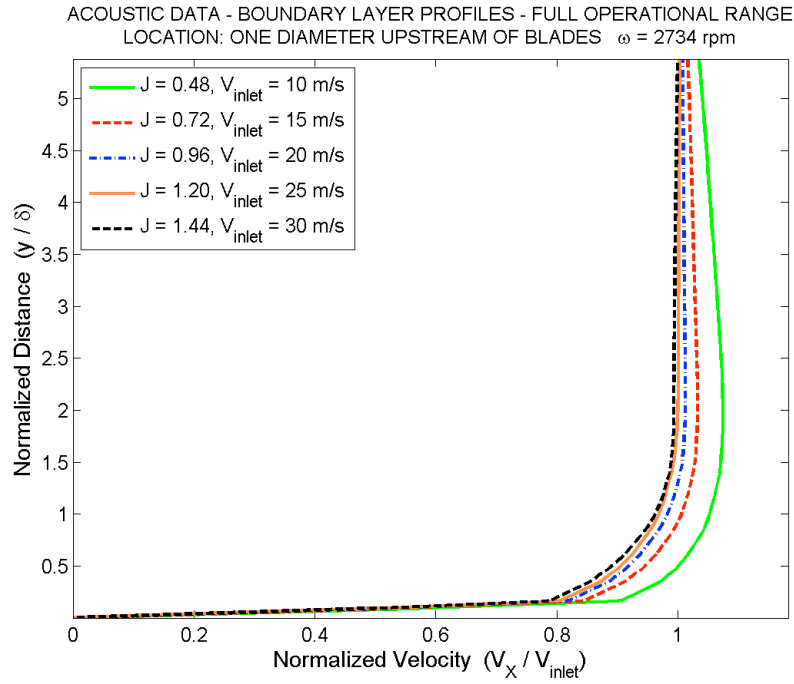
Figure 2.17 – Acoustic: BL Profile at 1 Diameter Upstream for All Case Files

All acoustic data set cases are plotted on the same chart demonstrating the change in boundary layer profile with advance ratio.

ACOUSTIC DATA - BOUNDARY LAYER PROFILES - FULL OPERATIONAL RANGE
LOCATION: THREE CHORD LENGTHS UPSTREAM OF BLADES ω = 2734 rpm
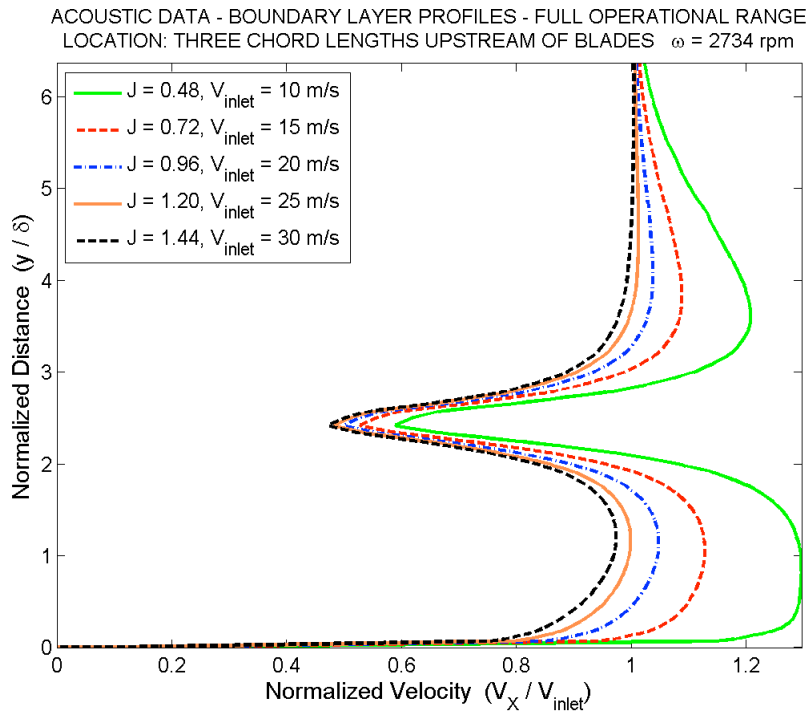
Figure 2.18 – Acoustic: BL Profile at 3 Chord Lengths Upstream for All Case Files

All acoustic data set cases are plotted on the same chart demonstrating the change in boundary layer profile with advance ratio.

100

ACOUSTIC DATA - BOUNDARY LAYER PROFILES - FULL OPERATIONAL RANGE
LOCATION: TWO CHORD LENGTHS UPSTREAM OF BLADES   ω = 2734 rpm
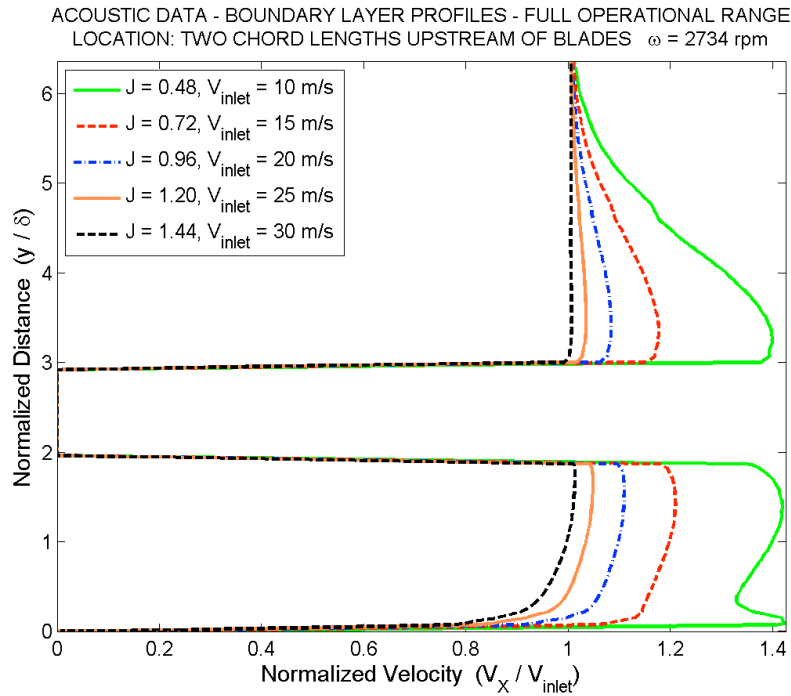
Figure 2.19– Acoustic: BL Profile at 2 Chord Lengths Upstream for All Case Files

All acoustic data set cases are plotted on the same chart demonstrating the change in boundary layer profile with advance ratio.

ACOUSTIC DATA - BOUNDARY LAYER PROFILES - FULL OPERATIONAL RANGE
LOCATION: ONE CHORD LENGTH UPSTREAM OF BLADES   ω = 2734 rpm

Figure 2.20– Acoustic: BL Profile at 1 Chord Length Upstream for All Case Files

All acoustic data set cases are plotted on the same chart demonstrating the change in boundary layer profile with advance ratio.

101

ACOUSTIC DATA - BOUNDARY LAYER PROFILES
Location: Inlet, One, and Two Diameters Upstream
J = 0.48 V_{inlet} = 10 m/s   ω = 2734 rpm

Figure 2.21 – Acoustic: BL Profile at All Far Upstream Stations (J = 0.48)

Configuration 3 Case for J = 0.48 Boundary layer profiles at all far upstream stations demonstrating the change in boundary layer profile with location.
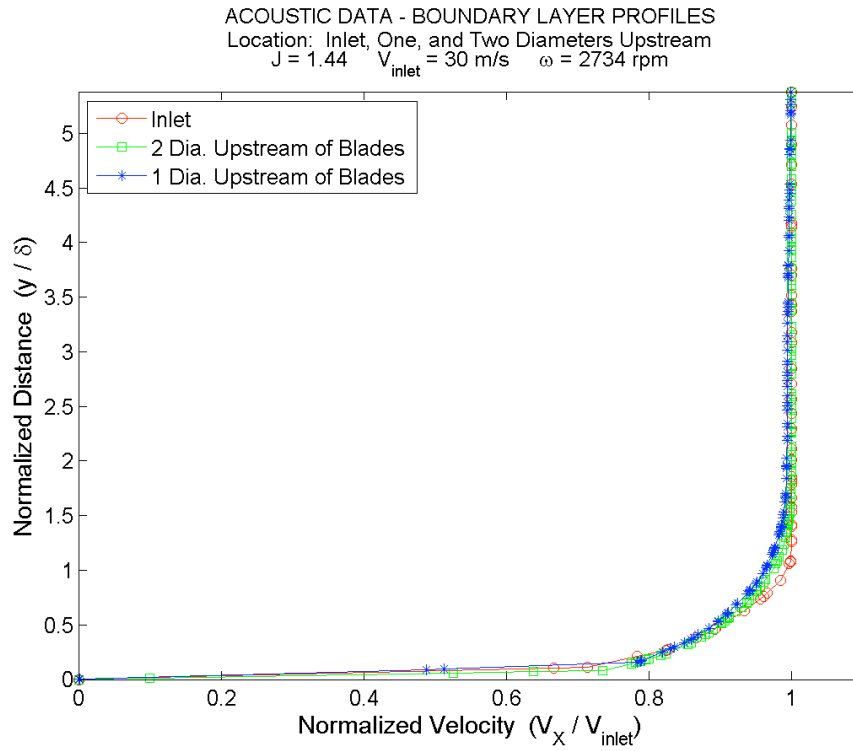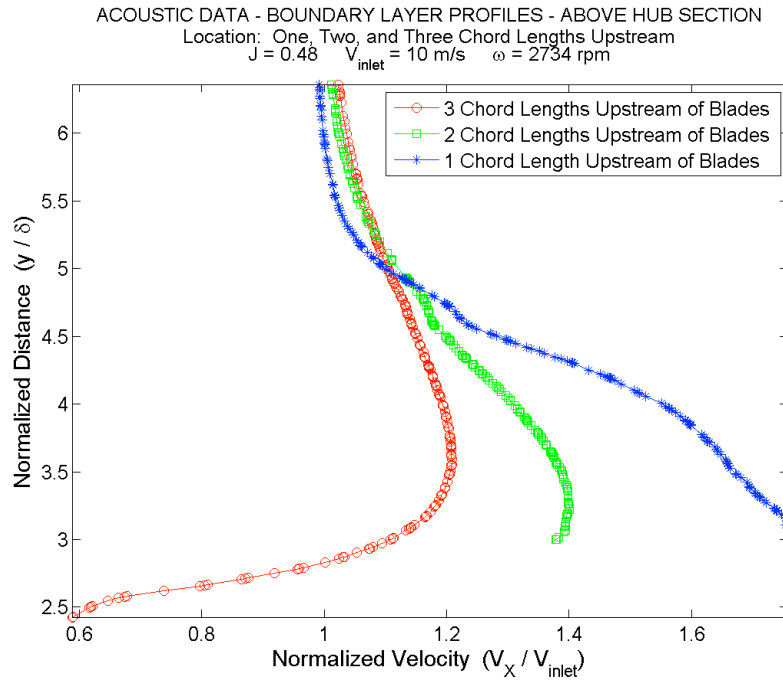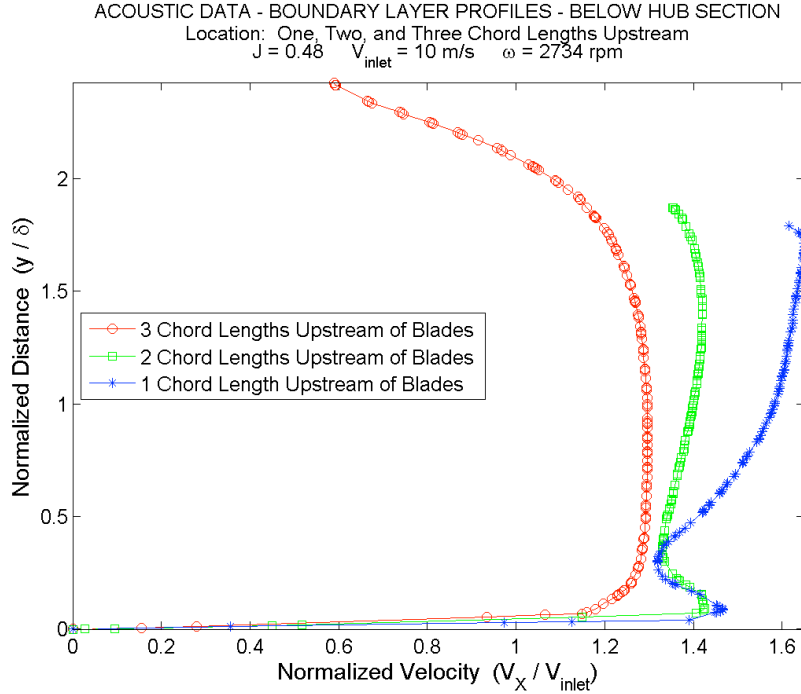
ACOUSTIC DATA - BOUNDARY LAYER PROFILES
Location: Inlet, One, and Two Diameters Upstream
J = 0.72 V_{inlet} = 15 m/s   ω = 2734 rpm
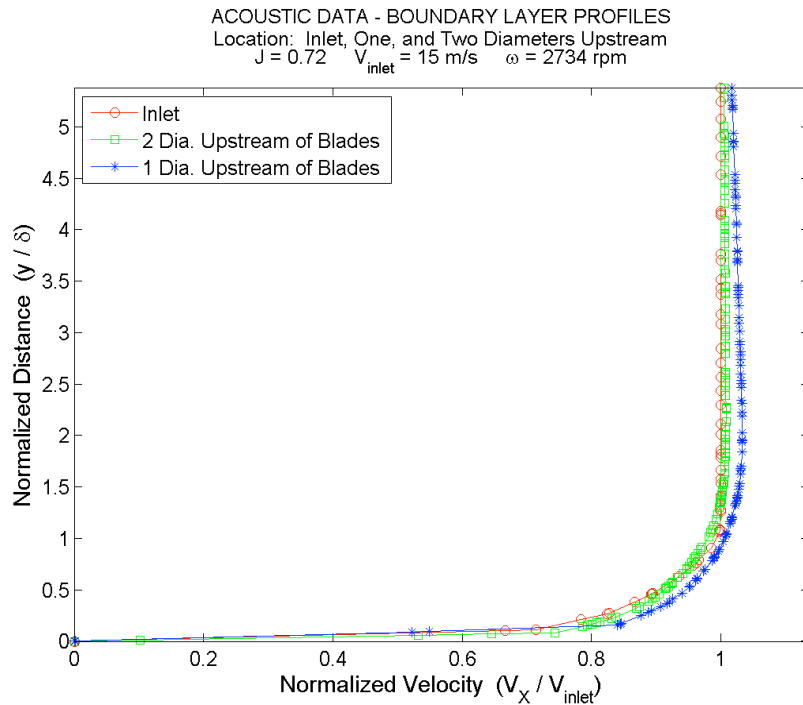
Figure 2.22 – Acoustic: BL Profile at All Far Upstream Stations (J = 0.72)

Configuration 3 Case for J = 0.72 Boundary layer profiles at all far upstream stations demonstrating the change in boundary layer profile with location.

ACOUSTIC DATA - BOUNDARY LAYER PROFILES
Location: Inlet, One, and Two Diameters Upstream
J = 0.96   V$_{inlet}$ = 20 m/s   ω = 2734 rpm
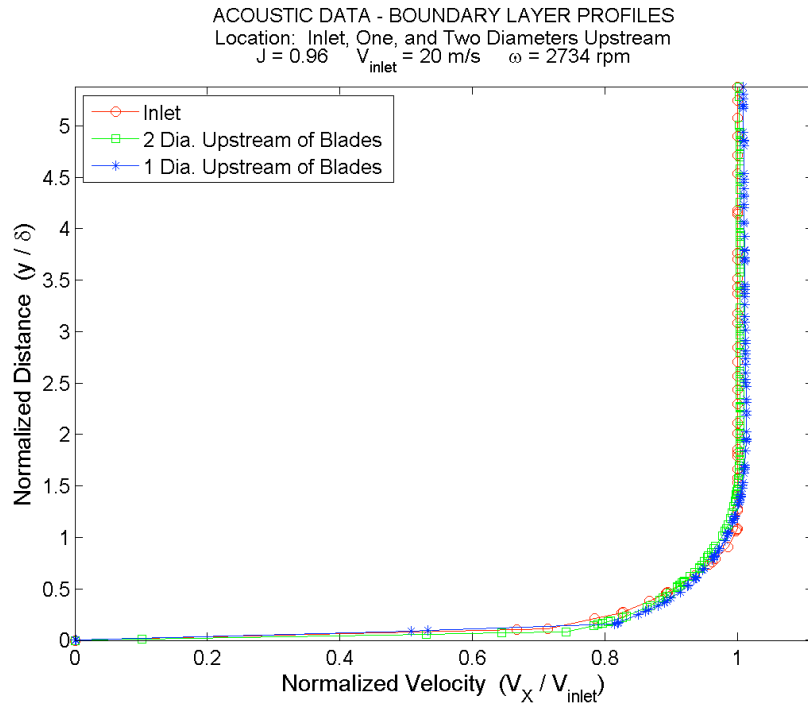
Figure 2.23 – Acoustic: BL Profile at All Far Upstream Stations (J = 0.96)

Configuration 3 Case for J = 0.96 Boundary layer profiles at all far upstream stations demonstrating the change in boundary layer profile with location.
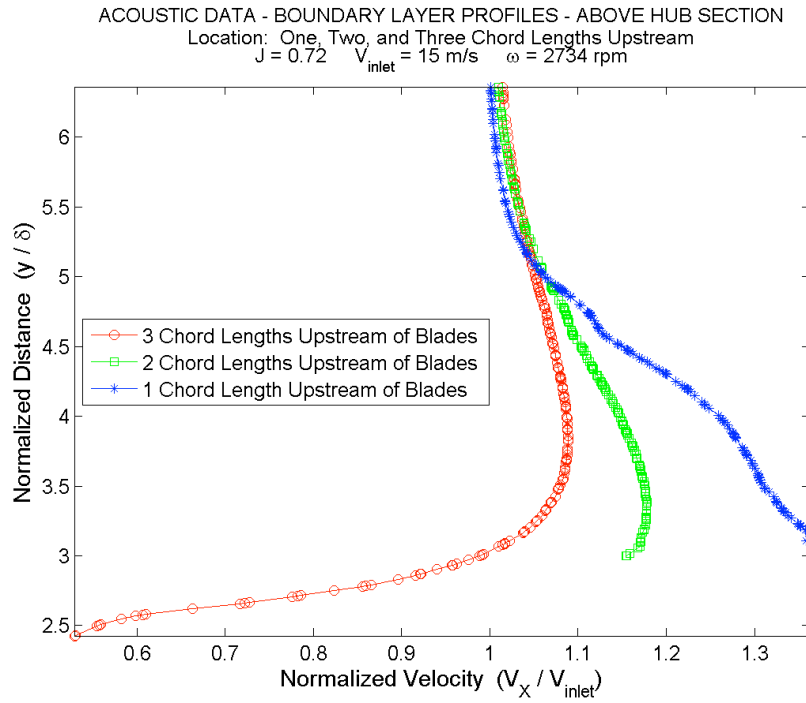

ACOUSTIC DATA - BOUNDARY LAYER PROFILES
Location: Inlet, One, and Two Diameters Upstream
J = 1.2   V$_{inlet}$ = 25 m/s   ω = 2734 rpm
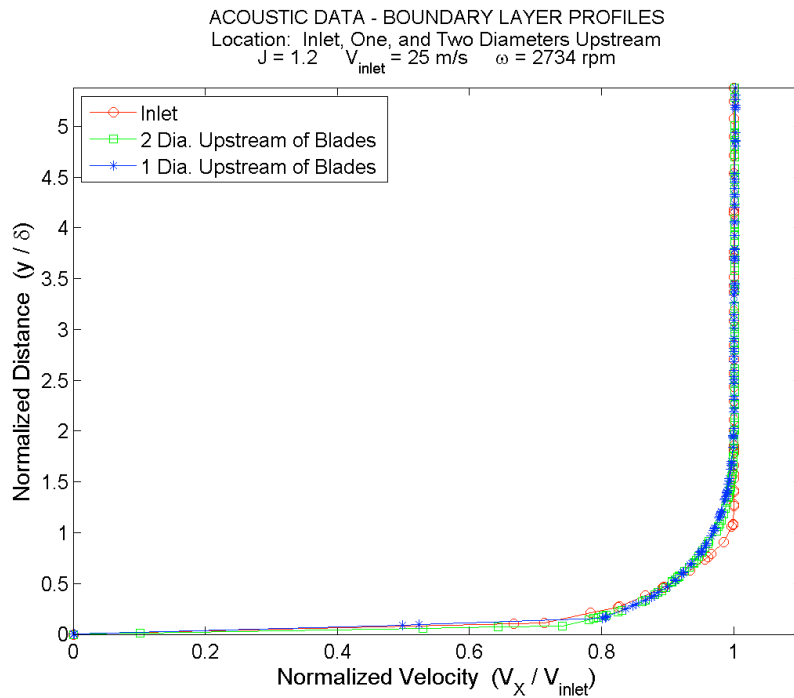
Figure 2.24 – Acoustic: BL Profile at All Far Upstream Stations (J = 1.20)

Configuration 3 Case for J = 1.20 Boundary layer profiles at all far upstream stations demonstrating the change in boundary layer profile with location.

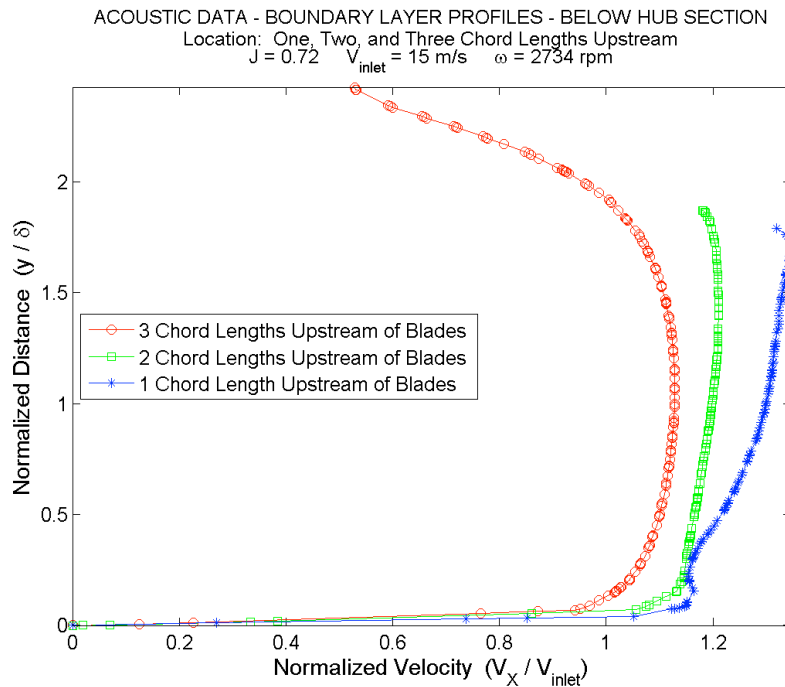ACOUSTIC DATA - BOUNDARY LAYER PROFILES
Location: Inlet, One, and Two Diameters Upstream
$J = 1.44$ $V_{inlet} = 30$ m/s $\omega = 2734$ rpm

**Figure 2.25– Acoustic: BL Profile at
All Far Upstream Stations (J = 1.44)**

**Configuration 3 Case for J = 1.44
Boundary layer profiles at all far upstream
stations demonstrating the change in
boundary layer profile with location.**

ACOUSTIC DATA - BOUNDARY LAYER PROFILES - ABOVE HUB SECTION
Location: One, Two, and Three Chord Lengths Upstream
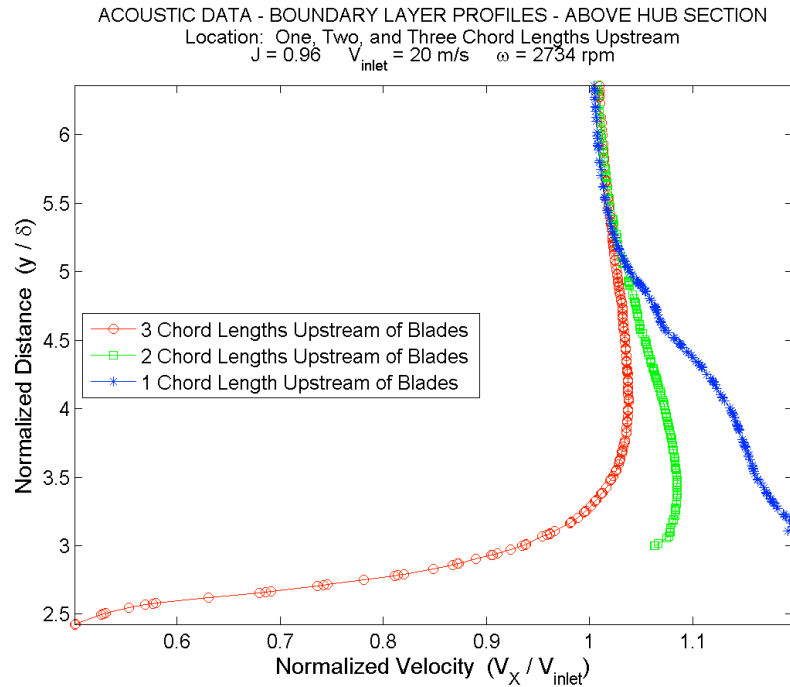J = 0.48   V_inlet = 10 m/s   ω = 2734 rpm

Figure 2.26 – Acoustic: BL Profile at All Near Upstream Stations (J = 0.48 – AH)

Configuration 3 Case for J = 0.48 Boundary layer profiles at all near upstream stations above hub demonstrating the change in boundary layer profile with location.
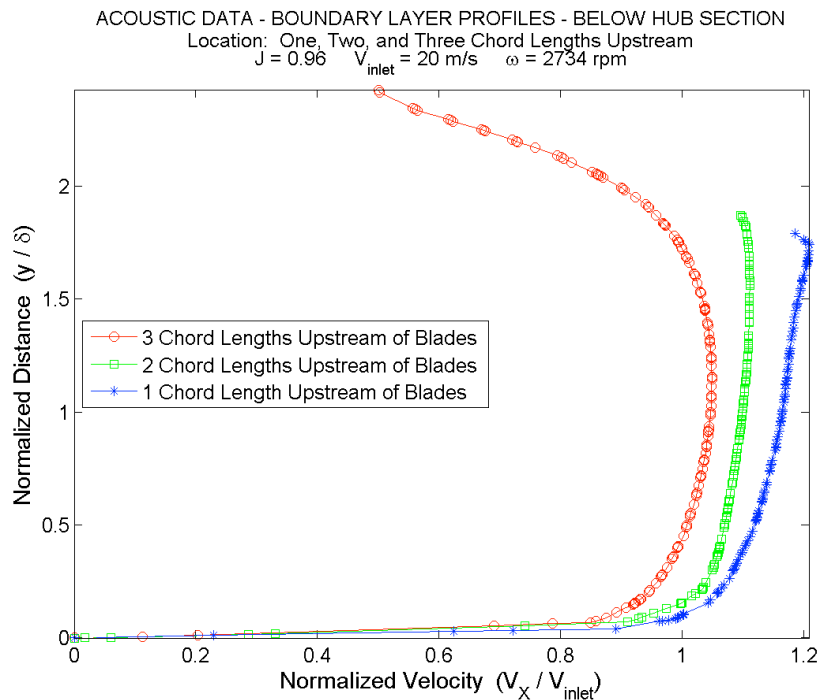
ACOUSTIC DATA - BOUNDARY LAYER PROFILES - BELOW HUB SECTION
Location: One, Two, and Three Chord Lengths Upstream
J = 0.48   V_inlet = 10 m/s   ω = 2734 rpm

Figure 2.27 – Acoustic: BL Profile at All Near Upstream Stations (J = 0.48 – BH)

Configuration 3 Case for J = 0.48 Boundary layer profiles at all near upstream stations below hub demonstrating the change in boundary layer profile with location.
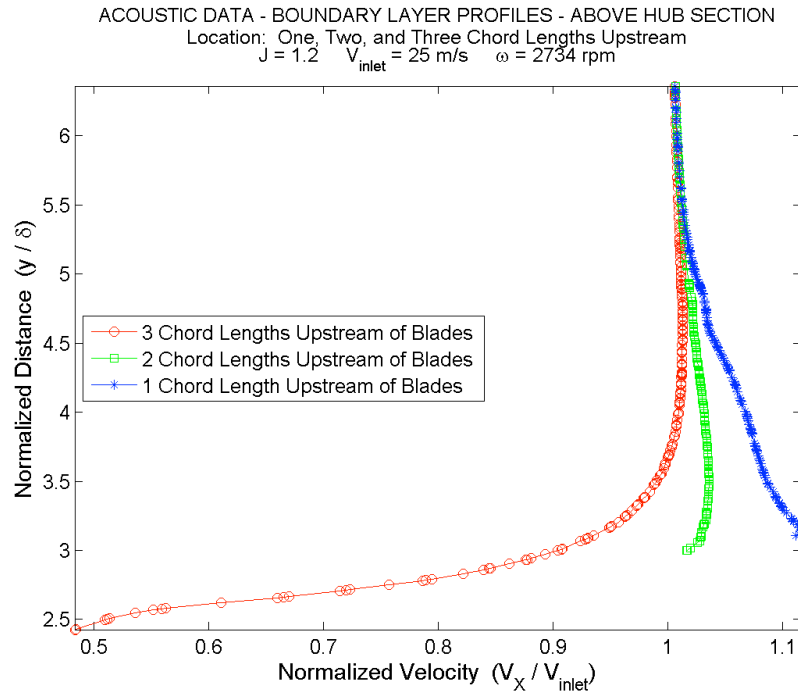
105

ACOUSTIC DATA - BOUNDARY LAYER PROFILES - ABOVE HUB SECTION
Location: One, Two, and Three Chord Lengths Upstream
$J = 0.72$ $V_{inlet} = 15$ m/s $\omega = 2734$ rpm

Figure 2.28– Acoustic: BL Profile at All Near Upstream Stations (J = 0.72 – AH)

Configuration 3 Case for J = 0.72
Boundary layer profiles at all near upstream stations above hub demonstrating the change in boundary layer profile with location.
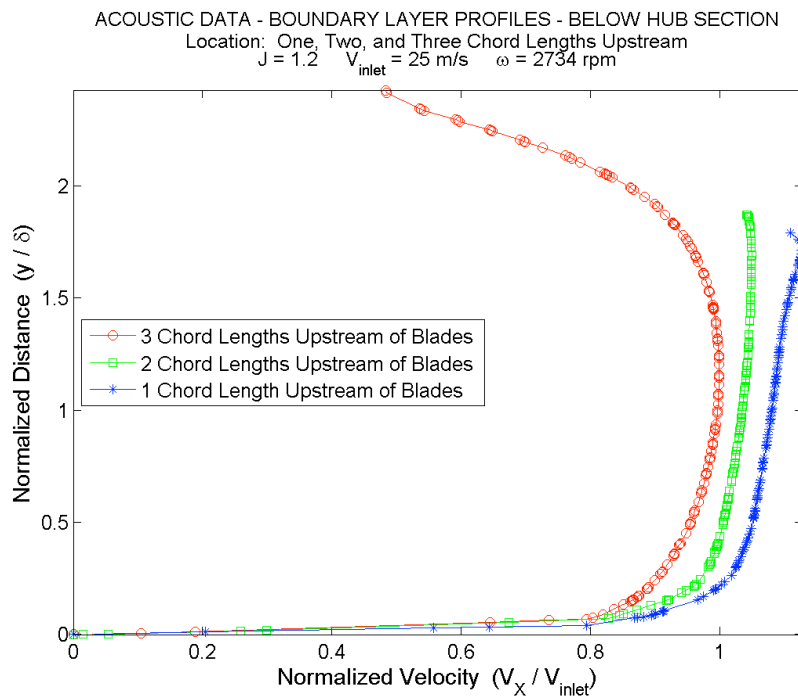

ACOUSTIC DATA - BOUNDARY LAYER PROFILES - BELOW HUB SECTION
Location: One, Two, and Three Chord Lengths Upstream
$J = 0.72$ $V_{inlet} = 15$ m/s $\omega = 2734$ rpm

Figure 2.29 – Acoustic: BL Profile at All Near Upstream Stations (J = 0.72 – BH)

Configuration 3 Case for J = 0.72
Boundary layer profiles at all near upstream stations below hub demonstrating the change in boundary layer profile with location.
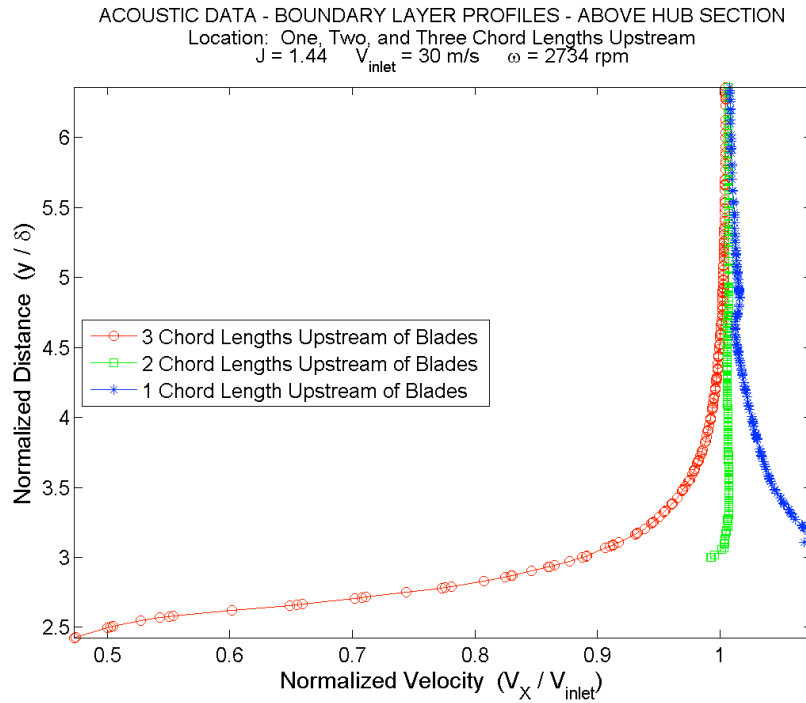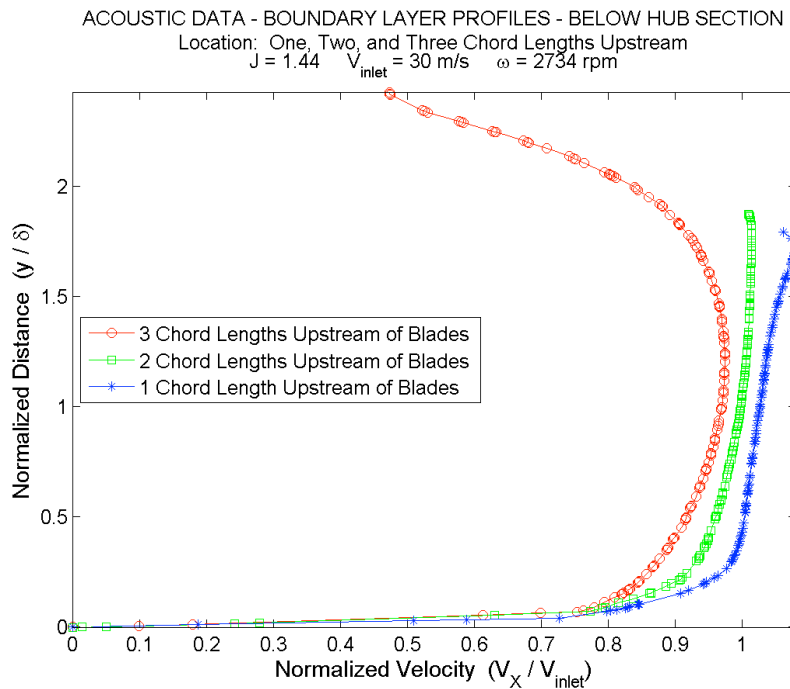
ACOUSTIC DATA - BOUNDARY LAYER PROFILES - ABOVE HUB SECTION
Location: One, Two, and Three Chord Lengths Upstream
J = 0.96 V_{inlet} = 20 m/s ω = 2734 rpm

Figure 2.30 – Acoustic: BL Profile at All Near Upstream Stations (J = 0.96 – AH)

Configuration 3 Case for J = 0.96 Boundary layer profiles at all near upstream stations above hub demonstrating the change in boundary layer profile with location.
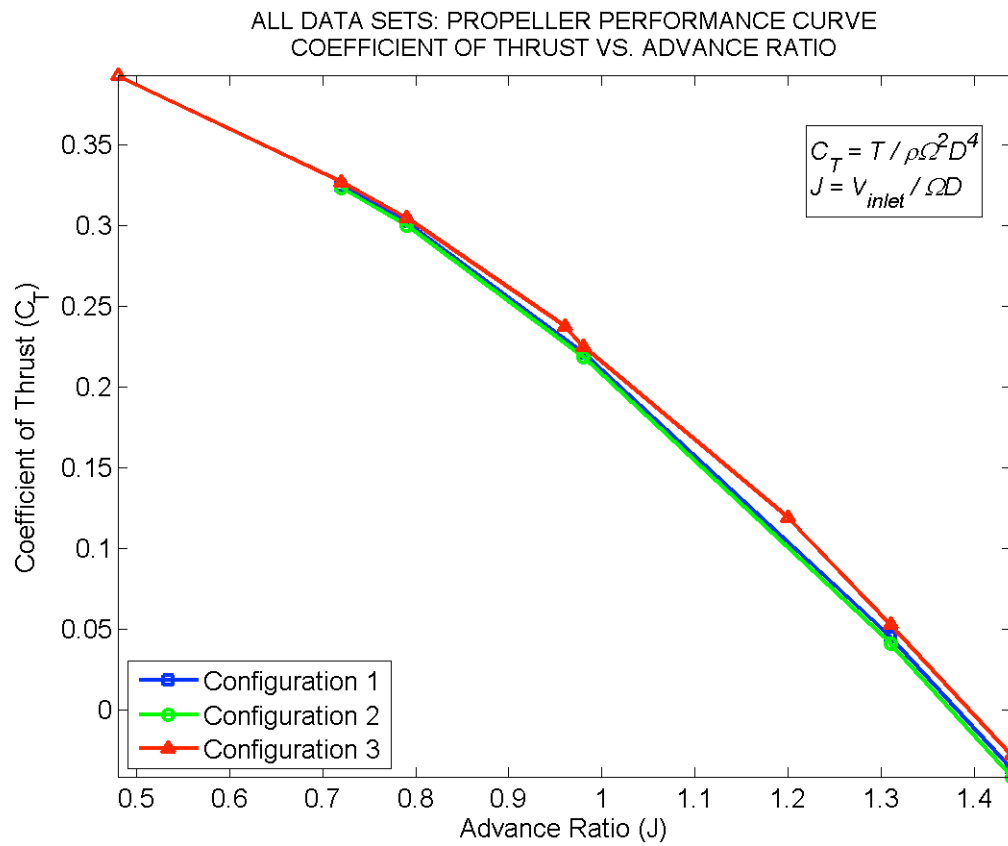

ACOUSTIC DATA - BOUNDARY LAYER PROFILES - BELOW HUB SECTION
Location: One, Two, and Three Chord Lengths Upstream
J = 0.96 V_{inlet} = 20 m/s ω = 2734 rpm

Figure 2.31 – Acoustic: BL Profile at All Near Upstream Stations (J = 0.96 – BH)

Configuration 3 Case for J = 0.96 Boundary layer profiles at all near upstream stations below hub demonstrating the change in boundary layer profile with location.

ACOUSTIC DATA - BOUNDARY LAYER PROFILES - ABOVE HUB SECTION
Location: One, Two, and Three Chord Lengths Upstream
$J = 1.2$ $V_{inlet} = 25$ m/s $\omega = 2734$ rpm

Figure 2.32– Acoustic: BL Profile at All Near Upstream Stations (J = 1.20 – AH)

Configuration 3 Case for J = 1.20
Boundary layer profiles at all near upstream stations above hub demonstrating the change in boundary layer profile with location.

ACOUSTIC DATA - BOUNDARY LAYER PROFILES - BELOW HUB SECTION
Location: One, Two, and Three Chord Lengths Upstream
$J = 1.2$ $V_{inlet} = 25$ m/s $\omega = 2734$ rpm

Figure 2.33 – Acoustic: BL Profile at All Near Upstream Stations (J = 1.20 – BH)

Configuration 3 Case for J = 1.20
Boundary layer profiles at all near upstream stations below hub demonstrating the change in boundary layer profile with location.

108

ACOUSTIC DATA - BOUNDARY LAYER PROFILES - ABOVE HUB SECTION
Location: One, Two, and Three Chord Lengths Upstream
J = 1.44 V_{inlet} = 30 m/s ω = 2734 rpm

Figure 2.34 – Acoustic: BL Profile at All Near Upstream Stations (J = 1.44 – AH)

Configuration 3 Case for J = 1.44 Boundary layer profiles at all near upstream stations above hub demonstrating the change in boundary layer profile with location.

ACOUSTIC DATA - BOUNDARY LAYER PROFILES - BELOW HUB SECTION
Location: One, Two, and Three Chord Lengths Upstream
J = 1.44 V_{inlet} = 30 m/s ω = 2734 rpm

Figure 2.35 – Acoustic: BL Profile at All Near Upstream Stations (J = 1.44 – BH)

Configuration 3 Case for J = 1.44 Boundary layer profiles at all near upstream stations below hub demonstrating the change in boundary layer profile with location.

109

ALL DATA SETS: PROPELLER PERFORMANCE CURVE
COEFFICIENT OF THRUST VS. ADVANCE RATIO

$$C_T = T / \rho\Omega^2 D^4$$
$$J = V_{inlet} / \Omega D$$

Figure 2.36 – Coefficient of Thrust vs. Advance Ratio

**All configurations and all data sets.
Acoustic data set is represented with
configuration 3.**
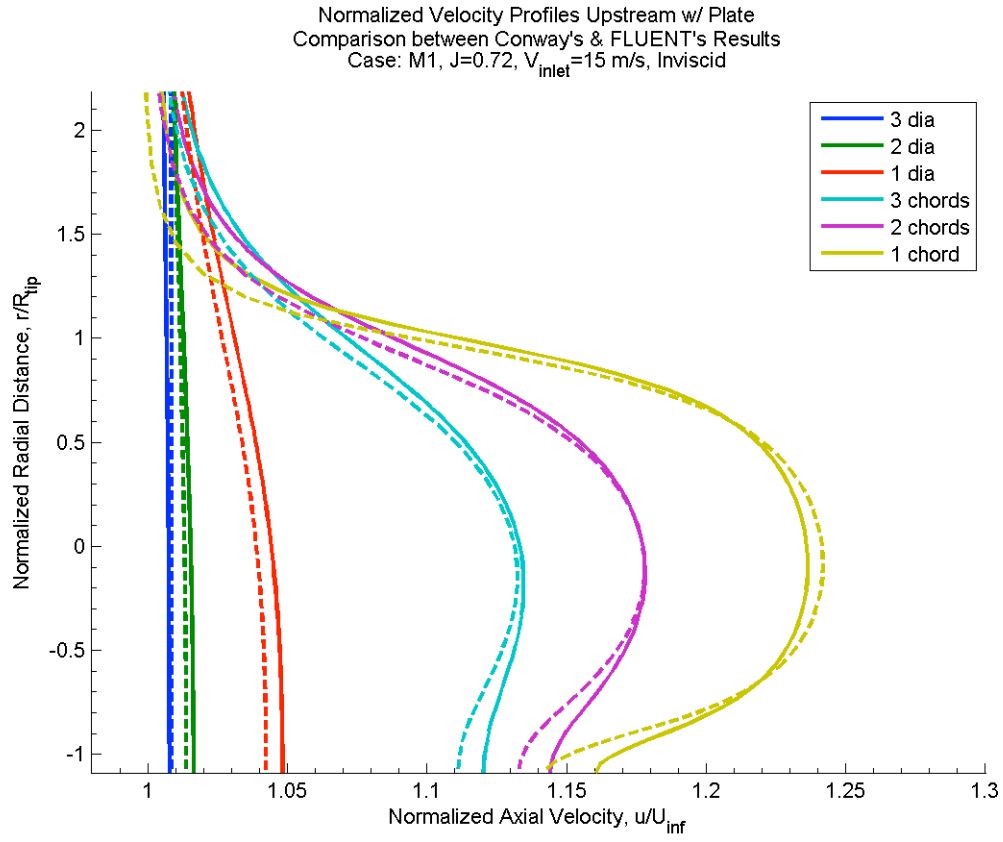
Figure 3.1: The flow entering the rotor near a wall based on Conway's potential flow model (solid line) and an inviscid RANS calculation using an actuator disc for an Advance ratio of *J=0.72*.
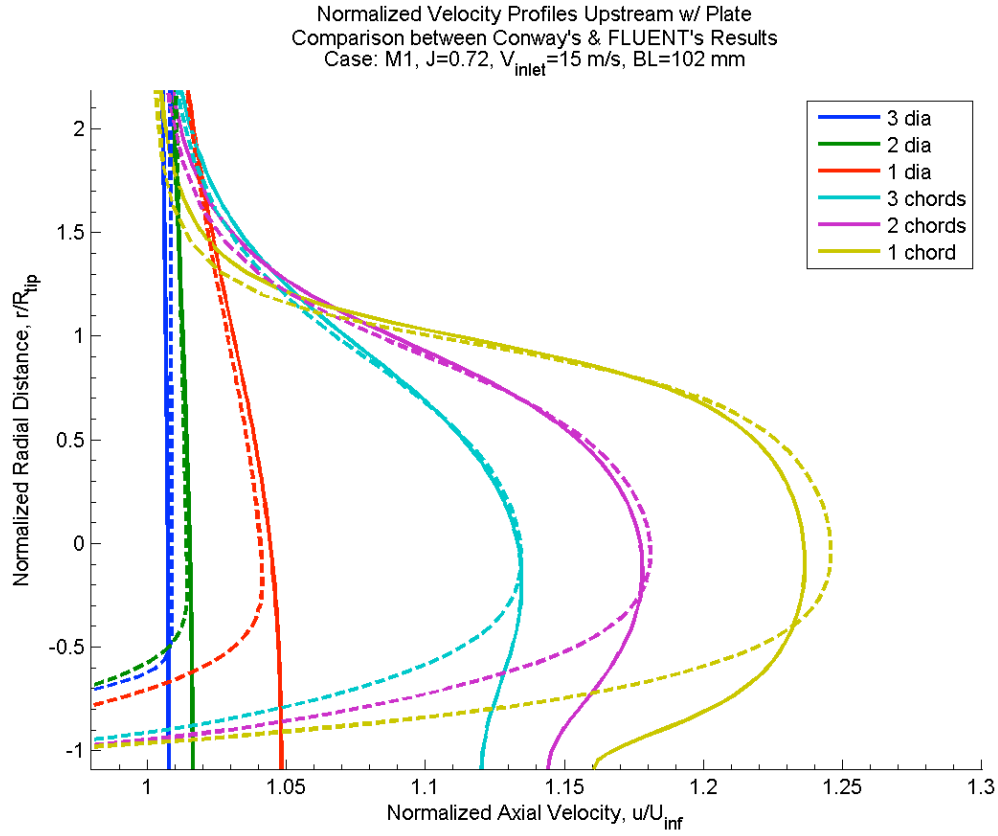
Figure 3.2: The flow entering the rotor near a wall based on Conway's potential flow model (solid line) and a viscid RANS calculation using an actuator disc for an Advance ratio of *J=0.72*.
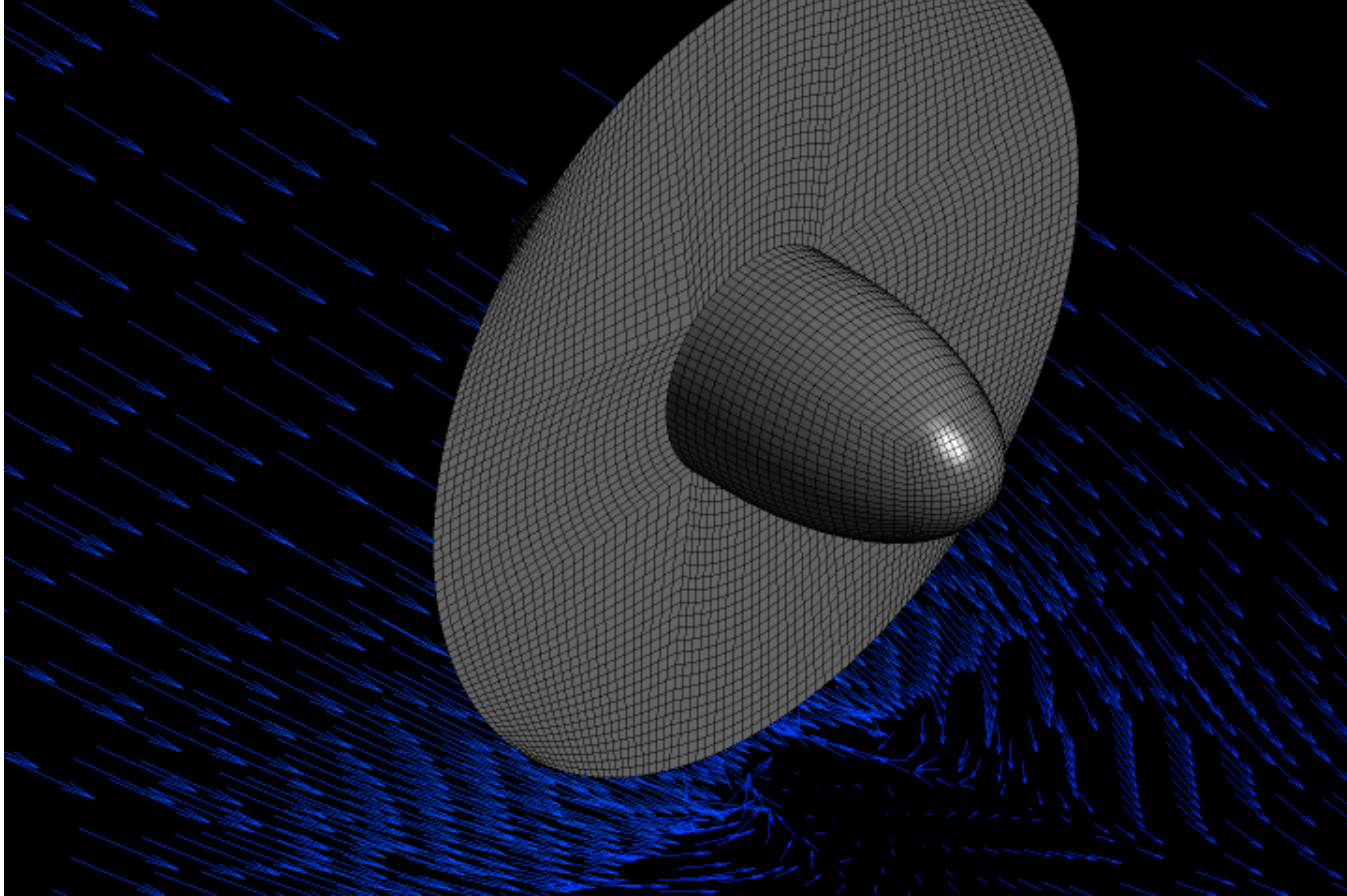
Figure 3.3: The actuator disc model grid and the flow 1mm above the plate at *J=0.48*. Note the reverse flow effect.

Rotor

Wind Tunnel Wall

Flow separation and reverse flow near the wall will impact the radiated noise and unsteady loading of the rotor
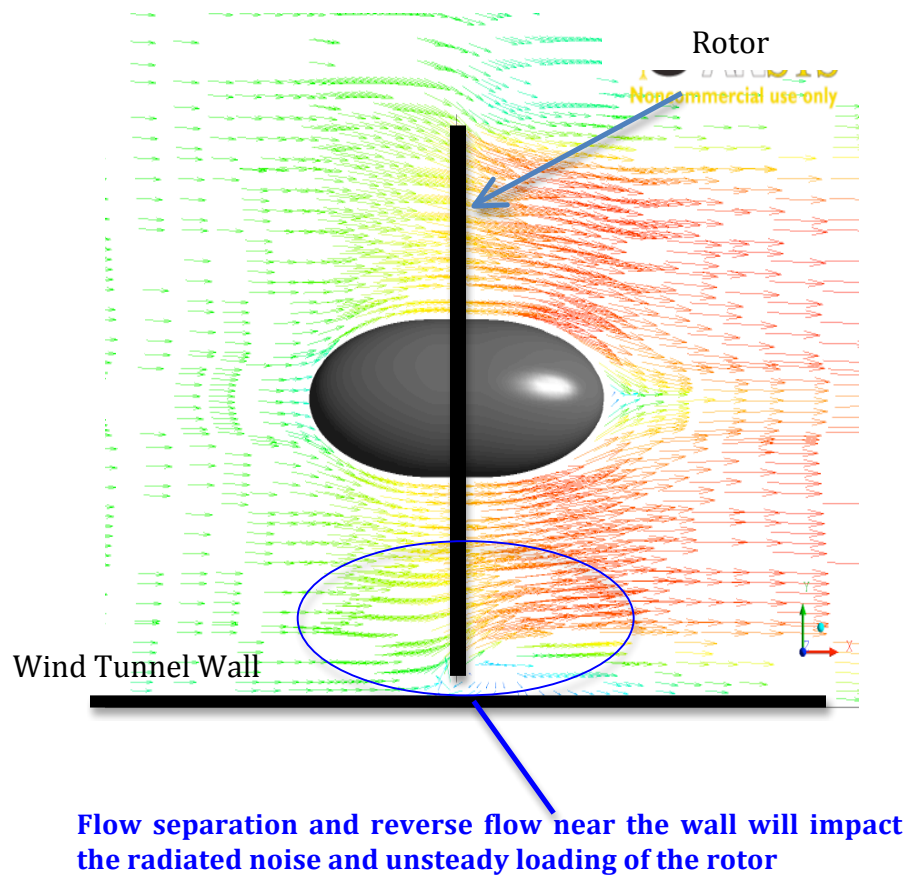
Figure 3.4: The flow entering the rotor near a wall based on an actuator disc RANS calculation for an Advance ratio of *J=0.48*.
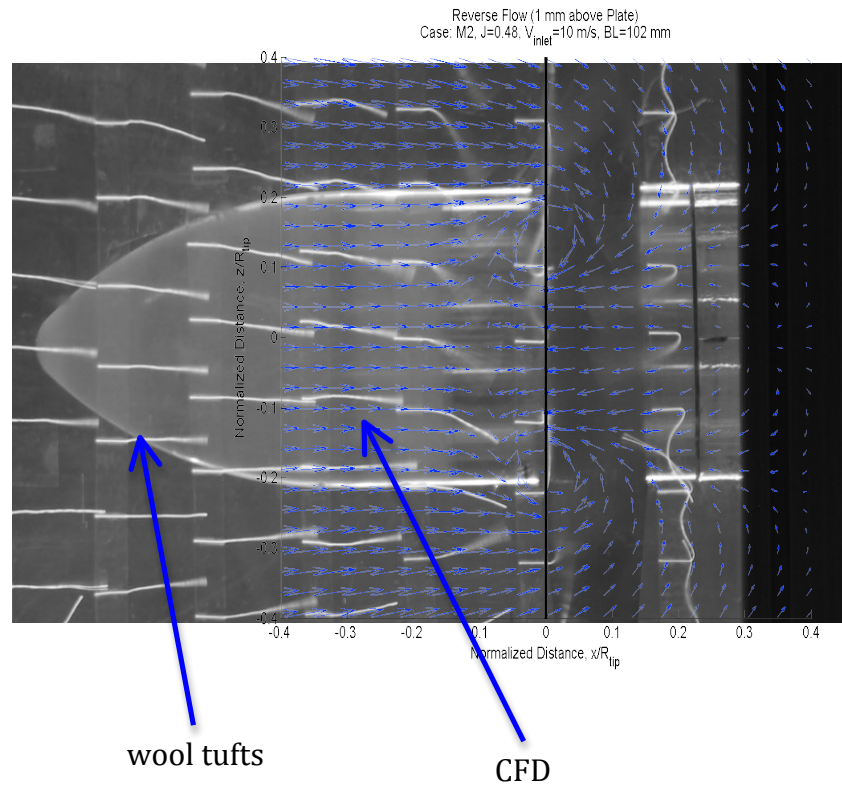
Figure 3.5: Comparison of CFD calculations with flow visualizations made in the Virginia Tech wind tunnel using wool tufts for an operating condition of *J=0.48*. The reverse flow shown by the wool tufts is clearly shown by the CFD calculations.

Drift initiated at 6 radii upstream
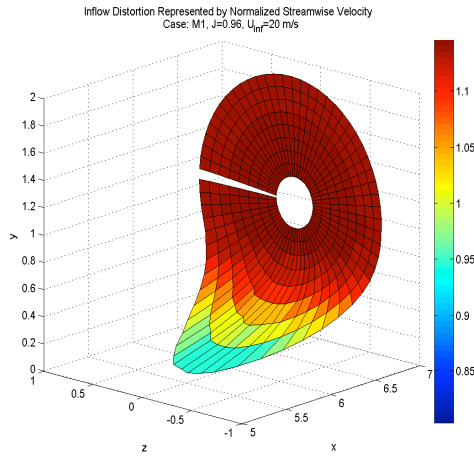
Drift initiated at 0.5 radii upstream
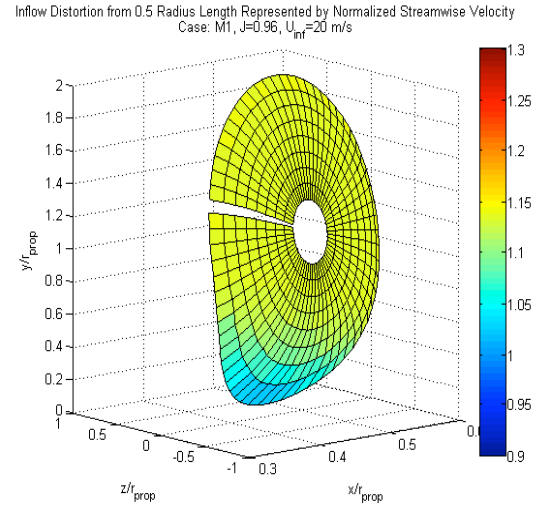
Figure 4.1: The stretching of the material lines caused by a boundary flow entering the rotor at *J=0.96*. The distortion was start 6 radii upstream in the figure on the left and 0.5 radii upstream for the figure on the right.

Predicted and Measured Spectra
J=0.96

Prediction for microphone close to rotor axis

Medium Thrust case J=0.96

29 deg
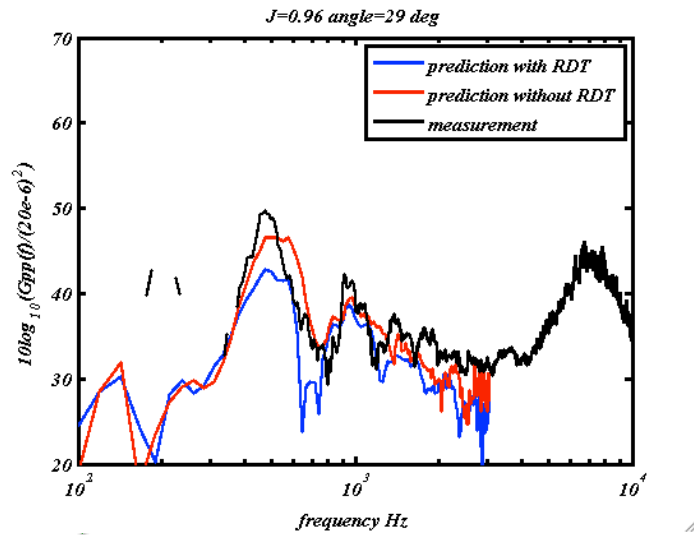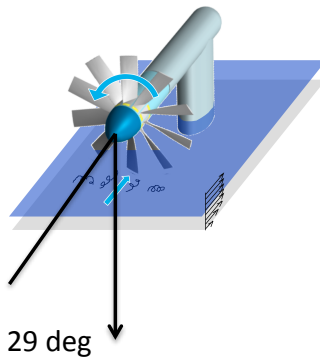
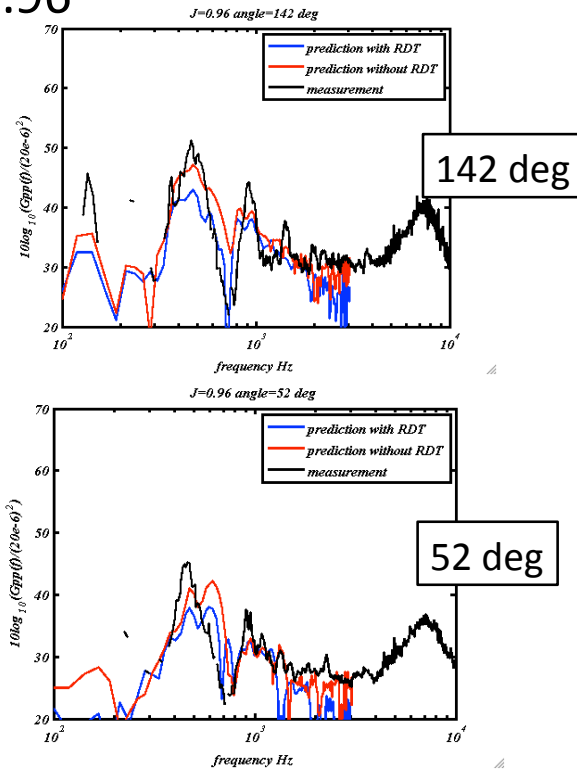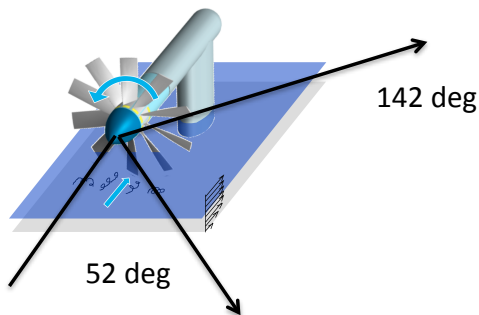Figure 4.2: Predicted and measured spectra at *J=0.96* for a thrusting rotor at 29º to the rotor axis. Predictions with and without RDT are shown.

Predicted and Measured Spectra
J=0.72

Prediction for microphone close to rotor axis

Medium Thrust case J=0.72

29 deg
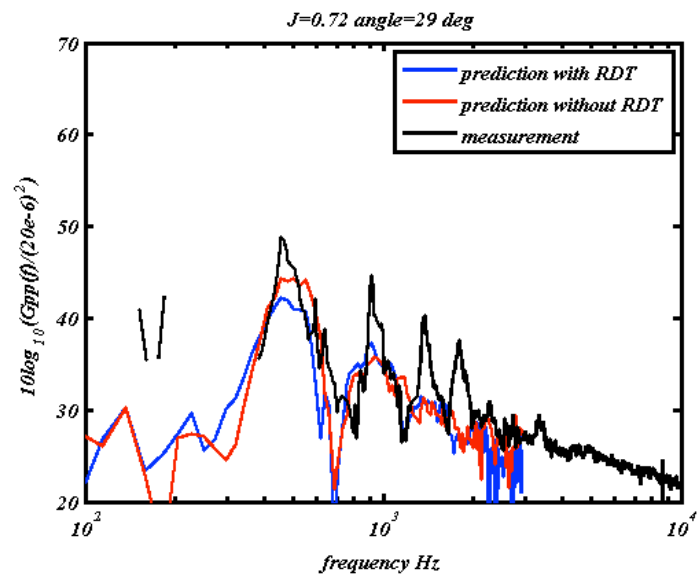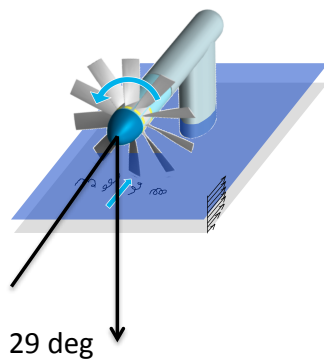
Figure 4.3: Predicted and measured spectra at *J=0.72* for a thrusting rotor at 29° to the rotor axis. Predictions with and without RDT are shown.

Predicted and Measured Spectra
J=0.96

Predictions at different angles to rotor axis

Medium Thrust case J=0.96

142 deg

52 deg

Figure 4.4: Predicted and measured spectra at *J=0.96* for a thrusting rotor at 142º and 52º to the rotor axis. Predictions with and without RDT are shown.
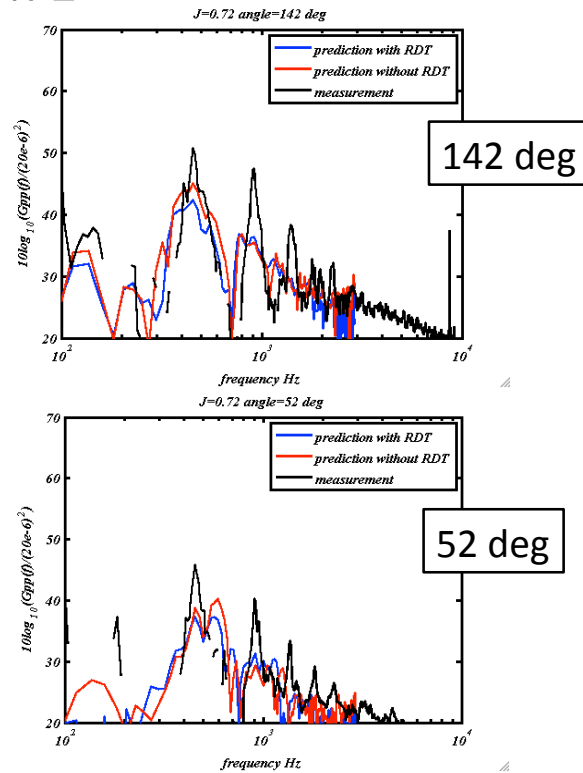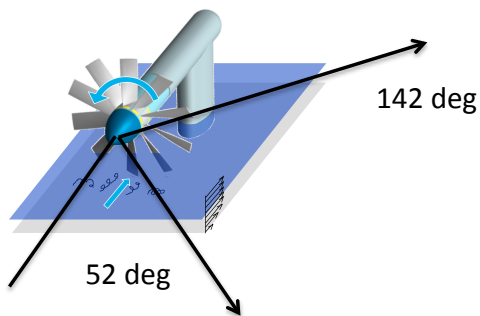
Figure 4.5: Predicted and measured spectra at *J=0.72* for a thrusting rotor at 142º and 52º to the rotor axis. Predictions with and without RDT are shown.